Università degli Studi di Padova

Sede Amministrativa: Università degli Studi di Padova
Dipartimento di Astronomia

scuola di dottorato di ricerca in astronomia
ciclo xxii

Multiple Stellar Populations in Globular Clusters: Spectroscopic evidence

Direttore della scuola: Ch. mo Prof. GIAMPAOLO PIOTTO
Supervisori: Ch. mo Prof. GIAMPAOLO PIOTTO
Ch. ma Prof.ssa MANUELA ZOCCALI

Dottoranda: Anna Marino

S

[22cm] Stampato il January 27, 2010

Acknowledgments

I wish to warmly thank Luigi R. Bedin, Andrea Bellini, Raffaele Gratton, Robert Kraft, Antonino P. Milone, Yazan Momany, Giampaolo Piotto, Alvio Renzini, Chris Sneden, Sandro Villanova, George Wallerstein, Manuela Zoccali without whom the results presented in this thesis would not have been possible.

Fabiola

Riassunto

Il ruolo fondamentale che gli ammassi globulari (AG) hanno storicamente occupato negli studi di evoluzione stellare si deve all'assunzione per cui tutte le stelle di un ammasso costituiscano una popolazione stellare semplice, cioè siano coeve e chimicamente omogenee. Tuttavia, una crescente quantità di dati osservativi sta mettendo in crisi questa visione tradizionale: Stelle all'interno dello stesso ammasso mostrano variazioni e peculiarità nelle abbondanze degli elementi leggeri, e recentemente, fotometria di alta precisione ottenuta dal telescopio spaziale Hubble (HST), ha rivelato sequenze multiple nei diagrammi colore-magnitudine di molti AG.

Nonostante sia ormai stata accettata l'idea che all'interno di uno stesso ammasso siano presenti diverse popolazioni stellari, non è ancora chiaro in che modo possa essersi formata la seconda generazione di stelle. In questa tesi presenterò il mio contributo, principalmente spettroscopico, allo studio di popolazioni multiple in AG.

Dall'analisi di spettri ad alta e media risoluzione ottenuti in diversi telescopi, ho determinato le abbondanze chimiche per vasti campioni di stelle negli AG NGC6121 (M4), NGC6656 (M22), e ω Centauri.

L'analisi di spettri ad alta risoluzione UVES@VLT di più di cento giganti rosse in M4, ha evidenziato che le abbondanze di sodio e ossigeno seguono la ben nota anticorrelazione NaO (rivelata in tutti gli AG dove questo fenomeno è stato studiato). Il risultato di maggior rilievo è che la distribuzione nel contenuto di sodio è chiaramente bimodale, e correla col contenuto in CN. Questa bimodalità è evidente anche in diagrammi colore-magnitudine ottenuti utilizzando immagini in banda U, fortemente contaminata dalle bande molecolari del CN.

Nonostante ω Centauri sia stato considerato per molto tempo il solo AG con differenze intrinseche in ferro, l'analisi spettroscopica di un campione di giganti in M22 osservate da diversi telescopi, ha mostrato la presenza di dif-

ferenze in ferro tra le stelle di questo ammasso. Il contenuto di ferro in M22 è bimodale e correla con l'abbondanza di calcio e di elementi s (Y, Zr, Ba, La): Stelle arricchite in ferro mostrano un'abbondanza maggiore in elementi s. Inoltre, poichè M22 è tra gli ammassi per cui la fotometria HST ha rivelato una distribuzione bimodale nel ramo delle sub-giganti, si può ipotizzare che ci sia una relazione tra questa e la presenza dei due gruppi di stelle con diverso contenuto di ferro. I risultati presentati in questa tesi mostrano che la differenza in ferro contribuisce a riprodurre la separazione osservata nel ramo delle subgiganti, ma non è sufficiente, suggerendo la presenza di effetti più complessi che potrebbero coinvolgere anche le abbondanze di NaCNO.

A causa della grande variazione in metallicità e della presenza di sequenze multiple osservate in tutti gli stadi evolutivi del suo diagramma colore-magnitudine, ω Centauri è sempre stato considerato un'eccezione tra gli AG, ed è stato suggerito che, più che un vero ammasso, sia il nucleo di una galassia distrutta dalle interazioni mareali con la Via Lattea. L'analisi di spettri GIRAFFE e UVES di più di 200 giganti rosse in questo intrigante oggetto, ha mostrato che sua la metallicità varia da ~ -2 fino a ~ -0.7 dex. L'anticorrelazione NaO è ben definita per le stelle appartenenti alla popolazione con contenuto intermedio di metalli, e ci sono tracce di un'anticorrelazione, probabilmente meno estesa, anche per la popolazione a metallicità più bassa. Non ci sono evidenze di anticorrelazione per le stelle con metallicità [Fe/H]> -1.00.

In questa tesi discuterò i risultati osservativi nel contesto delle popolazioni stellari multiple in AG e le loro implicazioni sui modelli teorici di formazione ed evoluzione di questi oggetti.

Resumen

Estrellas en cumulos globulares (CG) han tenido un papel fundamental en nuestro entendimiento de evolucion estelar gracias al hecho que su estrellas pueden ser idelizada como población estelar simple, o sea nacidas en el mismo instante y químicamente homogéneas. Sin embargo, hay una creciente cantidad de datos observacionales que estan desafíando esta interpretacion clasica: Estrellas en el mismo cumulo muestran variaciónes y comportamientos peculiares en las abundancias de elementos livianos, y recien fotometria de alta precisión desde el telescopio espacial Hubble (HST), ha evidenciado secuencias multiples en el diagrama color-magnitud en muchos CGes.

Aunque hoy la presencia de poblaciónes estelares multiples en CGes esta aceptada, todavia no esta claro como una segunda generación de estrellas pudo formarse. En esta tesi voy a entregar mi contribución para el estudio de poblaciónes estelares multiples en CGes, principalmente desde un punto de vista espectroscopico.

Utilizando espectros de alta y mediana resolución observados desde varios telescopios, yo he estudiado las abundancias químicas para una muestra importante de estrellas en los CGes NGC6121 (M4), NGC6656 (M22), y ω Centauri.

En M4, haciendo uso de espectros de alta resolución UVES@VLT para más de cien estrellas gigantes, he encontrado que estrellas siguen la anticorrelacion entre sodio y oxígeno (NaO, como en todos los CGs donde este fenomeno fue estudiado). El resultado importante es que la distribución en el contenido de sodio es claramente bimodal, y está correlacionada con la distribución bimodal de las bandas moleculares de CN entre las estrellas de M4. Estrellas enriquecidas en Na también son enriquecidas en CN. La distribución bimodal es también visible en el diagrama color-magnitud obtenido desde imagenes U, debido a la fuerte influencia de las bandas moleculares de CN sobre la magnitud U.

Si bien ω Centauri fue considerado para mucho tiempo como el solo CG con una dispersión intrinseca en hierro, desde el análisis de una muestra grande de

espectros observados desde varios telescopios, he encontrado evidencias de una variación intrinseca de hierro tambíen en M22. El contenido de hierro en M22 tiene una distribución bimodal, que está correlacionada con la abundancia de calcio y elementos s (como Y, Zr, Ba, La): Estrellas enriquecidas en Fe son también enriquecidas en elementos s. Dado que M22 está entre los CGes donde la fotometria HST ha desvelado una bimodalidad en la rama de las estrellas sub-gigantes, pareceria natural relacionar esta bimodalidad con la bimodalidad en hierro y elementos s. Sin embargo, los resultados de esta análisis demuestran que la diferencia de hierro observada puede contribuir a producir la separación de la rama de la sub-gigantes, pero no es suficiente. Probablemente esto indica que la origen de esta bimodalidad podria ser más complicada y involucrar también las abundancias en NaCNO.

Debido a las grandes variaciónes en metalicidad y las secuencias multiplas obsevadas en diagrama color-magnitud en todos los estadios evolutivos, ω Centauri ha sido siempre considerado una notable excepción entre los CGes, y se ha sugerido que podria ser el núcleo de una galaxia, más que un CG. Desde la análisis de espectros GIRAFFE y UVES para más de 200 gigantes rojas en este fascinante objecto, he obtenido que la metalicidad de ω Centauri varia desde ~ -2 hasta ~ -0.7 dex. La anticorrelacion NaO está bien definida para estrellas que pertenecen a la población con contenido de metale intermedio, y hay algunas indicaciones de una anticorrelacion probablemente meno extendida para la más pobre en metales. Al parecer, la anticorrelacion desaparece para las estrellas con [Fe/H]> -1.00.

En esta tesi discuteré en detalle los resultados observacionales en el contexto de las poblaciónes estelares multiples en CGes y su implicaciones en modelos teoricos de formación y evolución de estos objectos.

Abstract

Globular cluster (GC) stars have occupied a fundamental role in our understanding of stellar evolution thanks to the assumption that their stars can be idealized as a simple stellar population, i.e. coeval and chemically homogeneous. However, there is a growing body of observational facts which challenge this traditional view: Stars inside the same cluster show variations and peculiar patterns in the chemical abundances of light elements, and recently high accuracy photometry from Hubble Space Telescope (HST), has revealed multiple sequences in the color magnitude diagrams (CMD) of several GCs.

Even if today the presence of multiple stellar populations in GCs has been accepted, it is not yet clear how a second generation of stars could form. In this thesis I present my contribution to the study of multiple populations in GCs mainly from the spectroscopic point of view.

By taking advantage of high and mid-resolution spectra collected at various telescopes, I studied the chemical abundances for large sample of stars in the GCs NGC6121 (M4), NGC6656 (M22), and ω Centauri.

In M4, using high resolution UVES@VLT spectra of more than 100 giants, I found that stars define the NaO anticorrelation (as in all GCs studied so far, searching for this phenomenon). The important result is that the distribution in sodium content is clearly bimodal, and this bimodal distribution is correlated with a bimodality in CN molecular strengths among M4 stars. Stars Na-rich are also CN-strong. The bimodality is also visible in the CMDs built using U images, due to the strong effect of the CN bands on the U magnitude.

While ω Centauri was long thought to be the only GC to exhibit a spread in iron abundances, from the analysis of a large sample of spectra collected at different observatories, I found evidence for an intrinsic iron variation in M22. The iron content in M22 has a bimodal distribution, that correlates with calcium and the abundance of s-process elements (as Y, Zr, Ba, La): Stars rich in Fe are also s element rich. Since M22 is among globulars where HST

photometry has revealed a split in the sub-giant branch (SGB), it is tempting to relate the presence of the two stellar groups with different iron with the SGB split. However, from the present analysis I conclude that the observed difference in [Fe/H] can contribute to produce the split, but it is not sufficient. This probably indicates that the reason for the SGB split may be far more complicated and also involve the NaCNO abundances.

Because of its large metallicity variations and the multiple sequences observed in the CMD in all the evolutionary stages, ω Centauri has always been considered a noticeable exception among GCs, and has even been suggested to be the remnant of a dwarf galaxy rather than a GC. From the analysis of GIRAFFE and UVES spectra for more than 200 red giant stars in this intriguing object, I derive that ω Centauri metallicity ranges from ~-2 to ~-0.7 dex. NaO anticorrelation is well defined for stars belonging to the populations with intermediate metal content, and some hints of a probably less extended one are present for the more metal poor stars. Apparently, the anticorrelation disappears for stars with [Fe/H]> -1.00.

In this thesis I will discuss in details the observational findings in the context of multiple populations in GCs and their implications in the theoretical models on the formation and evolution of these objects.

Contents

1

Introduction

The recent discoveries of multiple stellar populations in Globular Clusters (GC) have stimulated new interest on GC research and have prompted a lively debate in the literature. Indeed, the idea of GCs hosting simple stellar populations (SSP), e.g. formed by stars coeval and sharing identical chemical composition, have always constituted a paradigm, and ruled GCs to represent an ideal laboratory for testing the stellar evolutionary models.

Until few years ago, the only known example of GC contradicting the SSP paradigm was ω Centauri, the most massive cluster, whose stars show a large spread in metallicity. However this cluster has always been considered a noticeable exception, and has even been suggested to be the remnant of a dwarf galaxy rather than a GC.

Instead, today the situation appears more complex, and it seems clear that none of the GCs studied so far is a real SSP. A lot of evidence of multiple stellar populations in GCs have been added, and new efforts to theoretically interpret the observations are needed.

In this thesis I present the contribution, given during my PhD, on the spectroscopic study of multiple stellar populations.

In this chapter the observational scenario, both from a spectroscopic and photometric point of view, is summarized, together with a brief description of the possible scenarios proposed to explain the presence of multiple populations in GCs.

1.1 Abundance variations in Globular Clusters

GCs are essentially monometallic, e.g. all the stars in a cluster show the same [Fe/H] abundance. The most notable exception is ω Centauri which has a well-

established metallicity spread of about 1 dex (Dickens & Bell 1976; Butler et al. 1978; Norris 1980; Persson et al. 1980). Also photometry confirms that ω Centauri shows the presence of different populations of stars with different metallicities (Lee et al. 1999, Pancino et al. 2000).

Despite ω Centauri was always considered an exception among GCs, because of its spread in iron, all of them show abundance variations in particular elements. The differences in chemical content of these elements for stars within the same cluster, constitute the first hint that GCs host multiple stellar populations. Yet in the early eighties, Cohen (1978) noted a scatter in the sodium abundance among stars in M 3 and M 13. Today, thanks to high resolution spectroscopic studies, we well know that stars in GCs are not chemically homogeneous: Despite they generally show the same abundance insofar the heavy elements are considered, notable variations are present in several light elements. Sometimes these abundance variations result in well defined pattern, such as the anticorrelations between C and N, Na and O, Mg and Al. Also variations in the molecular CH, CN and NH band strengths, due to a spread in the abundances of carbon and nitrogen have been observed, as well as anticorrelations between CH and CN strengths, and, in some cases, also a bimodality in the CN content.

While part of these variations, like C and N variations, are present also in field stars, and are expected from typical evolution of low mass stars (Sweigart & Mengel 1979), some others (O, Na, Mg, Al) follow a pattern typical of GCs. In particular Na and O are anticorrelated in all the GCs studied so far, but the extension of the NaO anticorrelation changes from cluster to cluster as shown in Fig.1.1 from Carretta et al. (2009). There are globulars with well extended NaO anticorrelation, others where Na and O abundances span over smaller ranges. In some notable cases stars appear to cluster around different values of Na and O. In NGC2808, that shows a NaO anticorrelation well extended towards low O values, three groups of stars with different O abundances are present (Carretta et al. 2006). In M4, where the anticorrelation is less extended, two groups of stars with different Na abundances have been found (Marino et al. 2008).

NaO anticorrelation (and MgAl one) is the hint of the presence in the stellar surfaces of a fraction of the GC stars, of material which have undergone H burning at temperatures of a few ten millions K (Prantzos et al. 2007). The fact that the total C+N+O abundance does not seem to vary, within the observational errors (Cohen & Melendez 2005), indicates that the material from which a second generation formed, has been processed through the hot CNO cycle. However, in a recent paper Yong et al. (2009) have shown some evidence of variations in the sum of CNO elements within stars in NGC 1851 (see Sect. 1.3 for more details).

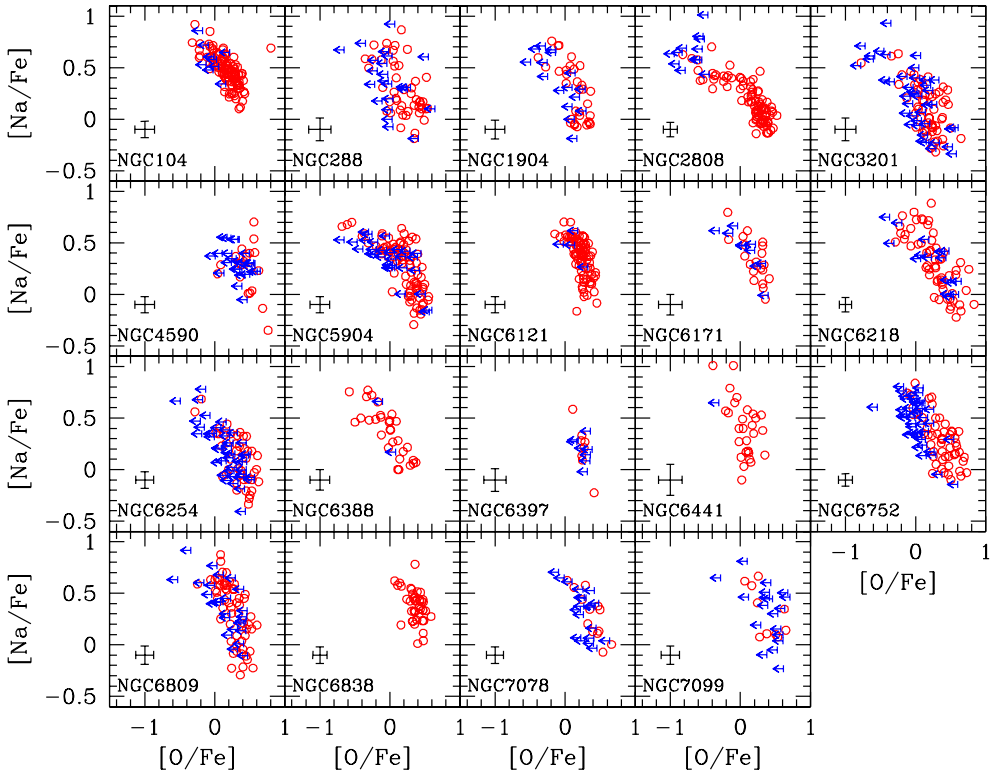

FIGURE 1.1— NaO anticorrelation observed in 19 GCs from Carretta et al. (2009).

The site where this processed material forms and how it reaches the stellar surface of some stars are still debated questions. Two scenarios (briefly described in Sect.1.4) have been proposed to explain the observed chemical heterogeneity: the evolutionary scenario and the primordial one, both apparently supported by observations (see Kraf 1994 for a review).

The observed decline of C content (e.g. in M13, as shown by Smith & Briley 2006) and the decreasing ratio $^{12}C/^{13}C$ (observed in M4 and NGC 6528 by Shetrone 2003) along the RGB phase, support the evolutionary scenario. According to this theory, the origin of the observed star-to-star scatter in light elements is due to the mixing of CNO-cycle-processed material transported, in a way not yet well understood, to the stellar surface. In this way the observed anticorrelations would be present in the evolved stages of the life of stars, after the RGB bump.

At odds with this scenario, in the last few years, spectroscopic studies have revealed light element abundance variations in unevolved main sequence stars and less-evolved RGB stars, fainter than the RGB bump. The Na-O anticorrelation was found at the level of the main sequence turn-off (TO) and sub giant branch (SGB) in M13 (Cohen & Melndez 2005), NGC 6397 and NGC 6752 (Carretta et al. 2005; Gratton et al. 2001), NGC 6838 (Ramirez & Cohen 2002) and 47 Tuc (Carretta et al. 2004). In 47 Tuc, a bimodal distribution in the CN strengths, similar to that found among RGB stars (Norris & Freeman 1979), was found also in the main sequence (MS) by Cannon et al. (1998).

The last observational evidence seem to confirm the primordial scenario with a successive generation of stars formed in GCs, after that a first generation realized in the intracluster medium material processed by H burning at high temperatures. In this way the observed groups of stars are really two different populations.

However also mixing in evolved stars should take a role. Indeed, recent observations made by Recio Blanco & de Leverny (2007) of upper RGB stars in several GCs, suggest that evolutionary effects should be at work in these stars, given that the $^{12}C/^{13}C$ ratio has reached close to its nuclear equilibrium value in virtually all of them.

Interestingly enough, recent findings show that some GCs, besides ω Centauri, show abundance variations also in heavy elements. Variations in *s*-elements were found in NGC 1851 (Yong et al. 2008) and in M 22 (Marino et al. 2009). Very surprisingly M 22, like ω Centauri, shows evidence of small variations also in [Fe/H] (Marino et al. 2009). Probably the evolutionary history of ω Centauri and M 22, that are the only globulars showing evidence of iron variations, is different from the one of the other GCs, since the iron variations indicate the contribution from Supernovae explosion in the enrichment of

the intracluster medium.

1.2 Horizontal Branch second parameter problem

Since the sixties (Sandage & Wildey 1967, van den Bergh 1967), we know that the horizontal branches (HB) of some GCs can be rather peculiar. There are GCs with a double HB, well populated in the both sides of the RR-Lyrae instability strip, others showing extension versus the blue, the so called Blue Tails, and some others with a single HB. This problem, usually known as the the second parameter problem, still lacks of a comprehensive understanding: many mechanisms, and many parameters, such as metallicity and cluster age, have been proposed to explain the HB peculiarities, but none apparently is able to explain the entire observational scenario. A classical example is the case of M3 and M13, two clusters with roughly the same metallicity, but showing different HB morphologies as shown in Fig.1.2. It is well possible that a combination of parameters is responsible for the HB morphology (Fusi Pecci et al. 1993). Surely, the total cluster mass seems to have a relevant role (Recio-Blanco et al. 2006) since the more massive clusters show extended HB.

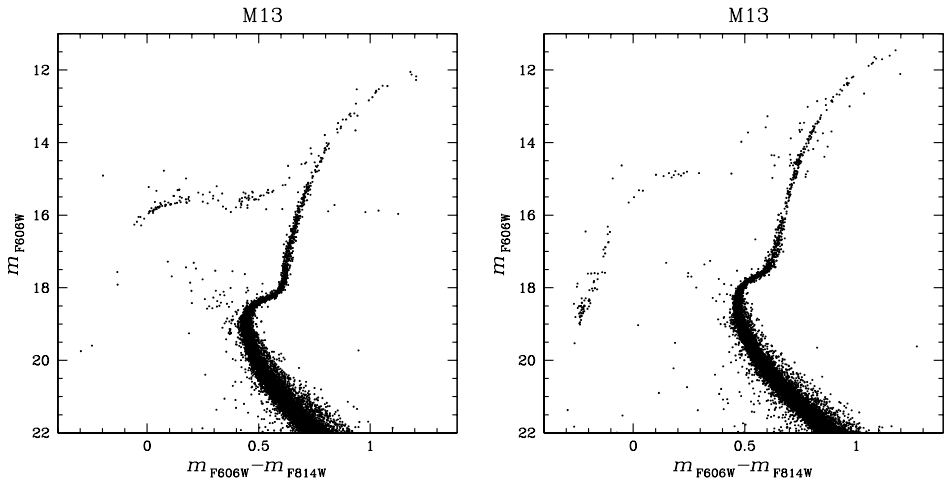

FIGURE 1.2— M13 and M3 CMD from ACS photometry.

Given the presence of different groups of stars with different chemical abundances in GCs, it is tempting to relate the second parameter problem to the complex abundance pattern of GCs. Interestingly enough, D'Antona et al. (2005) made the hypothesis of three groups of stars, with three different helium abundances in order to explain the peculiar, multi-modal HB of NGC 2808 (Sosin et al. 1997, Bedin et al. 2000). However, it is noteworthy, that the

He abundances are difficult to determine directly from spectra, because of they appear in hot stars. However for HB stars with T≥11500 some phenomena like the gravitational settling are expected and He should sediment in the stellar atmosphere making impossible to have reliable He spectral lines.

Since high Na and low O abundances are signatures of material processed through hot H-burning, they should be accompanied by high He-content (D'Antona & Caloi 2004). In this way, the NaO anticorrelation should be indicative of the He abundance. Interestingly enough, Carretta et al. (2009) show that the NaO anticorrelation extension is related to the very blue (and hot) extreme of the HB.

In most cases, small He excesses up to Y∼0.04 (that is Y∼0.28, assuming that the original He content was the Big Bang one) are expected. While this should have small impact on colors and magnitudes of stars up to the tip of the RGB, a large impact is expected on the colors of the HB stars, since He-rich stars should be less massive. E.g., in the case of GCs of intermediate metallicity ([Fe/H]∼−1.5), the progeny of He-rich, Na-rich, O-poor RGB stars should reside on the blue part of the HB, while that of the normal He-poor, Na-poor, O-rich stars should be within the instability strip or redder than it. Actually mean HB colors are influenced by the mass loss along the RGB and by small age differences of 2-3 Gyr. However, within a single GC a correlation is expected between the distribution of masses (i.e. colors) of the HB-stars and of Na and O abundances.

1.3 Globular Clusters with photometric evidence of multiple stellar populations

While there are spectroscopic evidence of abundance variations, due to the presence of different generations of stars, in all the GCs studied so far, to date photometric evidence were found only in some of them.

Indeed, despite the spectroscopic observations of chemical variations, up until a few years, the view of GCs as SSP was supported by the interpretation of the available Color-Magnitude Diagrams (CMD) in the framework of theoretical stellar evolution (see, for instance, King et al., 1998). In very many instances deep Hubble Space Telescope (HST) photomtry has revealed exquisitely narrow sequences in the CMD from the main sequence (MS) to the RGB tip (e.g. Bedin et al. 2001 for M4, or Richer et al. 2008 for NGC6397).

Very recently, a spectacular, and somehow unexpected confirmation that, at least in some GCs, the origin of the chemical anomalies must be primordial came from high precision photometry from HST. In Fig.1.3, the ACS CMDs (apart from M4 for which the CMD came from Wide Field Imager photometry)

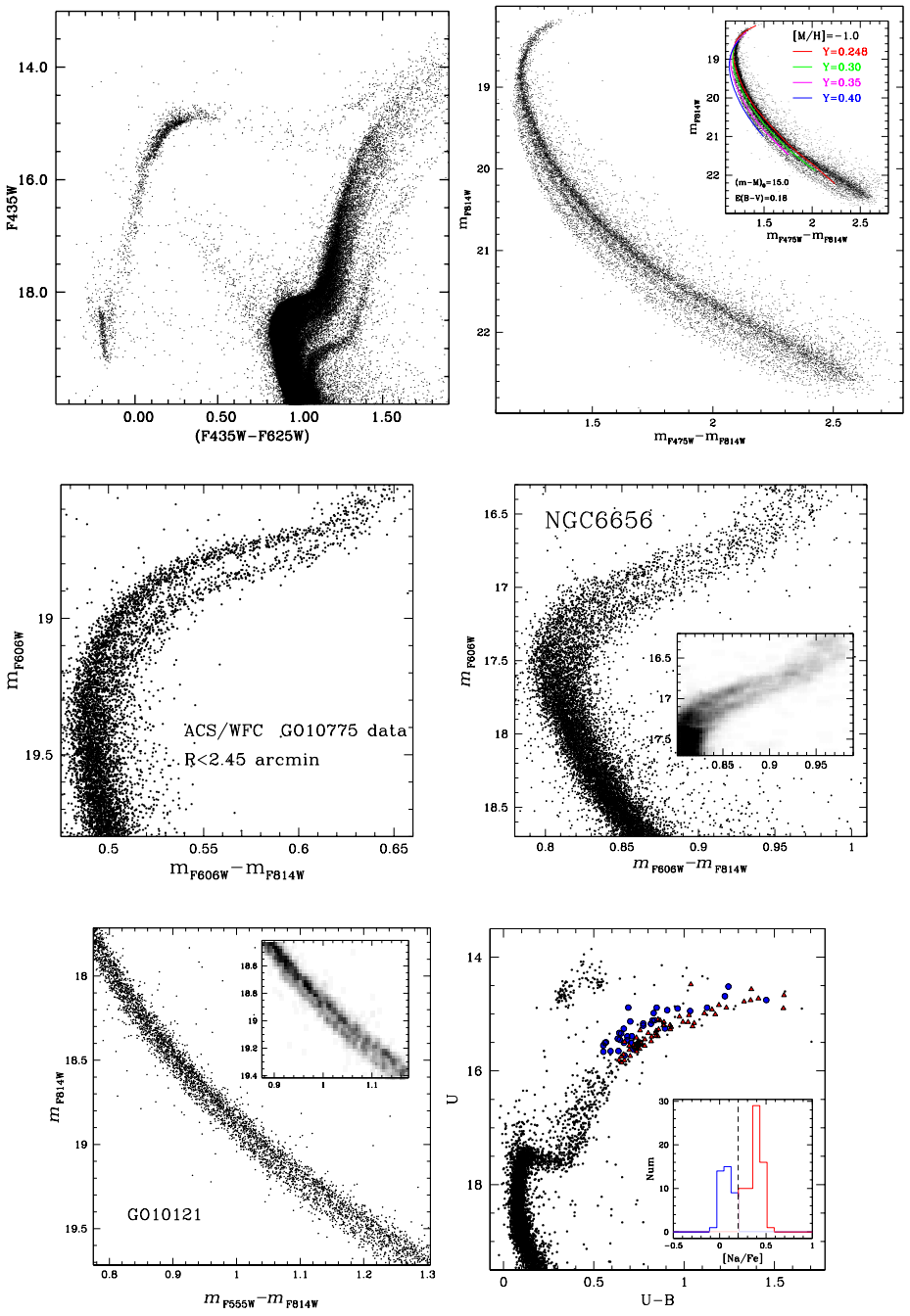

FIGURE 1.3— *Upper panels*: ACS CMD for ω Centauri (from Villanova et al. 2007), and NGC2808 (from Piotto et al. 2007). *Middle panels*: ACS CMD for NGC1851 (from Milone et al. 2008) and NGC 6656 (from Piotto 2009) that show a split SGB. *Lower panels*: the MS of NGC6752 (from Milone et al. 2010) obtained from ACS photomtry, and the WFI CMD of M4 (from Marino et al. 2008).

for some GCs with evidence of multiple stellar populations are represented.

As already said, the first object challenging the paradigm of GCs hosting simple stellar populations was ω **Centauri**, that exhibits a very complex RGB structure. As shown by Bedin et al. (2004), the MS splits into two sequences, but the most exciting discovery came from the spectroscopic investigation by Piotto et al. (2005), who found that the bluest MS is more metal rich than the redder one. The only way to account for the spectroscopic and photometric properties of the two main sequences is to assume that the bluest sequence is also strongly He enhanced, to an astonishingly high Y=0.38. More recently, Villanova et al. (2007) showed that the two main sequences split in at least four sub giant branches (SGB) which must be connected in some way to the multiplicity of RGBs identified by Lee et al. (1999) and Pancino et al. (2000). The metal content of the different SGBs measured by Villanova et al. (2007) also implies a large age difference among ω Centauri stellar populations, larger than 1 Gyr, even if the exact age dispersion depends on the assumed abundances (including the He content) of the different stellar populations, and it is still controversial (Sollima et al. 2007). Bedin et al. (2004) demonstrated that there is also a third MS, running on the red side of the two main MSs, and likely connected with the anomalous RGB-a of Pancino et al. (2000). Since the seventies we know from spectroscopic studies that ω Centauri shows iron-peak element dispersion (Freeman & Rodgers 1975; Norris et al. 1996; Suntzeff & Kraft 1996). Despite abundance variations in iron-peak elements were recently found also in M22 and NGC1851, ω Centauri still remains the most extreme case among GCs, both for the larger abundance dispersions and for the multiple sequences seen in each part of its CMD. In a sense, the findings by Pancino et al. (2000), Bedin et al. (2004), Piotto et al. (2005), Villanova et al. (2007) and Sollima et al. (2007) could simply be considered additional evidence that ω Centauri is so peculiar that it might not be a GC. Perhaps, as suggested by many authors (Freeman 1993, Hughes & Wallerstein 2000), it might simply be the nucleus of a much larger system, likely disrupted by the tidal field of our Galaxy. For a more detailed description of the complex multiplicity of stellar populations in ω Centauri we remand to Chapter **??**.

Similarly to ω Centauri, also M54 clearly exhibits multiple SGBs (Piotto 2009), and has hints of multiple MSs. The complexity of M54 makes good sense, because it coincides with the nucleus of the tidally disrupting Sagittarius dwarf-spheroidal galaxy. M54 might be the actual nucleus or, more likely, it may represent a cluster that migrated to the nucleus as a result of dynamical friction (Bellazzini et al. 2008). ω Centauri and M54 are the two most massive GCs in our Galaxy, and it is quite possible that they are the result of similar—and peculiar—evolutionary paths (Piotto 2009). In any case, even ω Centauri

and M54 are not the only clusters to exhibit non-singular populations. Exciting new discoveries, made in the last few years, clearly show that the GC multi-population zoo is quite populated, inhomogeneous, and complex.

The second, in time, GC in which photometric evidence of multiple populations were found is **NGC2808** (Piotto et al. 2007). NGC 2808 has been always considered a GC, with many peculiar properties regarding its metal content and its CMD, but a genuine, massive GC. Still, it hosts multiple stellar populations. Moreover, also in this case, in view of the negligible dispersion in iron-peak elements in NGC2808, the only way so far available to reproduce the three MSs is to assume that there are three populations, characterized by three different helium contents, up to an (again) astonishingly high Y=0.40. Interestingly enough, D'Antona et al. (2005) already made the hypothesis of three groups of stars, with different helium abundances in order to explain the peculiar, multi-modal HB of NGC2808 (Sosin et al. 1997, Bedin et al. 2000). Piotto et al. (2007) simply found them in the form of a MS split and also noted that the different stellar populations in NGC2808 are consistent with the spectroscopic observations by Carretta et al. (2006), who identified three groups of stars with different oxygen abundances. The fraction of stars in the three abundance groups is in rough agreement with the fraction of stars in the three MSs.

NGC1851 hosts two distinct sub-populations (Milone et al. 2008) as indicated by the split in the SGB region, as shown in Fig.1.3. This discovery has brought new interest on this cluster accompanied by numerous efforts aimed to better understand how this cluster formed and evolved. Milone et al. (2008) noted that, if the double SGB is only due to an age difference, the two star formation episodes should have occurred with a time delay of about one Gyr. As an alternative scenario, Cassisi et al. (2008) and Ventura et al. (2009) showed that two stellar populations, one with a normal, and one with enhanced CNO, could respectively account for the observed bright and faint SGB (bSGB and fSGB), without requiring any significant age difference. Interestingly, this working scenario seems to be supported by spectroscopic measurements (Hesser et al. 1982) indicating the presence of two groups of CN-strong and CN-weak stars. A more recent spectroscopic investigation cames from Yong & Grundahl (2008) who determined the chemical composition for eight bright giants in this cluster. Their analysis revealed large star-to-star abundance variations of Zr and La. These *s*-process elements are correlated with Al and anticorrelated with O. Furthermore, the Zr and La abundances appear to cluster around two distinct values. Unfortunately, their sample is too small to determine with some significance whether the measured O abundances are bimodal or not. NGC 1851 is also considered a sort of prototype of bimodal HB clusters. Milone et

al. (2008) noted that the fraction of fainter/brighter SGB stars is remarkably similar to the fraction of bluer/redder HB stars. Therefore it is tempting to associate the brighter SGB stars to the CN normal, *s*-process element normal stars and to the red HB, while the fainter SGB should be populated by CN strong, *s*-process element enhanced stars which should evolve into the blue HB. This scenario requires that fSGB stars are the younger population and cames from processed material.

Throught the HST presise photometry, other clusters were added to the globulars with a split (or broaden) SGB: NGC 362, NGC 5286, NGC6388, NGC 6656 (M22), NGC6715 (M54), and NGC 7089 (M2) (Piotto et al. in preparation), 47Tuc (Anderson et al. 2009) .

We computed a study of a sample of RGB stars in **M22**, a globular with a split SGB. This GC is a very interesting one. For decades this cluster has been suspected to have metallicity variations, including a spread in [Fe/H]. The iron spread has been controversial till very recently, when, thanks the UVES@VLT high resolution spectra of RGB stars, we (Marino et al. 2009) could demonstrate that, not only the [Fe/H] spread is confirmed, but that, indeed, there is a bimodal distribution in the iron content, and that this distribution is correlated with the abundance of *s*-process elements (Y, Zr, Ba, and Nd): Stars rich in Fe and Ca are also s-process element rich. The bimodal distribution of the SGB stars in M22 might be related to these two metallicity groups. We will discuss more in detail this findings on M22 in Chapter 3.

In **47Tuc** Anderson et al. (2009) have shown that not only a complex, multimodal SGB is present, but also an intrinsically broad MS. Very interestingly this GC shows a CN bimodality that was observed from the MS to the RGB tip (Cannon et al. 1998).

It is worth noting that the clusters showing multiplicities in their CMDs are among the most massive GCs of our Galaxy ($M > 10^6 M_\odot$) and all of them have peculiar HBs, as well as peculiar abundances, including NaO anticorrelations. However, we must also note that much less massive GCs, with no evidence of multiple populations identified so far, show very large star-to-star abundance variations.

In this respect, it is particularly interesting the spectroscopic study we computed on **M4** stars. By studying a large sample of RGB stars in the GC M4, we found two distinct groups of stars with a different sodium content, which also displays a remarkable difference in the strength of the CN-band. These two spectroscopic groups were found to populate two different regions along the RGB. We also noted that the RGB spread is present from the base of the RGB to the RGB-tip, suggesting that the spread must be related to the presence of two distinct stellar generations. Interestingly, the mass of this cluster is

at least an order of magnitude smaller than that of any other cluster showing photometric evidence of multiple stellar population. However the bimodality on the CMD was recognized only when we overimpose the two spectroscopically identified groups of stars on the U vs. $U-B$ CMD (see Chapter 2 for further details).

The last found GC showing evidence of multiple populations is **NGC6752** (Milone et al. 2009) where the MS appears spread, and maybe splitted. Like in M4, also in this case, overimposing the two groups of stars selected on the NaO anticorrelation, they appear to define two different sequences on the RGB in the U vs. $U-B$ CMD (see Chapter 2).

1.4 Scenarios for the origin of the multiple populations

After the early observations of chemical anomalies in GCs, the theory of **RGB self-enrichment** was proposed by Sweigart & Mengel (1979). They proposed that in low mass upper RGB stars mixing could extend to below the formal boundary of the convective envelope, and reach the H-burning shell. In this way the processed material could be brought to the surface, establishing the abundance (anti)correlations. Also He enrichment could take place affecting the HB evolution (Sweigart 1997; Sweigart & Catelan 1998, Moehler & Sweigart 2006). However, as said in Sect.1.1, even if the Sweigart-Mengel process should take a role, the observations of the chemical anomalies at much lower luminosities and down to the MS indicate that different populations of stars, born at different stages of the cluster evolution, are present in GCs. Another indication of the co-esistence of multiple stellar populations in GCs, is that halo field stars with the same metallicity do not show such huge variations (Kraft 1994). Indeed, the cluster environment is a critical factor. The anomalous composition can be attributed to the fact that nuclear processing in a first generation has been followed by the formation of a second generation, and such processes could be influenced by the dense GC environment.

Critical for understanding the origin of the multiple populations in GCs, is to identify the progenitor stars responsible for the excess of some elements (like Na and Al) in the second generation stars. An important constraint, always considered for the progenitors, was that they must activate the hot CNO cycle, and not, the He-burning phase, since the observed C+N+O in the studied GCs is constant (Cohen & Melendez 2005) within the errors. However, the constancy of C+N+O has been challenged by the discovery of double SGBs in some GCs. Indeed, theoretical studies suggest that the double SGB in NGC1851 could be due to a difference in the total C+N+O (see Sect.1.3). However, we have to note that only one spectroscopic study based on a small sample (8 stars) was

done indicating variations of C+N+O (Yong et al. 2009).

To date, **AGB stars** are the best candidate for being responsible for at least some of the chemical anomalies observed in GCs (D'Antona, Gratton & Chieffi 1983; Iben & Renzini 1984). These stars have the advantage to account, in a time, for the NaO and AlO anticorrelations, and also for the recent observations of the variations in s-process elements (and in the total C+N+O). Moreover AGB stars eject large amounts of mass at low velocity ($\sim$10-20 km s^{-1}) which can be retained within the potential well of GCs.

Following the theoretical models, these stars should activate the Hot Bottom Burning process that reproduces the observed NaO and AlO anticorrelations, and trough the second dredge-up, large amounts of He are lead to the stellar envelope. The constant C+N+O, generally observed in GCs, is explained with more massive AGB progenitors for which the nucleosynthesis is not greatly affected by the third dredge-up, responsible for increasing the sum CNO and the s elements.

However, the effects of the third dredge-up increase with time, as the evolving mass decreases. The AGB luminosity and the mass loss rate also decrease and the star undergoes a larger number of thermal pulses during the AGB phase. Following this scenario, how longer is the second generation formation, higher are the effects due to the third dredge-up, e.g. the vaiation in the total CNO abundance and in the s elements.

An alternative to the AGB, as the progenitors for a second stellar population, are the **fast-rotating massive stars** (Maeder & Meynet 2006; Decressin et al. 2007; Meynet, Decressin & Charbonell 2008). Massive rotating stars would bring to the stellar surface the processed H-burning material (i.e. He), via a mechanism called meridional circulation, whose efficiency is, however, not well predicted. Moreover these stars lose mass by slow outflowing equatorial disk, by fast radiative winds, and by core-collapse supernova explosion. However, both the stellar winds and supernova ejecta, that run at thousands of km/s, would not be retained inside the shallow potential well of the protocluster. Consequently, the only way to produce stars enriched in helium is within the outflowing disk whose helium abundance increases as evolution proceedes. The problem of this scenario is that the star formation around a given fast rotating star, should take place before the outflowing disk is destroyed by supernova ejecta or fast winds from nearby stars (Meynet et al. 2008). Another difficulty is that the stars formed in the outflowing disk, will reflect the helium abundance of this disk. Indeed the He abundance varies from disk to disk, since the amount of the outflowing He depends on the star and its evolutionary stage. Following this scenario we should observe a spread in the He abundance, while we observe stellar populations clustered around different abundances. Never-

theless, it is possible that meridional circulations are at work in massive stars, and bring fresh helium to the surface.

In summary, it is clear that GCs are not as simple systems as thought in the past. Up to now, we lack a complete explanation for the mechanisms necessary to understand the great observed variety and complexity. Even if, it seems that the AGB scenario is the one that better accounts for the observed chemical anomalies observed in GCs, our understanding of the origin of multiple populations is far to be complete. We still remain with a lot of open questions: first of all, if this scenario is correct, the mass of a first stellar population in a cluster had to be several times larger than the present mass of the cluster, suggesting that, at least some GCs, are the remnant nucleus of dwarf galaxy cannibalized by the Miky Way.

1.5 Thesis layout

To shed light on the origin of different stellar generations in GCs, a systematic study of the chemical abundances of large samples of stars in GCs is mandatory. A detailed analysis of the chemical content of stars belonging to various populations will help to understand the nature of the progenitors responsible for the excess of some elements in the second generation.

In the following chapters I will discuss my contribution to the observational scenario, and the implications on theoretical models, obtained in the context of multiple populations in GCs. Results obtained during my PhD mainly derive from the analysis of chemical abundances in GC stars, spectroscopic results were then combined with high precision photometry from Wide Field Imager (WFI) and HST. I will describe the study computed for three GCs, where the presence of different populations of stars manifests in different ways.

The layout of the thesis is as follows:

- In Chapter 2 I will discuss the results derived for M4 from the analysis of high resolution UVES@VLT for a sample of more ∼100 RGB stars.
- Chapter 3 presents a spectroscopic analysis of RGB stars in M22, from an heterogeneous set of high and mid-resolution spectra.
- In Chapter **??** I will describe the results obtained for ω Centauri by analysing a sample of ∼200 stars from UVES and GIRAFFE data.
- Chapter 5 summarizes the findings of this study.

2

Multiple populations in the GC NGC6121 (M4)

In this chapter it is presented a study on the chemical abundances of the GC NGC 6121 (M4) from high resolution spectra of RGB stars.

As far as we know, M4 shows no evidence of multiple stellar populations in its CMD, and its mass ($\log\frac{M}{M\odot} = 4.8$, Mandushev et al. 1991) is much smaller than the mass of the clusters with the photometric peculiarities discussed in the previous chapter.

Chemical abundances from high resolution spectra of M4 RGB stars have been already measured by different groups of investigators: Gratton, Quarta & Ortolani 1986 (hereafter GQO86), Brown & Wallerstein 1992 (BW92), Drake et al. 1992 (D92), Ivans et al. 1999 (I99), and Smith et al. (2005). These authors have found a range of [Fe/H] between -1.3 dex (BW92) and -1.05 dex (D92). For further details, see I99 who have summarized the chemical abundances found in previous studies. A study by Norris 1981 (hereafter N81) of 45 RGB stars showed a CN bimodality in M4, e. g., stars of very similar magnitudes and colors have a bimodal distribution of CN band strengths. By analyzing 4 RGB stars, two selected from the CN-weak group and two from the CN-strong one, D92 (and then Drake et al. 1994) found differences in the Na and Al content. I99 found that O is anticorrelated with N, whereas Na and Al abundances are larger in CN-strong stars. Looking at the evolutionary states of these stars, both I99 and Smith & Briley 2005 (SB05) did not find any strong correlation between CN band strength and the position on the CMD. More recently, Smith et al. (2005), studying the fluorine abundance in seven RGB stars in M4, found a large variation in ^{19}F, which is anticorrelated with the Na and Al abundances.

In these previous studies, both the evolutionary scenario and a primordial one have been taken into account in order to explain the light element variations and the CN bimodality in M4.

In our study, we have analyzed high resolution spectra in order to study chemical abundances for a large sample of M4 RGB stars and compare our results with those of previous studies. Our results will be discussed in the context of the multipopulation phenomenon in GCs.

In Section 2 we provide an overview of the observations and target sample. The membership criterion used to separate the probable cluster stars is described in Section 3, and the procedure to derive the chemical abundances is in Section 4. We present our results in Section 5, and discuss them in Section 6 and Section 7. Section 8 summarizes the results of this work.

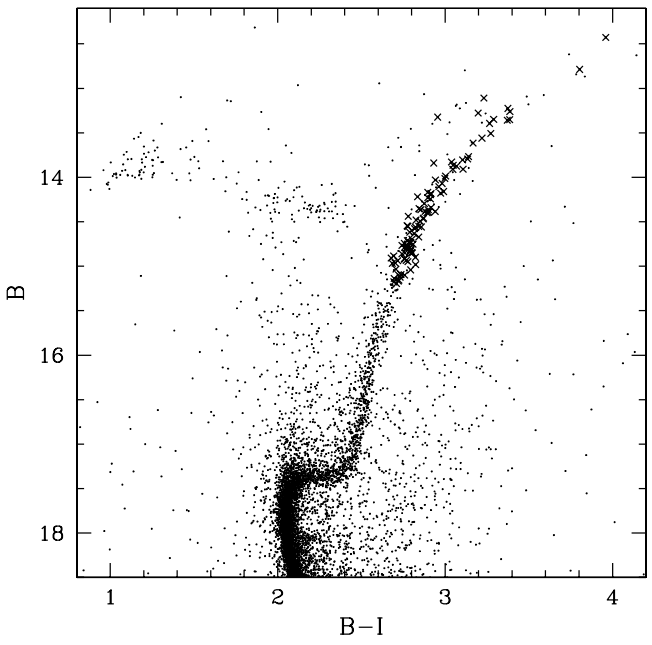

FIGURE 2.1— Distribution of the UVES target stars on the B vs. (B − I) CMD corrected for differential reddening.

2.1 Observations and Data Reduction

Our dataset consists of UVES spectra collected in July-September 2006, within a project devoted to the detection of spectroscopic binaries in the GC M4, and to the measurement of the geometric distance of this cluster (Programs 072.D-0742 and 077.D-0182). Data are based on single 1200-1800 sec exposures obtained with FLAMES/VLT@UT2 (Pasquini et al. 2002) under photometric conditions and a typical seeing of 0.8-1.2 arcsec. The 8 fibers feeding the UVES spectrograph were centered on 115 isolated stars (no neighbours within a radius of 1.2 arcsec brighter than $V + 2.5$, where V is the magnitude of the target star) from $\sim$ 1 mag below the HB to the tip of the RGB of M4, in the magnitude range $10.5 < V < 14.0$.

The UVES spectrograph was used in the RED 580 setting. The spectra have a spectral coverage of $\sim$2000 Å with the central wavelength at 5800 Å. The typical signal to noise ratio is S/N $\sim 100 - 120$.

Data were reduced using UVES pipelines (Ballester et al. 2000), including bias subtraction, flat-field correction, wavelength calibration, sky subtraction and spectral rectification. Stars were carefully selected from high quality photometric $UBVI_C$ observations by Momany et al. (2003) obtained with the Wide Field Imager (WFI) camera at the ESO/MPI 2.2m telescope (total field of view 34×33 arcmin^2) coupled with infrared JHK 2MASS photometry (Skrutskie et al. 2006). Given the spatially variable interstellar reddening across the cluster (Cudworth & Rees 1990; Drake et al. 1994; Kemp et al. 1993; Lyons et al. 1995; and I99) we have corrected our CMDs for this effect (as done in Sarajedini et al. 2007). Fig. 2.1 shows the position of the target stars on the corrected B vs (B-I) CMD.

2.2 Radial velocities and membership

In the present work, radial velocities were used as the membership criterion since the cluster stars all have similar motion with respect to the observer. The radial velocities (v_r) of the stars were measured using the IRAF FXCOR task, which cross-correlates the object spectrum with a template. As a template, we used a synthetic spectrum obtained through the spectral synthesis code SPECTRUM (see http://www.phys.appstate.edu/spectrum/spectrum.html for more details), using a Kurucz model atmosphere with roughly the mean atmospheric parameters of our stars $T_{eff} = 4500$ K, log(g) = 2.0, $v_t = 1.4$ km/s, [Fe/H] $= -1.10$. At the end, each radial velocity was corrected to the heliocentric system. We calculated a first approximation mean velocity and the r.m.s (σ) of the velocity distribution. Stars showing v_r out of more than 3σ from the mean value were considered probable field objects and rejected, leaving us with

105 UVES spectra of probable members. After this procedure, we obtained a new mean radial velocity of 70.6 ± 1 km/s from all the selected spectra, which agrees well with the values in the literature (Harris 1996, Peterson et al. 1995).

2.3 Abundance analysis

The chemical abundances for all elements, with the exception of Oxygen, were obtained from the equivalent widths (EWs) of the spectral lines. An accurate measurement of EWs first requires a good determination of the continuum level. Our relatively metal-poor stars, combined with our high S/N spectra, allowed us to proceed in the following way. First, for each line, we selected a region of 20 Å centered on the line itself (this value is a good compromise between having enough points, i. e. a good statistic, and avoiding a too large region where the spectrum can be not flat). Then we built the histogram of the distribution of the flux where the peak is a rough estimation of the continuum. We refined this determination by fitting a parabolic curve to the peak and using the vertex as our continuum estimation. Finally, the continuum determination was revised by eye and corrected by hand if a clear discrepancy with the spectrum was found. Then, using the continuum value previously obtained, we fit a Gaussian curve to each spectral line and obtained the EW from integration. We rejected lines if affected by bad continuum determination, by non-gaussian shape, if their central wavelength did not agree with that expected from our linelist, or if the lines were too broad or too narrow with respect to the mean FWHM. We verified that the gaussian shape was a good approximation for our spectral lines, so no lorenzian correction was applied. The typical error for these measurements is 3.6 mÅ, as obtained from the comparison of the EWs measured on stars having similar atmospheric parameters (see Sect. 5.1 for further details).

2.3.1 Initial atmospheric parameters

Initial estimates of the atmospheric parameters were derived from WFI BVI photometry. First-guess effective temperatures (T_{eff}) for each star were derived from the T_{eff}-color relations (Alonso et al. 1999). $(B-V)$ and $(V-I)$ colors were de-reddened using a reddening of $E(B-V) = 0.36$ (Harris 1996). Surface gravities (log(g)) were obtained from the canonical equation:

$$\log(g/g_{\odot}) = \log(M/M_{\odot}) + 4 \cdot \log(T_{eff}/T_{\odot}) - \log(L/L_{\odot})$$

where the mass $M/M_{\odot}$ was derived from the spectral type (derived from T_{eff}) and the luminosity class of stars (in this case we have a III luminosity class)

through the grid of Straizys & Kuriliene (1981). The luminosity $L/L_{\odot}$ was obtained from the absolute magnitude M_V, assuming an apparent distance modulus of $(m - M)_V = 12.83$ (Harris 1996). The bolometric correction (BC) was derived by adopting the relation $BC - T_{eff}$ from Alonso et al. (1999).
Finally, microturbolence velocity (v_t) was obtained from the relation (Gratton et al. 1996):

$$v_t \text{ (km/s)} = 2.22 - 0.322 \cdot \log(g)$$

These atmospheric parameters are only initial guesses and are adjusted as explained in the following Section.

2.3.2 Chemical abundances

The Local Thermodynamic Equilibrium (LTE) program MOOG (Sneden, 1973) was used to determine the metal abundances.

The linelists for the chemical analysis were obtained from the VALD database (Kupka et al. 1999) and calibrated using the Solar-inverse technique. For this purpose we used the high resolution, high S/N Solar spectrum obtained at NOAO (*National Optical Astronomy Observatory*, Kurucz et al. 1984). We used the model atmosphere interpolated from the Kurucz (1992) grid using the canonical atmospheric parameters for the Sun: $T_{eff} = 5777$ K, $\log(g) = 4.44$, $v_t = 0.80$ km/s and [Fe/H] = 0.00.

The EWs for the reference Solar spectrum were obtained in the same way as the observed spectra, with the exception of the strongest lines, where a Voigt profile integration was used. In the calibration procedure, we adjusted the value of the line strength log(gf) of each spectral line in order to report the abundances obtained from all the lines of the same element to the mean value. The chemical abundances obtained for the Sun are reported in Tab. 2.1. The derived Na and Mg abundances were corrected for the effects of departures from the LTE assumption, using the prescriptions by Gratton et al. (1999).

With the calibrated linelist, we can obtain refined atmospheric parameters and abundances for our targets. Firstly model atmospheres were interpolated from the grid of Kurucz models by using the values of T_{eff}, $\log(g)$, and v_t determined as explained in the previous section. Then, during the abundance analysis, T_{eff}, v_t and $\log(g)$ were adjusted in order to remove trends in Excitation Potential (E.P.) and equivalent widths vs. abundance respectively, and to satisfy the ionization equilibrium. T_{eff} was optimized by removing any trend in the relation between abundances obtained from the FeI lines with respect to the E.P. The optimization of $\log(g)$ was done in order to satisfy the ionization equilibrium of species ionized differently: we have used FeI and FeII lines for

this purpose. We changed the value of log(g) until the following relation was satisfied:

$$\log\epsilon(\mathrm{FeII})_{\odot} - \log\epsilon(\mathrm{FeI})_{\odot} = \log\epsilon(\mathrm{FeII})_{*} - \log\epsilon(\mathrm{FeI})_{*}$$

We optimized v_t by removing any trend in the relation abundance vs. EWs of the spectral lines. This iterative procedure allowed us to optimize the values of atmospheric parameters on the basis of spectral data, independent of colors. This is an important advantage for those clusters, as M4, that are projected in regions characterized by a differential reddening.

The adopted atmospheric parameters, together with the coordinates, the U, B, V, I_C, and the 2MASS J, H, K magnitudes, can be found in the on-line table (http://adsabs.harvard.edu/abs/2008yCat..34900625M). All the reported magnitudes are not corrected for differential reddening.

Having T_{eff} determinations independent of colors, we can verify whether the T_{eff}-scale is affected by systematic errors. For this purpose we used the T_{eff} and [Fe/H] of our stars (see Sec. 6.1) to obtain intrinsic B − V colors from Alonso's relations. These colors were compared with WFI photometry corrected for differential reddening. We obtained a reddening of:

$$E(B-V) = +0.34 \pm 0.02$$

This value agrees well with the E(B − V) = 0.36 of Harris (1996) and with I99 who find E(B − V) = 0.33 ± 0.01. Therefore, we conclude that our T_{eff}-scale is

TABLE 2.1— Measured Solar abundances ($\log\epsilon(X) = \log(N_X/N_H) + 12$).

Element	UVES	lines
OI	8.83	1
NaI_{NLTE}	6.32	4
MgI_{NLTE}	7.55	3
AlI	6.43	2
SiI	7.61	12
CaI	6.39	16
TiI	4.94	33
TiII	4.96	12
CrI	5.67	32
FeI	7.48	145
FeII	7.51	14
NiI	6.26	47
BaII	2.45	2

not affected by strong systematic errors.
Finally we present a $v_t - \log(g)$ relation obtained from our data:

$$v_t = -(0.254 \pm 0.016) \cdot \log(g) + (1.930 \pm 0.035)$$

It gives a mean microturbolence velocity 0.15 km/s lower than that given by Gratton et al. (1996), but this is not a surprise because also in other papers (Preston et al. 2006) Gratton et al. (1996) was found to overestimate the microturbolence, especially in our T_{eff} regime. We underline that our formula is valid for objects in the same T_{eff}-log(g) regime as out targets, i.e. cold giant stars.

2.3.3 The O synthesis

Instead of using the EW method, we measured the O content of our stars by spectral synthesis. This method is necessary because of the blending of the target O line at 6300 Å with other spectral lines (mainly the Ni transition at 6300.34 Å). For this purpose, we used a linelist from the VALD archive calibrated on the NOAO Solar spectrum as done before for the other elements, but in this case we changed the log(gf) parameter of our spectral lines in order to obtain a good match between our synthetic spectrum and the observed one.

With the calibrated linelist, it is possible to establish the O content of our targets. To this aim, we used the standard MOOG running option *synth* that computes a set of trial synthetic spectra and matches these to the observed spectrum. The synthetic spectra were obtained by using the atmospheric parameters derived in the previous section. In this way, the Oxygen abundances were deduced by minimization of the observed-computed spectrum difference. An example of a spectral synthesis is plotted in Fig. 2.2 where the spectrum of the observed star #34240 (thick line) is compared with synthetic spectra (thin lines) computed for O abundances [O/Fe]= +0.30, +0.47, and +0.60 dex. In the plotted spectral range, the observed spectrum is contaminated by two telluric features (not present in the models), but none affecting the O line.

The O line is faint, and we could measure the O content only for a subsample of 93 stars. In the remaining 12 spectra, the bad quality of the Oxygen line prevented us from measuring accurate O abundance.

2.4 Results

The wide spectral range of the UVES data allowed us to derive the chemical abundances of several elements. The mean abundances for each element are listed in Tab. 2.2 together with the error of the mean, the rms scatter and the

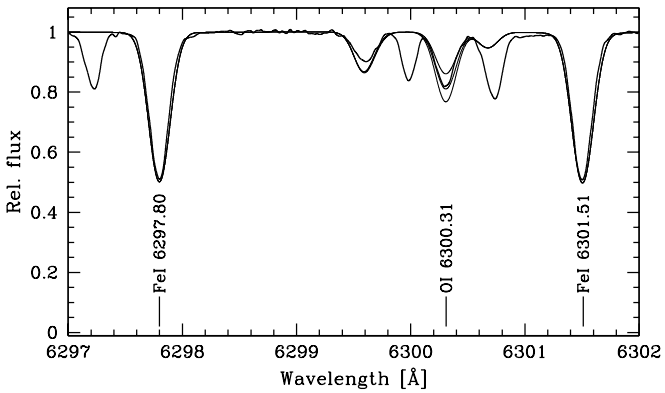

FIGURE 2.2— Spectrum of the star #34240, compared with synthetic spectra in the region 6297-6302 Å, which includes the Oxygen line at 6300.31 Å. Synthetic spectra were computed for O abundances [O/Fe] = +0.30, +0.47, and +0.60 dex. Thick line is the observed spectrum, thin lines are the synthetic ones.

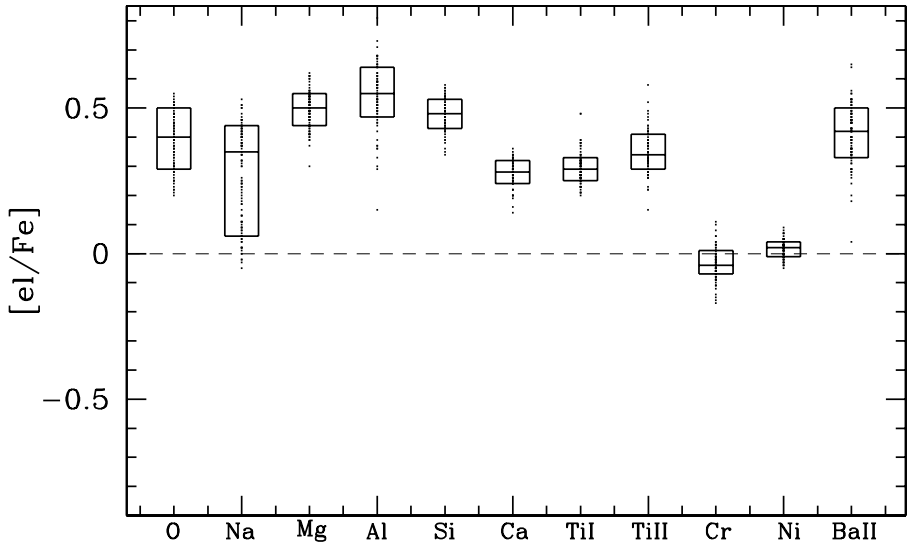

FIGURE 2.3— Box plot of the M4 giant star element abundances from UVES data. For each box the central horizontal line is the median of the data, while the upper and lower lines indicate the higher and lower 1σ value respectively. The points represent the individual measurements.

number of measured stars (N_{stars}). The rms scatter (hereafter σ_{obs}) is assumed to be the 68.27th percentile of the distribution of the measures of the single stars and the error of the mean is the rms divided by $\sqrt{N_{stars} - 1}$. In the last column the abundances derived by I99 were listed as a comparison.

The derived Na and Mg abundances were corrected for the effects of departures from the LTE assumption (NLTE correction) using the prescriptions by Gratton et al. (1999), as done for the Sun. In the paper all the used Na and Mg abundances are NLTE corrected, also were not explicitely indicated. The mean NLTE corrections obtained for [Na/Fe] and [Mg/Fe] are -0.02 dex and $+0.07$ dex, respectively. For the Fe abundance, we do not distinguish between the results obtained from I and II ionization stages, because their values are necessarily the same in the chosen method.

Chemical abundances for the single stars are listed in the on-line table (http://adsabs.harvard.edu/abs/2008yCat..34900625M). A plot of our measured abundances is shown in Fig. 2.3, where, for each box, the central horizontal line is the median values for the element, and the upper and lower lines indicate the 1σ values higher and lower than the median values, respectively. The points represent individual measurements.

TABLE 2.2— The average abundances of M4 stars The results by I99 are shown for comparison in Column 5.

	This work			I99
		σ_{obs}	N_{stars}	
[OI/Fe]	$+0.39 \pm 0.01$	0.09	93	$+0.25 \pm 0.03$
$[NaI/Fe]_{NLTE}$	$+0.27 \pm 0.02$	0.17	105	$+0.22 \pm 0.05$
$[MgI/Fe]_{NLTE}$	$+0.50 \pm 0.01$	0.06	105	$+0.44 \pm 0.02$
[AlI/Fe]	$+0.54 \pm 0.01$	0.11	87	$+0.64 \pm 0.03$
[SiI/Fe]	$+0.48 \pm 0.01$	0.05	105	$+0.55 \pm 0.02$
[CaI/Fe]	$+0.28 \pm 0.01$	0.04	105	$+0.26 \pm 0.02$
[TiI/Fe]	$+0.29 \pm 0.01$	0.05	105	$+0.30 \pm 0.01$
[TiII/Fe]	$+0.35 \pm 0.01$	0.06	105	$+0.30 \pm 0.01$
[CrI/Fe]	-0.04 ± 0.01	0.05	105	–
[FeI/H]	-1.07 ± 0.01	0.05	105	-1.18 ± 0.00
[NiI/Fe]	$+0.02 \pm 0.01$	0.03	105	$+0.05 \pm 0.01$
[BaII/Fe]	$+0.41 \pm 0.01$	0.09	103	$+0.60 \pm 0.02$

2.4.1 Internal errors associated to the chemical abundances

The measured abundances of of every element vary from star to star as a consequence of both measurement errors and intrinsic star to star abundance variations. In this section, our final goal is to search for evidence of intrinsic abundance dispersion in each element by comparing the observed dispersion $\sigma_{\rm obs}$ and that produced by internal errors ($\sigma_{\rm tot}$). Clearly, this requires an accurate analysis of all the internal sources of measurement errors. We remark here that we are interested in star-to-star intrinsic abundance variation, i.e. we want to measure the internal intrinsic abundance spread of our sample of stars. For this reason, we are not interested in external sources of error which are systematic and do not affect relative abundances.
It must be noted that two sources of errors mainly contribute to $\sigma_{\rm tot}$. They are:

- the errors $\sigma_{\rm EW}$ due to the uncertainties in the EWs measures;
- the uncertainty $\sigma_{\rm atm}$ introduced by errors in the atmospheric parameters adopted to compute the chemical abundances.

In order to derive an estimate of σ_{EW}, we consider that EWs of spectral lines in stars with the same atmospherical parameters and abundances are expected to be equal; any difference in the observed EWs can be attributed to measurements errors. Hence, in order to estimate $\sigma_{\rm EW}$, we applied the following procedure:

- Select two stars (#33683 and #33946) from our sample characterized by exactly the same $T_{\rm eff}$, and log(g), $v_{\rm t}$, [Fe/H] within a range of 0.05;
- Compare the EWs of the iron spectral lines in these two stars and calculate the standard deviation of the distribution of the differences between the EWs divided by $\sqrt{2}$. We found a value of 3.6 mÅ that we assume to represent our estimate for the errors in the EWs. Iron lines were selected because Fe abundance has always been found to be the same for stars in GCs, with the exception of ω Cen. This means that any differences in the EW for the same couple of lines is due only to measurement errors;
- Calculate the corresponding error in abundance measurements ($\sigma_{\rm EW}$) by using a star (#21728) at intermediate temperature, assumed to be representative of the entire sample. To this aim, we selected two spectral lines for each element in order to cover the whole E.P. range, changed the EWs by 3.6 mÅ and calculated the corresponding mean chemical abundance variation. This number divided by $\sqrt{\rm N_{lines}-1}$ is our $\sigma_{\rm EW}$. Results are listed in Tab. 2.3.

A more elaborate analysis is required to determine $\sigma_{\rm atm}$. We followed two different approaches.

In order to better understand the method, it is important to summarize the role of the atmospheric parameters in the determination of chemical abundances. As fully described in sections 4.1, the best estimate of chemical abundances, $T_{\rm eff}$, $v_{\rm t}$ and log(g) obtained from the spectrum of a single star are those that satisfy at the same time three conditions:

- removing any trend from the straight line that best fits the abundances vs. E.P.;
- removing any trend from the straight line that best fits the abundances as a function of equivalent widths;
- satisfy the ionization equilibrium through the condition [FeI/H] = [FeII/H].

Therefore, any error in the slope of the best fitting lines and in FeI/FeII determinations produces an error on the measured abundance.

In order to derive the error in temperature we applied the following procedure. First we calculated, for each star, the errors associated with the slopes of the best least squares fit in the relations between abundance vs. E.P. The average of the errors corresponds to the typical error on the slope. Then, we selected three stars representative of the entire sample (#29545, #21728, and #34006) with high, intermediate, and low $T_{\rm eff}$, respectively. For each of them, we fixed the other parameters and varied the temperature until the slope of the line that best fits the relation between abundances and E.P. became equal to the respective mean error. This difference in temperature represents an estimate of the error in temperature itself. The value we found is $\Delta T_{\rm eff} = 40$ K.

The same procedure was applied for $v_{\rm t}$, but using the relation between abundance and EWs. We obtained a mean error of $\Delta v_{\rm t} = 0.06$ km/s.

Since log(g) was obtained by imposing [FeI/H] = [FeII/H], and [FeI/H] and [FeII/H] have averaged uncertainties of $\overline{\sigma_{\rm star}[{\rm FeII/H}]}$ and $\overline{\sigma_{\rm star}[{\rm FeI/H}]}$ (where $\sigma_{\rm star}$[Fe/H] is the dispersion of the iron abundances derived by the various spectral lines in each spectrum and given by MOOG, divided by $\sqrt{N_{\rm lines} - 1}$), in order to associate an error to the measures of gravity we have varied the gravity of the three representative stars such that the relation:

$$[{\rm FeI/H}] - \overline{\sigma_{\rm star}[{\rm FeI/H}]} = [{\rm FeII/H}] + \overline{\sigma_{\rm star}[{\rm FeII/H}]}$$

was satisfied. The obtained mean error is Δ[log(g)]=0.12.

Once the internal errors associated to the atmospheric parameters were calculated, we re-derived the abundances of the three reference stars by using the following combination of atmospheric parameters:

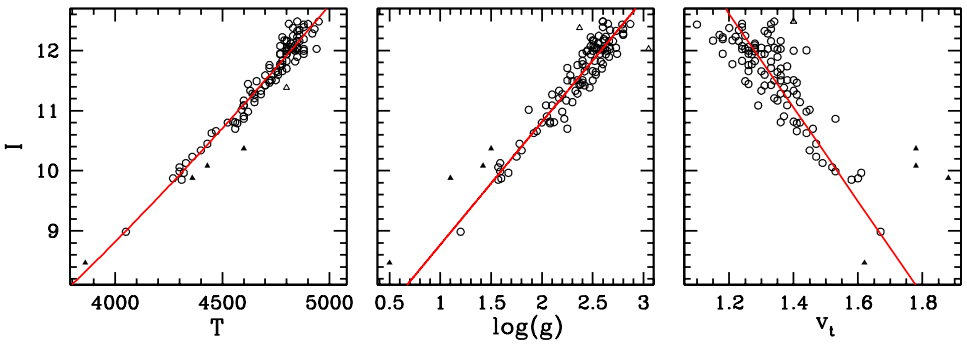

FIGURE 2.4— I magnitude (corrected for differential reddening) as a function of the atmospheric parameters for our target stars. For T_{eff} the data were fitted with a parabolic curve, for log(g) and v_t with a straight line.

- ($T_{eff} \pm \Delta(T_{eff})$, log(g), v_t)
- (T_{eff}, log(g) $\pm \Delta$(log(g)), v_t)
- (T_{eff}, log(g), $v_t \pm \Delta(v_t)$)

where T_{eff}, log(g), v_t are the measures determined in Section 4.2.

The resulting errors in the chemical abundances due to uncertainties in each atmospheric parameter are listed in Tab. 2.3 (columns 2, 3 and 4). The values of σ_{atm} (given by the squared sum of the uncertainties introduced by each single parameter) listed in column 5 are our final estimates of the error introduced by the uncertainties of all the atmospheric parameters on the chemical abundance measurements.

We also used a second approach to estimate σ_{atm} as confirmation of the first method. In order to verify our derived uncertainties related to the temperature, gravity and microturbolence, we considered that RGB stars with the same I magnitude must have the same atmospheric parameters. Hence, we started by plotting the magnitude I as a function of T_{eff}, log(g) and v_t as shown in Fig. 2.4. We see in this figure that the typical internal error in our I photometry (~ 0.01 mag) translates into an error in temperature of ~ 3 K, in log(g) of ~ 0.005, and in v_t of ~ 0.002 km/s, each of which is absolutely negligible. The data were fitted by a parabolic curve in the case of T_{eff}, and by straight lines in the cases of log(g) and v_t. We determined the differences between the T_{eff}, log(g) and v_t of each star and the corresponding value on the fitting curve. Assuming the 68.27th percentile of the absolute values of these differences as an estimate of the dispersion of the points around the fitting curve, all the stars with a distance

from the curve larger than 3σ were rejected (the open triangles in Fig. 2.4). The four probable AGB stars (filled triangles) that are evident on the B − (B − I) CMD of Fig. 2.1 were also rejected. With the remaining stars, the curve was refitted and the differences between the atmospheric parameters of the stars and the fit were redetermined. The 68.27th percentile of their absolute values are our estimate of the uncertainties on the atmospheric parameters.

By using this second method we obtained the uncertainties ΔT_{eff} =37 K, $\Delta\log(g)$ =0.12 and Δv_t =0.06 km/s, consistent with the ones determined with the first method.

TABLE 2.3— Sensitivity of derived UVES abundances to the atmospheric parameters and EWs. We reported the total error due to the atmospheric parameters (σ_{atm}), due to the error in EW measurement (σ_{EW}), the squared sum of the two (σ_{tot}), and the observed dispersion (σ_{obs}) for each element. The FeII observed dispersion is not reported because it is necessarily the same as FeI due to the method used in this paper to obtain atmospheric parameters.

	ΔT_{eff}(K)	$\Delta\log(g)$	Δv_t (km/s)	σ_{atm}	σ_{EW}	σ_{tot}	σ_{obs}
	+40	+0.12	+0.06				
[OI/Fe]	–	–	–	–	–	0.04	0.09
[NaI/Fe]	+0.00	−0.01	+0.02	0.02	0.04	0.04	0.17
[MgI/Fe]	−0.01	−0.01	+0.01	0.02	0.06	0.06	0.06
[AlI/Fe]	−0.01	−0.02	+0.02	0.03	0.06	0.07	0.11
[SiI/Fe]	−0.04	+0.03	+0.02	0.05	0.03	0.06	0.05
[CaI/Fe]	+0.01	−0.02	+0.00	0.02	0.02	0.03	0.04
[TiI/Fe]	+0.04	−0.02	+0.00	0.04	0.02	0.04	0.05
[TiII/Fe]	+0.03	−0.01	−0.01	0.03	0.05	0.06	0.06
[CrI/Fe]	+0.02	−0.01	+0.00	0.02	0.06	0.06	0.05
[FeI/H]	+0.04	+0.00	−0.03	0.05	0.01	0.05	0.05
[FeII/H]	−0.03	+0.06	−0.01	0.07	0.04	0.08	–
[NiI/Fe]	−0.01	+0.02	+0.01	0.02	0.02	0.03	0.03
[BaII/Fe]	+0.05	−0.04	−0.03	0.07	0.05	0.09	0.09

Our best estimate of the total error associated to the abundance measures is calculated as

$$\sigma_{tot} = \sqrt{\sigma_{EW}^2 + \sigma_{atm}^2}$$

listed in the column 7 of Tab. 2.3. For O σ_{tot} was obtained in a different way since its measure was not based on the EW method (see Section 6.4). In all the plots for the error bars associated with the measure of abundance we adopted σ_{tot}.

In addition, systematic errors on abundances can be introduced by systematic errors in the scales of T_{eff}, log(g), v_t, and by deviations of the real stellar atmosphere from the model (i.e. deviations from LTE). A study of the systematic effects goes beyond the purposes of this study, where we are more interested in internal star to star variation in chemical abundances.

Comparing σ_{tot} with the observed dispersion σ_{obs} (column 8) at least for the abundance ratios [Na/Fe], [O/Fe] and [Al/Fe], we found σ_{obs} significantly larger than σ_{tot}, suggesting the presence of a real spread in the content of these elements within the cluster.

2.5 The chemical composition of M4

In the following sections, we will discuss in detail the measured chemical abundances. In addition, we will use the abundances of C and N from the literature to extend our analysis to those elements. The errors we give here are only internal. External ones can be estimated by comparison with other works (see Tab. 2.2).

2.5.1 Iron and iron-peak elements

The weighted mean of the [Fe/H] found in the 105 cluster members is

$$[\mathrm{Fe/H}] = -1.07 \pm 0.01 \text{ dex}$$

The other Fe-peak elements (Ni and Cr) show roughly the Solar-scaled abundance.

The agreement between σ_{obs} and σ_{tot} (see Tab. 2.3), allows us to conclude that there is no evidence for an internal dispersion in the iron-peak element content, suggesting that this cluster is homogeneous in metallicity down to the σ_{obs} level.

2.5.2 α elements

The chemical abundances for the α elements O, Mg, Si, Ca, and Ti are listed in Tab. 2.2. All the α elements are overabundant. Ca and Ti are enhanced by $\sim$0.3 dex, while Si and Mg by $\sim$0.5 dex. The results for [O/Fe] will be discussed in detail in Section 6.4.

Previous investigators (GQO86, BW92 and I99) have also found significant overabundances for both Si and Mg. In particular, for [Si/Fe] they found values higher than 0.5 dex, slightly higher than our results, while our [Mg/Fe] = 0.50 lies in the middle of the literature results that range between 0.37 (BW92) and 0.68 dex (GQO86). As noted by I99, the abundances of these two elements in

M4 are higher if compared to the ones found in other globular clusters showing a similar metallicity, i. e. M5 (Ivans et al. 2000). I99 suggest that the higher abundances in M4 should be primordial, e.g. due to the chemical composition of the primordial site from which the cluster formed.

For [Ca/Fe] we obtained a scatter of 0.04 dex, differing from I99, who found σ=0.11 dex (see discussion in Section 6.6). TiI and TiII show the same abundance within 3σ (see Tab. 2.2), with a mean of the two different ionized species of $[\mathrm{Ti/Fe}] = +0.32 \pm 0.04$.

The average of all the α elements, gives an α enhancement for M4 of:

$$[\alpha/\mathrm{Fe}] = +0.39 \pm 0.05 \text{ dex}$$

In this case the agreement between σ_{obs} and σ_{tot} again allows us to conclude that, down to the σ_{obs} level, there is no evidence of internal dispersion for these elements, with the exception of O, which we will discuss in Section 6.4.

2.5.3 Barium

As in I99 and BW92, we have found a strong overabundance of Ba. We have $[\mathrm{Ba/Fe}] = 0.41 \pm 0.01$ which is about 0.2 dex smaller than in I99. In any case, our results confirm that Ba is significantly overabundant in M4, at variance with what found by GQO86, possibly solving this important issue. As deeply discussed by I99, this high Barium content cannot be accounted for mixing processes, but must be a signature of the presence of s-process elements in the primordial material from which M4 stars formed. The excess of s-process elements provides some support to the idea that the formation of the stars we now observe in M4 happened after intermediate-mass AGB stars have polluted the environment, or that it lasted for long enough to allow intermediate-mass AGB stars to strongly pollute the lower mass forming stars. We do not find any significant dispersion in Ba content for the bulk of our target stars, though there are a few outliers worth further discussion (see below).

2.5.4 Na-O anticorrelation

Variations in light element abundances is common among GCs, and is also present in M4. In particular, Sodium and Oxygen have very large dispersions: we obtained $\sigma_{[\mathrm{Na/Fe}]}$=0.17 and $\sigma_{[\mathrm{O/Fe}]}$=0.09. A large star to star scatter in Sodium and Oxygen abundance in M4 was found also in other previous studies (I99, D92). Sodium and Oxygen show the typical anticorrelation found in many other GCs (Gratton et al. 2004), as shown in Fig. 2.5, where the [Na/Fe] values are plotted as a function of [O/Fe]. The open blue circles represent the 12

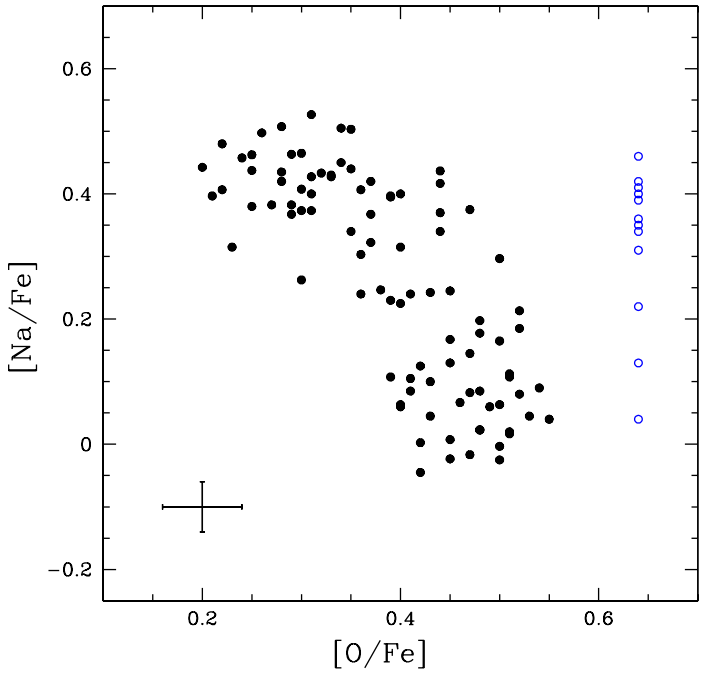

FIGURE 2.5— [Na/Fe] vs. [O/Fe] abundance ratios. The error bars represent the typical errors $\sigma_{\rm tot}$ from Tab. 2.3.

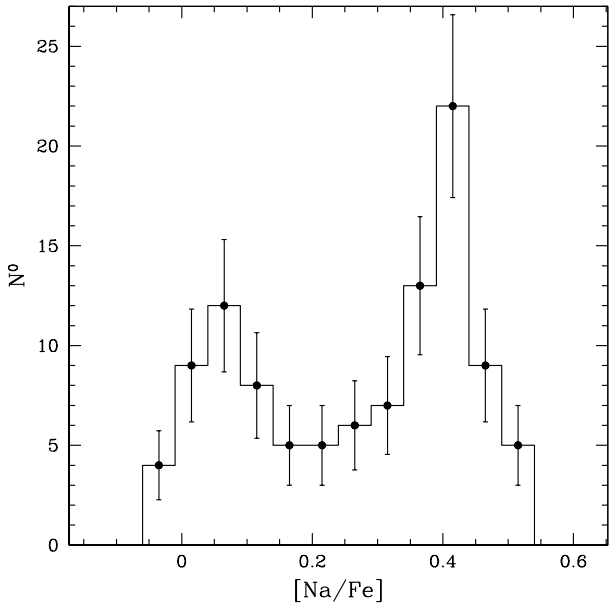

FIGURE 2.6— Histogram of the distribution of the [Na/Fe] abundances. The error bars represent the Poisson errors.

stars for which it was not possible to obtain a good estimate of the Oxygen abundance.

Since the Oxygen abundance was derived from just one spectral line, we adopted the following the following procedure to derive a raw estimate of the typical error $\sigma_{\rm tot}$ associated with each measure: we selected the group of stars with [Na/Fe]<0.20, assuming them to be homogeneous in their O content. Under this hypothesis, the dispersion in O can be assumed to be due to the random error associated with the measured O abundance. We obtained $\sigma_{\rm [O/Fe]} = 0.04$ dex, which corresponds to the error bar size in Fig. 2.5 and to the $\sigma_{\rm tot}$ in Tab. 2.3. The only previous study showing the Na-O anticorrelation in M4 was that by I99. They analysed [Na/Fe] and [O/Fe] abundances for 24 giant stars from high resolution spectra taken at the Lick and McDonald Observatories. With respect to their work, our dispersion for [O/Fe] is quite a bit smaller (0.09 dex against their value of 0.14 dex), and our average value is larger (see Tab. 2.2). We have seven stars in common with their high resolution sample, and another seven with their medium resolution sample for which they derived only the Oxygen abundance. The comparison between their results and the present ones are listed in Tab. 2.4, where the last two columns give the dif-

ferences between I99 and our results. We can note that our abundances are systematically higher than those of I99. The effect is higher for the [O/Fe], but is present for Sodium too, and could reflect the difference of ~ 0.1 dex we found for the iron with respect to I99. This systematic difference does not affect the shape of the Na-O anticorrelation, but it does emphasize the overabundance of O in M4 stars with respect to other clusters with similar metallicity, as already noticed by I99: M4 stars formed in an environment particularly rich in O and possibly in Na.

The most interesting result of our investigation is that, thanks to the large number of stars in our sample, we can show that the [Na/Fe] distribution is bimodal (Fig. 2.6). Setting an arbitrary separation between the two peaks in Fig. 2.6 at $\sim$0.2 dex, we obtain, for the two groups of stars with higher and lower Na content, a mean [Na/Fe] $= 0.38 \pm 0.01$ and [Na/Fe] $= 0.07 \pm 0.01$, respectively.

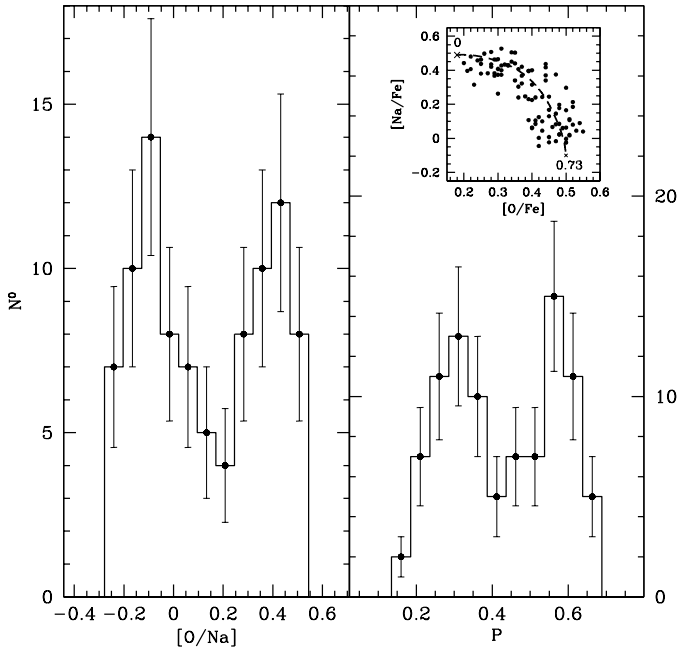

FIGURE 2.7— Left: Distribution of stars along the Na-O anticorrelation represented by the [O/Na] ratios. Right: Distribution of the projected position P of stars on the parametric curve plotted in the inset pannel. The coordinates of the edges of the curve are indicated.

In correspondence with the two peaks in the [Na/Fe] distribution, there are

TABLE 2.4— Comparison between our [Na/Fe] and [O/Fe] ($[el/Fe]_{tw}$) and those of I99 ($[el/Fe]_{I99}$) for the stars in common. The Oxygen values were compared both with the high resolution sample of I99 ($[O/Fe]^{(a)}_{I99}$) and with the medium resolution sample ($[O/Fe]^{(b)}_{I99}$). The last three columns give the differences $[el/Fe]_{tw} - [el/Fe]_{I99}$.

ID	$[O/Fe]_{tw}$	$[O/Fe]^{(a)}_{I99}$	$[O/Fe]^{(b)}_{I99}$	$[Na/Fe]_{tw}$	$[Na/Fe]^{(a)}_{I99}$	$\Delta O^{(a)}$	$\Delta O^{(b)}$	ΔNa
L1411	+0.28	+0.20	+0.07	+0.51	+0.43	+0.08	+0.21	+0.08
L1501	+0.34	+0.10	−−	+0.51	+0.42	+0.24	−−	+0.09
L1514	+0.50	+0.41	+0.41	+0.17	+0.01	+0.09	+0.09	+0.16
L2519	+0.48	+0.37	+0.37	+0.02	−0.19	+0.11	+0.11	+0.21
L2617	+0.25	+0.01	+0.07	+0.44	+0.50	+0.24	+0.18	−0.06
L3612	+0.25	+0.10	+0.12	+0.46	+0.47	+0.15	+0.13	−0.01
L3624	+0.48	+0.29	+0.27	+0.18	+0.10	+0.19	+0.21	+0.08
L1403	+0.31	−−	+0.22	+0.53	−−	−−	+0.09	−−
L2410	+0.39	−−	+0.32	+0.11	−−	−−	+0.07	−−
L2608	+0.43	−−	+0.37	+0.24	−−	−−	+0.06	−−
L1617	+0.24	−−	+0.17	+0.46	−−	−−	+0.07	−−
L4415	+0.44	−−	+0.37	+0.37	−−	−−	+0.07	−−
L4421	+0.28	−−	+0.07	+0.44	−−	−−	+0.21	−−
L4413	+0.22	−−	+0.27	+0.48	−−	−−	−0.05	−−
mean	+0.35	+0.21	+0.24	+0.35	+0.25	+0.16	+0.11	+0.08

also two [O/Fe] groups (Fig. 2.5): the first group is centered at [O/Fe] ~ 0.30, while the second is at [O/Fe] ~ 0.47, with a few stars having intermediate Oxygen abundance.

We have followed two methods to trace the distribution of the stars on the Na-O plane. The first method uses the ratio [O/Na] between the O and the Na abundances (Carretta et al. 2006) which appears to be the best indicator to trace the star distribution along the Na-O anticorrelation, because this ratio continues to vary even at the extreme values along the distribution. The distribution of the [O/Na] is plotted in Fig. 2.7 (left panel). We can identify two bulks of RGB stars in this plot: one at [O/Na] ~ 0.40 and the second one at [O/Na] ~ -0.10. There might be another group of stars between [O/Na]$\sim$0 and [O/Na]$\sim$0.25, but we cannot provide conclusive evidence.

Note that the two groups of stars in the Na-O anticorrelation have their corresponding peaks at [O/Fe] ~ 0.47 and [O/Fe] ~ 0.30, so both groups are O-enhanced.
There are no differences in [Fe/H] content between these two groups of stars: both of them have [Fe/H] $= -1.07$ dex.

We have also analysed the distribution of stars along the Na-O anticorrela-

tion with an alternative procedure whose steps are briefly described below:

- A parametric curve following the observed Na-O distribution as shown in the inset of the right panel of Fig. 2.7 has been traced;
- Each observed point in the Na-O distribution has been projected on the parametric curve;
- For each projected point, the distance (P) from the origin of the parametric curve (indicated with 0 in the inset of the right panel of Fig. 2.7) has been calculated;
- A histogram of the P distance distribution has been constructed.

The histogram is shown in the right panel of Fig. 2.7. In this case also, two peaks are evident: the first one at P $\sim$ 0.28, and the second one at P $\sim$ 0.58.

In conclusion, we obtained the Na-O anticorrelation for a large sample (93 RGB stars) in the globular cluster M4. The distribution of the objects on the Na-O anticorrelation is clearly bimodal.

2.5.5 Mg-Al anticorrelation

Aluminium abundances have been determined from the EWs of the AlI lines at 6696 Å and 6698 Å, and Mg abundances from the EWs of the MgI doublet at 6319 Å, 6318 Å, and of the line at 5711Å. Figure 2.8 shows the [Mg/Fe] as a function of [Al/Fe] and [O/Fe] (upper panels) and [Mg/Fe] and [Al/Fe] as a function of [Na/Fe] (lower panels).

In each panel the red line represents the best least squares fit to the data. The value a is the slope of the best fit straight line y = ax + b. There is no clear Mg-Al anticorrelation (upper left panel of Fig. 2.8), although Al is more spread out than Mg ($\sigma_{[Al/Fe]} = 0.11$ vs. $\sigma_{[Mg/Fe]} = 0.06$). Both Al and Mg are overabundant, with average value of $[Al/Fe] = 0.54 \pm 0.01$ and $[Mg/Fe] = 0.50 \pm 0.01$ (internal errors).

The right-bottom panel of Fig. 2.8 shows that there is a correlation between [Al/Fe] and [Na/Fe] (higher Al abundances for higher Na content), though it is less pronounced than the Na-O anticorrelation. Aluminium spans over a range of $\sim$ 0.4 dex, while Sodium covers a range of $\sim$ 0.6 dex. The spread in Al content of M4 is smaller than in other clusters of similar metallicity, like M5 (Ivans et al. 1999) and M13 (Johnson et al. 2005).
Figure 2.9 shows that there might also be a correlation between the [Al/Fe] and [Ba/Fe].

Mg does not clearly correlate neither with Na (left-bottom panel of Fig. 2.8) nor O (upper-right panel of Fig. 2.8).

The absence of a Mg-Al anticorrelation is somehow surprising, in view of the presence of a strong double peaked Na-O anticorrelation, and of a correlation between Al and Na and possibly Al and Ba. All these correlations seems to indicate the presence of material that has gone through the s-process phenomenon. Assuming that the Na enhancement comes from the proton capture process at the expense of Ne, we can also expect that a similar process is the basis of the Al enhancement at the expense of Mg. Still, we do not find any significant dispersion in the Mg content. This problem has already been noted by I99, who suggested that the required Mg destruction is too low to be measured (see their Section 4.2.2 for further details).

Here we only add that, despite our large sample, neither in the Al nor in the Mg (and Ba) distribution can we see any evidence of the two peaks so clearly visible as in the Na and O distribution. But, in spite of the lack of a clear Mg-Al anticorreletion, we found that Na poor stars have on average higher Mg and lower Al. The difference between the median Mg and Al abundances for the Na-poor and Na-rich samples are: $[\mathrm{Mg/Fe}]_{\mathrm{Na-rich}} - [\mathrm{Mg/Fe}]_{\mathrm{Na-poor}} = -0.04 \pm 0.01$ and $[\mathrm{Al/Fe}]_{\mathrm{Na-rich}} - [\mathrm{Al/Fe}]_{\mathrm{Na-poor}} = +0.08 \pm 0.02$ This should be consistent with the scenario proposed by I99 (see their Sec. 4.2.2 for more details) who predicted that a drop of only 0.05 dex in Mg is needed to account for the observed increase in the abundance of Al. (Obviously this requires the further hypothesis that all the Na enhanced stars are also Al enhanced.)

2.5.6 CN bimodality

In this section we discuss the correlation of the λ3883 CN absorption band strength with Na, O, and Al abundances. Previous studies revealed a trend of Na and Al with the CN band strength. By studying 4 RGB stars from high resolution spectra, D92 found higher Sodium abundances in the two CN-strong stars with respect to the two CN-weak ones (Suntzeff & Smith 1991). I99 found that the Oxygen abundance is anticorrelated with Nitrogen, whereas both Na and Al are more abundant in CN-strong giants than in CN-weak ones.

In our study, two peaks in the Na distribution are evident (see Fig. 2.6), while there is no equally strong pattern in the Al distribution (right bottom panel of Fig. 2.8). The CN band strengths of red giants in M4 have been measured by N81, Suntzeff & Smith (1991), and I99. Smith & Briley 2005 (SB05) have homogenized all the available data for CN band strengths in terms of the S(3839) index, e. g. the ratio of the flux intensities of the Cyanogen band near 3839 Å and the nearby continuum. In the following, we will use the

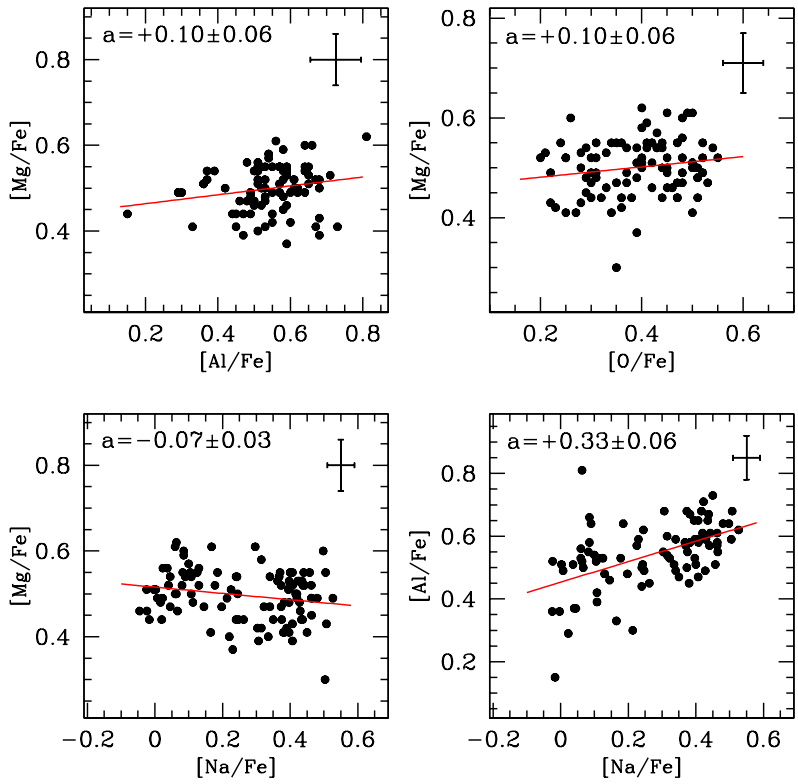

FIGURE 2.8— Bottom panels: [Al/Fe] and [Mg/Fe] abundance ratios are plotted as a function of [Na/Fe]. Upper panels: [Mg/Fe] ratio as a function of [O/Fe] and [Al/Fe]. In each panel the red line is the best least squares fit and a is the slope of this line. The error bars represent the typical errors $\sigma_{\rm tot}$ from Tab. 2.3.

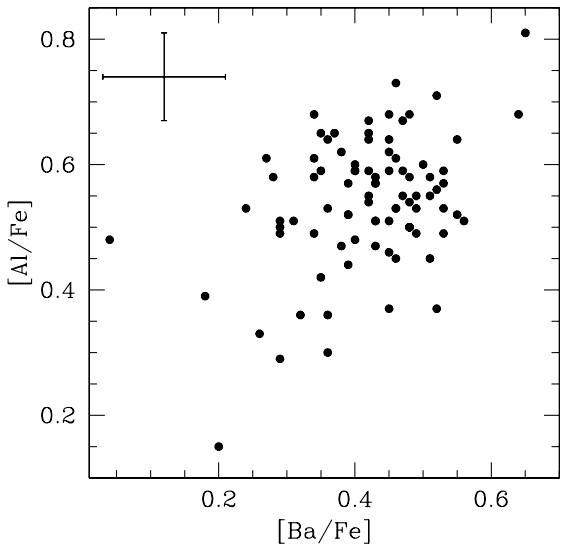

FIGURE 2.9— [Al/Fe] vs. [Ba/Fe] abundance ratios. The error bars represent the typical errors $\sigma_{\rm tot}$ from Tab. 2.3.

S(3839) index calculated by SB05.

In Tab. 2.5 the CN-index S(3839), the [C/Fe] and the [N/Fe] values (taken from SB05 and I99, respectively), and the identification as CN-strong (S), -weak (W), and -intermediate (I), are listed for our target stars with available CN data (34 stars in total). The IDs come from Lee (1977).

For these targets, Table 2.6 lists the mean values of the chemical abundances for CN-S and CN-W(+I) stars. The Na, O, Mg, Al and Ca abundances are from this work, the [C/Fe] values are given by SB05, while the [N/Fe] are the mean values taken from I99 for all their CN-S and CN-W stars, including stars not in common with our sample (there are only five stars in our sample with nitrogen content available). In the last column the differences $\Delta(\mathrm{S}-\mathrm{W})$ between the mean values for CN-S and CN-W(+I) stars are listed.

Fig. 2.10 shows the [Na/Fe], [Al/Fe], [O/Fe], [Mg/Fe] and [Ca/Fe] values obtained in this work as a function of S(3839). In this figure CN-S objects are represented by filled circles, CN-W by open circles, and CN-I by open squares. The dotted lines represent the mean values of the abundances for the CN-S and CN-W(+I) stars; the CN-I stars were included in the CN-W group because of their similar behaviour as is clear from Fig. 2.10. The red lines represent the best least squares fit of the data, and a is the slope of the line. We note that

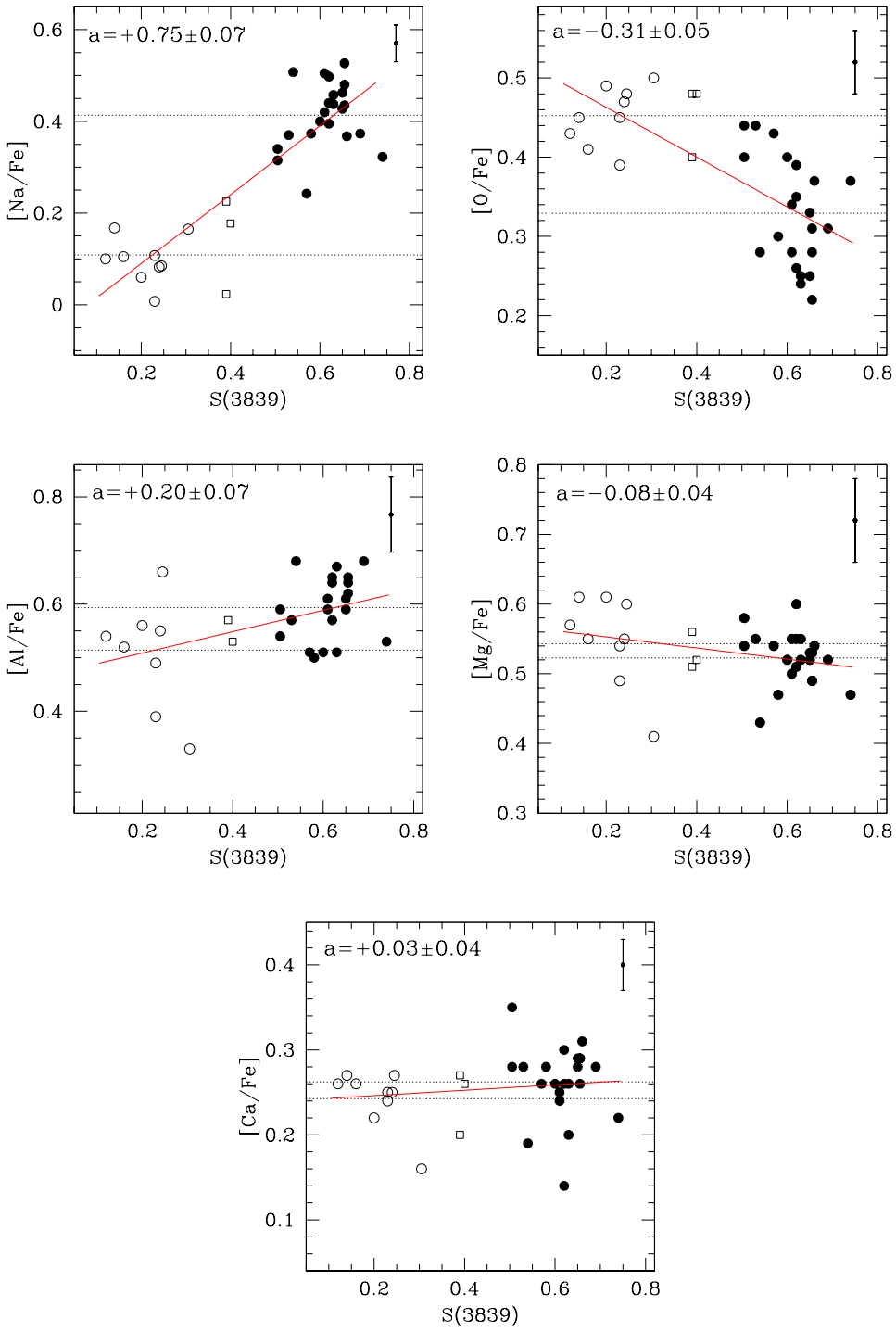

FIGURE 2.10— The abundance ratios [Na/Fe], [O/Fe], [Al/Fe], [Mg/Fe] and [Ca/Fe] are plotted as a function of the CN index S(3839). The filled circles represent the CN-S stars, the open circles the CN-W and the open squares the CN-I ones. In each panel, a is the slope of the straight line of the best least square fit. The error bars represent the typical errors $\sigma_{\rm tot}$ from Tab. 2.3.

the CN-S objects clearly show significantly enhanced Na abundances, while the CN-W(+I) stars have a lower Na content. The three CN-I stars show low [Na/Fe] values typical of CN-weak stars. There is also a systematic difference in Al between CN-weak and CN-strong stars, with CN-strong stars richer in Al content.

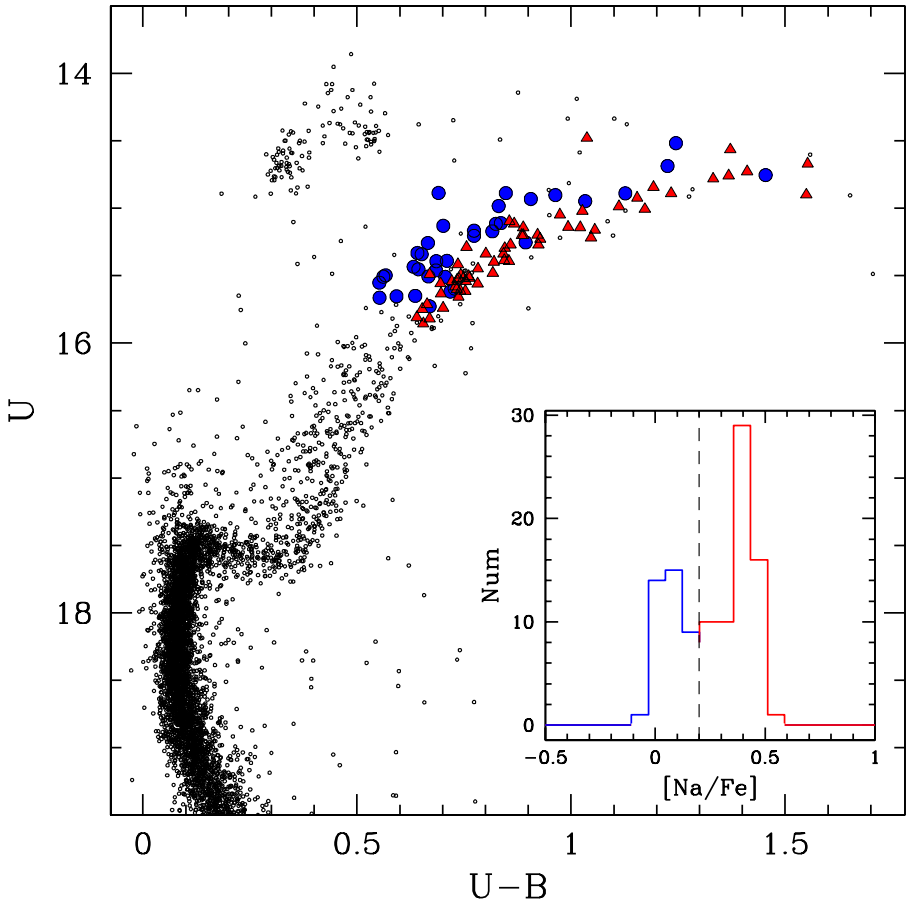

FIGURE 2.11— U vs. $(U - B)$ CMD from WFI photometry. The distribution of the Na content for the UVES stars is shown in the inset. The stars belonging to the two different Na groups are represented in two different colors: the red triangles represent the stars with [Na/Fe] > 0.2 dex, and the blue circles the stars with [Na/Fe] ≤ 0.2 dex.

The CN-W(+I) stars have a higher O content than the CN-S as shown in the upper middle panel of Fig. 2.10. Fig. 2.10 shows some difference in

[Mg/Fe] between the CN-W(+I) and the CN-S stars, with CN-W(+I) stars having slightly higher Mg abundances than the CN-S ones, but this difference is not statistically significant (see Table 2.6).

I99 and D92 also found that the scatter in Ca abundance correlates with the CN strength. I99 found a difference in Ca content between CN-strong and CN-weak stars by 0.08 ± 0.11 dex. To compare, we have also analysed the Ca abundance as a function of the CN strength. In the bottom-right panel of Fig. 2.10, [Ca/Fe] is plotted as a function of S(3839); we can see that the difference between the two groups is 0.02 dex, smaller than what was found by I99 and not statistically significant (see Table 2.6).

TABLE 2.5— CN band strengths and Carbon and Nitrogen abundances for our target stars with C, N and CN measurements in the literature. We use the star identifications from Lee (1977). In the last column, S refers to CN-strong, W CN-weak and I CN-intermediate stars. The C and N abundances are from SB05 and I99, respectively.

ID	S(3839)	CN	[CI/Fe]	[NI/Fe]	ID	S(3839)	CN	[CI/Fe]	[NI/Fe]
L1411	0.54	S	...	...	L2626	0.66	S	...	...
L1403	0.655	S	−0.67	...	L3705	0.20	W	...	...
L1501	0.61	S	...	...	L3706	0.16	W	...	...
L2422	0.69	S	−0.83	...	L2519	0.39	I	−0.50	+0.22
L4404	0.505	S	−0.35	...	L2623	0.245	W	−0.70	...
L1514	0.305	W	−1.12	+0.99	L3721	0.58	S	...	...
L4415	0.53	S	−0.67	...	L2617	0.63	S	−0.77	+1.05
L4416	0.62	S	−0.89	...	L2711	0.65	S	...	...
L4509	0.62	S	−0.44	...	L3730	0.24	W	...	...
L1512	0.61	S	...	...	L3612	0.65	S	−0.73	+1.02
L1617	0.63	S	−0.93	...	L3621	0.23	W	...	...
L1619	0.62	S	...	...	L2608	0.57	S	−0.52	...
L1608	0.60	S	−0.63	...	L3624	0.40	I	−0.67	+0.25
L1605	0.74	S	...	...	L2410	0.23	W	−0.59	...
L4630	0.505	S	−0.62	...	L4413	0.655	S	−0.32	...
L3701	0.39	I	...	...	L4421	0.655	S	−0.83	...
L3404	0.12	W	−0.40	...	L4508	0.14	W	...	...

2.6 Search for evolutionary effects

2.6.1 Abundances along the RGB

According to the results discussed in the previous section, we can define two groups of stars: the Na-rich stars, i. e. those with [Na/Fe] ≥ 0.2 and low Oxygen content which must be associated to the CN-S stars (Fig. 2.10), and the Na-poor stars with higher Oxygen, i. e. those with [Na/Fe] < 0.2, which correspond to the CN-W group. It is instructive to look at the position of the

TABLE 2.6— Mean abundance ratios and relative rms (σ) for the CN-S and CN-W(+I) groups. In the last column the difference between CN-S and CN-W(+I) stars are listed.

[el/Fe]	CN-S	σ	CN-W(+I)	σ	Δ(S − W(+I))
[CI/Fe]	-0.66 ± 0.05	0.19	-0.66 ± 0.11	0.25	+0.00
[NI/Fe]	$+1.08 \pm 0.10$	0.22	$+0.42 \pm 0.19$	0.42	+0.66
[OI/Fe]	$+0.33 \pm 0.01$	0.07	$+0.45 \pm 0.01$	0.04	−0.12
[NaI/Fe]	$+0.41 \pm 0.02$	0.07	$+0.11 \pm 0.02$	0.06	+0.30
[AlI/Fe]	$+0.59 \pm 0.01$	0.06	$+0.51 \pm 0.03$	0.09	+0.08
[MgI/Fe]	$+0.52 \pm 0.01$	0.04	$+0.54 \pm 0.02$	0.06	−0.02
[CaI/Fe]	$+0.26 \pm 0.01$	0.04	$+0.24 \pm 0.01$	0.03	+0.02

stars belonging to these two Na groups on the U vs. $(U-B)$ CMD and on the color-color $(U-B)$ vs. $(B-K)$ diagram (Fig. 2.11 and Fig. 2.12, respectively). The U and B magnitudes come from our WFI photometry, the K magnitude from the 2MASS catalogue. The Na-rich stars are represented by red triangles, while the Na-poor stars by blue circles. The CMD has been corrected for differential reddening (following the same procedure used in Sarajedini et al. 2007) and proper motions. It is clear from Fig. 2.11 that our sample of stars mostly includes RGB stars with only three or four probable AGB stars.

Interestingly enough, the two groups of Na-rich and Na-poor stars form two distinct branches on the RGB. Na-rich stars define a narrow sequence on the red side of the RGB, while the Na-poor sample populates the blue, more spread out portion of the RGB. Even more interestingly, the anomalous broadening of the RGB is visible down to the base of the RGB, at $U \sim 17.5$, indicating that the two abundance groups are present all over the RGB, even well below the RGB bump, where no deep mixing is expected. This evidence further strengthens the idea that the bimodal Na, O, CN distribution must have been present in the material from which the stars we presently observe in M4 originated.

Figure 2.11 unequivocally shows that the Na (CN) dichotomy is associated to a dichotomy in the color of the RGB stars. In order to quantify this split, we calculated for the Na-poor group of stars the mean difference in $(U-B)$ color with respect to a fiducial line representative of the RGB Na-rich stars (see Fig. 2.13). The fiducial line has been obtained as follows:

- the CMD has been divided into bins of 0.30 mag in U, and a median color $(U-B)$ and U magnitude have been computed for the Na-rich ([Na/Fe] ≥ 0.2) stars in each bin. The median points have been fitted with a spline function which represent a first, raw fiducial line;
- for each Na-rich star, the difference in color with respect to the fiducial

was calculated, and the 68.27th percentile of the absolute values of the color differences, was taken as an estimate of the color dispersion (σ). All stars with a color distance from the fiducial larger than 3σ were rejected;

- the median colors and magnitudes and the σ of each bin were redetermined by using the remaining stars.

The leftmost panel of Fig. 2.13 shows the original CMD, while the rightmost one shows the CMD after subtracting from each Na-poor star the fiducial line color appropriate for its U magnitude. The differences are indicated as $\Delta(U-B)$. We calculated the average $\Delta(U-B)$ of Na-poor stars with $U \geq 14.8$. This cut in magnitude has been imposed by the poor statistics and the presence of the probable AGB stars at brighter magnitudes. The mean $\Delta(U-B)$ value is -0.17 ± 0.02 (dotted line in the left most panel of Fig. 2.13).

The significant difference between the mean colors of the 2 groups of stars is a further evidence of the presence of two different stellar populations in the RGB of M4, to be associated with the different content of Na, and, because of the discussed correlations to different O, N, and C content.

In order to understand the origin of the photometric dichotomy, using SPECTRUM, we simulated two synthetic spectra, one representative of the Na-rich, CN-strong stars and one for the Na-poor, CN-weak ones. The two synthetic spectra were computed using as atmospheric parameters the mean values measured for the sample of our stars for which there are literature data on the CN band strengths (see Tab. 2.5), and assuming for the C, N, O, Na abundances the average values calculated for the CN-W(+I) and the CN-S groups and listed in Tab. 2.6. We then multiplied the two spectra by the efficiency curve of our U and B photometric bands (Fig. 2.14, lower panels), and, finally, we calculated the difference between the resulting fluxes. The upper panels of Fig. 2.14 show the differences between the two simulated spectra as a function of the wavelength for the U (left panel) and B (right panel) panel. It is clear that the strength of the CN and NH bands strongly influences the $(U-B)$ color. The NH band around 3360 Å, and the CN bands around 3590 Å, 3883 Å and 4215 Å are the main contributors to the effect.

The differences in magnitude between the CN-S and the CN-W(+I) simulated spectra in the two bands are: $\Delta U_{Strong-Weak} = +0.06$ and $\Delta B_{Strong-Weak} = +0.02$. Consequently, the expected color difference between the two groups of stars is $\Delta(U-B)_{Strong-Weak} = +0.04$. This value goes in the same direction, but it is smaller than the observed one ($\Delta(U-B)_{Strong-Weak} = +0.17 \pm 0.02$). However, we note that our procedure uses simulated spectra with average abundances, and therefore should be considered a rough simulation. We cannot

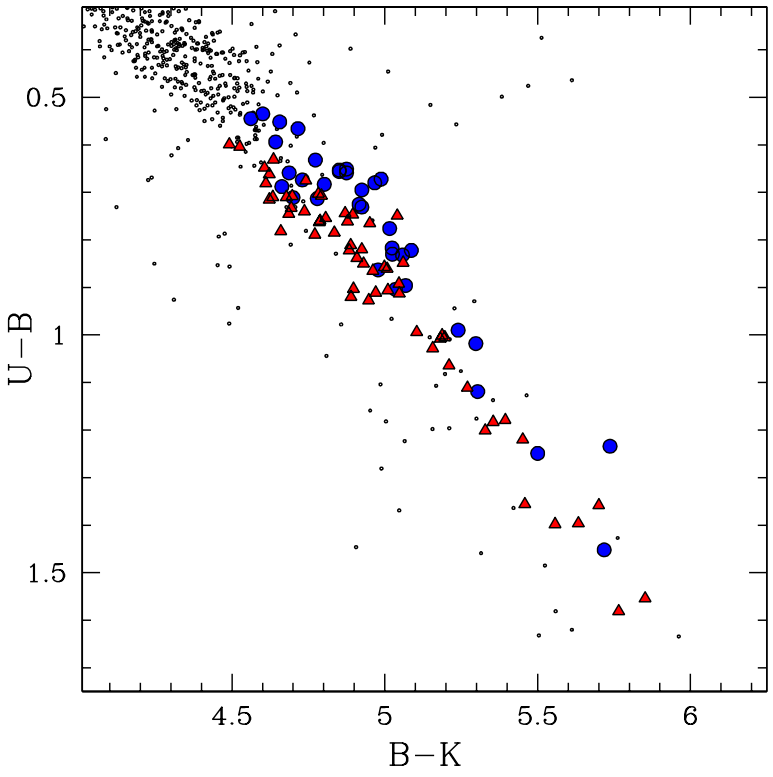

FIGURE 2.12— $(U-B)$ vs. $(B-K)$ diagram: U and B come from WFI photometry, K from 2MASS catalogue. The UVES stars belonging to the two different Na groups are represented as in Fig. 2.11.

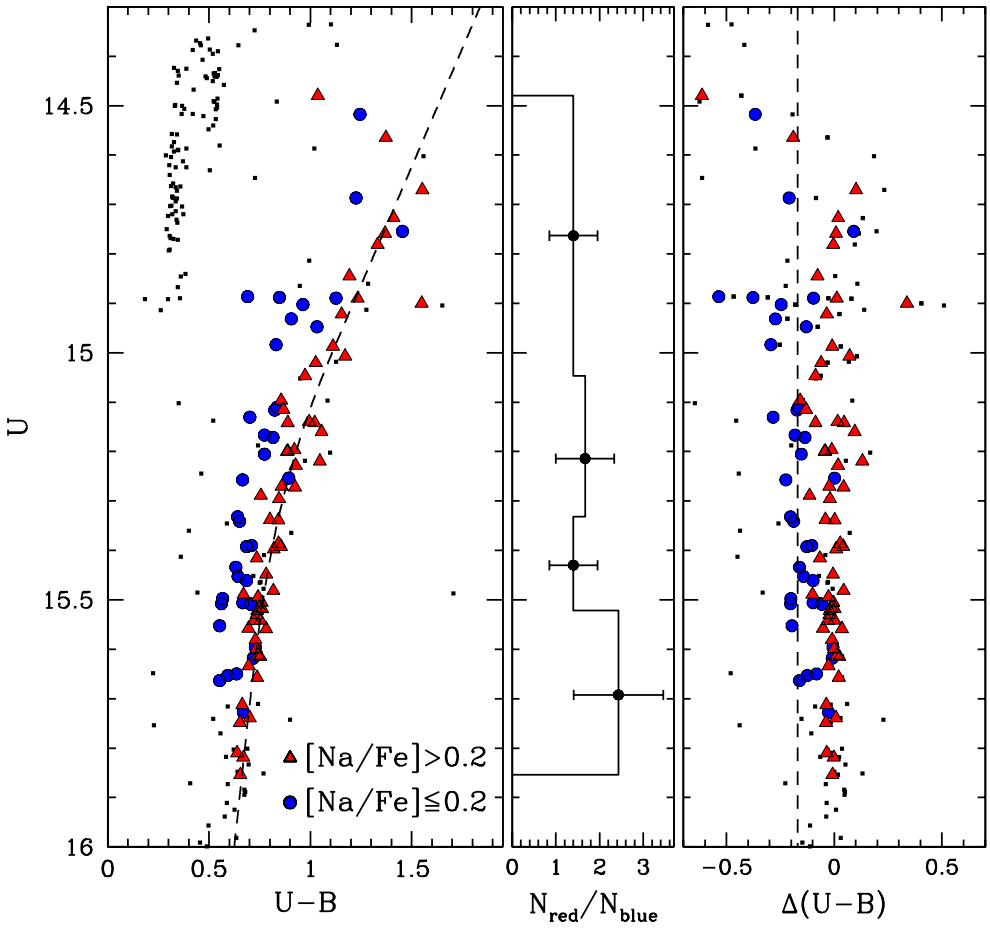

FIGURE 2.13— (Left panel) Distribution along the RGB of the stars with measured abundances. The Na-rich (red) and the Na-poor (blue) stars are represented as in Fig. 2.11 and Fig. 2.12. In the middle panel the N_{red}/N_{blue} ratios for the 4 selected magnitude bins are shown with their relative Poisson errors. The rightmost panel shows the color difference between each analyzed star and a reference fiducial line (dotted line).

exclude the possibility that other effects (perhaps related to the structure and evolution of the stars with different chemical content, or effects on the stellar atmosphere associated with the complex distribution of the chemical abundances in addition to the CN band), might further contribute to the photometric dichotomy in the RGB. Surely, our simulations show that the CN-bimodality affects the $(U-B)$ color and can be at least partly responsible for the observed spread in the U vs. $(U-B)$ CMD.

Finally, we investigated whether the chemical and photometric dichotomy is related to the evolutionary status along the RGB. To this end, we have calculated the fractions of stars in the 2 Na-groups at different magnitudes along the RGB. As shown in the middle panel of Fig. 2.13, we divided the RGB in 4 magnitude bins containing the same number of stars with measured metal content, and calculated the ratio between the number of Na-rich (N_{red}) and the number of Na-poor (N_{blue}) stars in each bin. The N_{red}/N_{blue} ratios with their associated Poisson errors as a function of the magnitude are plotted the middle panel of Fig. 2.13. The N_{red}/N_{blue} values in the different magnitude bins are the same within the errors. A similar result is obtained if we divide the RGB in two bins only, but containing a number of stars twice as large as in the previous experiment. In this case, we have $N_{red}/N_{blue} = 1.52 \pm 0.44$ for $14.0 < U < 14.9$, $N_{red}/N_{blue} = 1.82 \pm 0.54$ for $14.9 < U < 15.8$.

Figure 2.15 shows the dependence of Na, Al, and S(3839) index as a function of the magnitude U (upper panel) and B (lower panel). Again, we do not see any trend of the abundances with the position of the stars along the RGB.

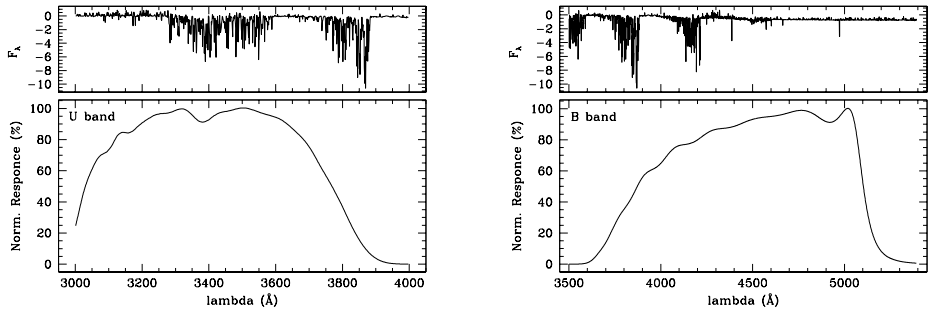

FIGURE 2.14— The differences (expressed in 10^4 erg/cm^2/sec/Angstrom) between the CN-S and the CN-W(+I) simulated spectra in the U and B band are represented in the upper panels. The normalized response of the two filters is also shown in the lower panels.

In conclusion, there is no evidence for a dependence of the Na content and (because of the discussed correlations) of the O, Al abundances or of the CN

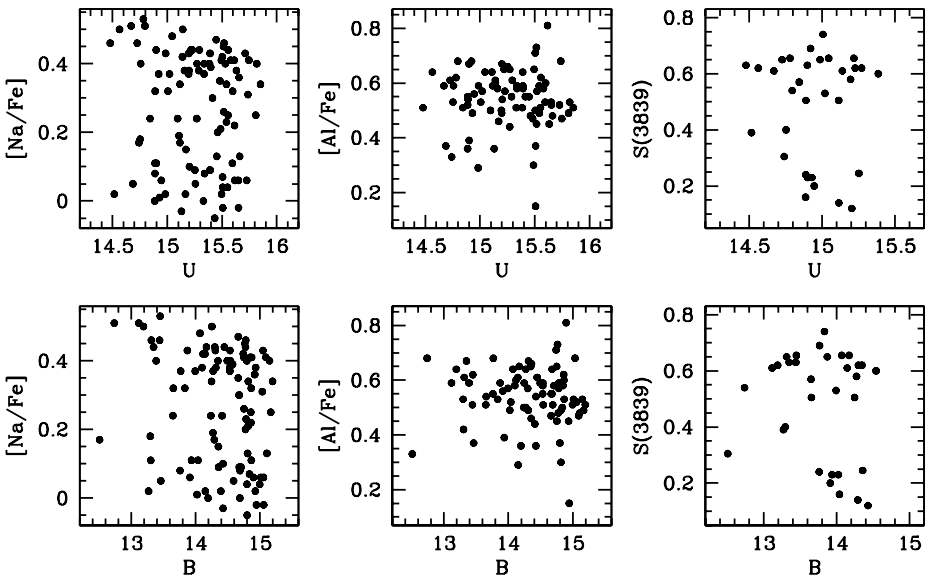

FIGURE 2.15— Dependence of Na, Al, and S(3839) index as a function of the magnitude U (upper panels) and B (lower panels).

strength with the evolutionary status of the stars.

2.6.2 The RGB progeny on the HB

In the previous sections, we have identified two groups of stars with distinct Na, O, CN content, and which populate two distinct regions in the U vs. $(U-B)$ CMD.

We note that Yong & Grundhal (2008), by studying 8 bright red giants in the GC NGC 1851 found a large star to star abundance variation in the Na, O, and Al content, and suggested that these abundance anomalies could be associated with the presence of the two stellar populations identified by Milone et al. (2008), a situation apparently very similar to what we have found in M4. Cassisi et al. (2008) suggest that extreme CNO variations could be the basis of the SGB split found in NGC 1851. As discussed in Milone et al. (2008) there is some evidence of a split of the RGB in NGC 1851 similar to what we have found in this paper for M4. We have investigated all available HST data of M4, including CMDs from very high precision photometry based on ACS/HST images; we could find no evidence for a SGB split (as in NGC 1851) or evidence for a MS split (as in NGC 2808 or ω Cen).

It is also useful to investigate where the progeny of the two RGB populations is along the HB. Milone et al. (2008) suggest that the bimodal HB of NGC 1851 can be interpreted in terms of the presence of two distinct stellar populations in this cluster, and tentatively link the bright SGB to the red HB (RHB) and the fainter SGB to the blue HB (BHB). M4 also has a bimodal HB, well populated on both the red and blue side of the RR Lyrae gap. Could the HB morphology of M4 be related to the CN bimodality? N81, studying the CN band strengths on a sample of 45 giant stars in M4, suggested the possibility of a relation between the HB morphology and the CN-bimodality.

To test the possible relation between the chemical and consequent RGB bimodality of M4 and the morphology of its HB, we used the WFI@2.2m instrumental photometry by Anderson et al. 2006 (Fig. 2.16) corrected for differential reddening, and selected the cluster members using the measured proper motions. We remark here the fact that this photometry is not the one we use in the whole paper. The homogenization between the two photometries is a difficult and long process (mainly because the fact that the B filters for the two datasets are different) beyond the scope of this work.

In our test, we used the V vs. $(B-V)$ CMD, as in this photometric plane the two components of the HB are more clearly distinguishable.

In Fig. 2.16, different symbols show the red and blue HB stars that we selected. The ratio between the number (N_{BHB}) of the HB stars bluer than the

RR-Lyrae instability strip (BHB), and the total HB stars (N_{TOT}) is:

$$N_{BHB}/N_{TOT} = 0.56 \pm 0.10$$

while the ratio between the Na rich stars (N_{NaR}) and the total number of stars in our spectroscopic sample (N_S) is:

$$N_{NaR}/N_S = 0.64 \pm 0.10$$

where the associated uncertainties are the Poisson errors. Within the statistical uncertainties, accounting for the different evolutionary times along the HB, we can tentatively associate the Na-rich stars with the BHB, and the Na-poor stars with the RHB. A direct measurement of the metal content of the HB stars is needed in order to support this suggestion..

TABLE 2.7— Mean abundance ratios and relative rms (σ) for the Na-rich and Na-poor groups. In the last column, the difference between Na-rich and Na-poor stars are listed.

[el/Fe]	Na-rich	σ	Na-poor	σ	$\Delta(Na_{rich-poor})$
[OI/Fe]	$+0.34 \pm 0.01$	0.08	$+0.47 \pm 0.01$	0.04	-0.13 ± 0.01
[NaI/Fe]	$+0.38 \pm 0.01$	0.08	$+0.07 \pm 0.01$	0.06	$+0.31 \pm 0.01$
[MgI/Fe]	$+0.48 \pm 0.01$	0.06	$+0.52 \pm 0.01$	0.05	-0.04 ± 0.01
[AlI/Fe]	$+0.57 \pm 0.01$	0.08	$+0.49 \pm 0.02$	0.13	$+0.08 \pm 0.02$
[SiI/Fe]	$+0.49 \pm 0.01$	0.04	$+0.46 \pm 0.01$	0.06	$+0.03 \pm 0.01$
[CaI/Fe]	$+0.28 \pm 0.01$	0.04	$+0.28 \pm 0.01$	0.04	$+0.00 \pm 0.01$
[TiI/Fe]	$+0.29 \pm 0.01$	0.03	$+0.29 \pm 0.01$	0.05	$+0.00 \pm 0.01$
[TiII/Fe]	$+0.35 \pm 0.01$	0.07	$+0.34 \pm 0.01$	0.05	$+0.01 \pm 0.01$
[CrI/Fe]	-0.04 ± 0.01	0.05	-0.03 ± 0.01	0.05	-0.01 ± 0.01
[FeI/H]	-1.07 ± 0.01	0.05	-1.07 ± 0.01	0.05	$+0.00 \pm 0.01$
[NiI/Fe]	$+0.02 \pm 0.01$	0.03	$+0.01 \pm 0.01$	0.03	$+0.01 \pm 0.01$
[BaII/Fe]	$+0.42 \pm 0.01$	0.07	$+0.40 \pm 0.02$	0.13	$+0.02 \pm 0.02$

2.7 Conclusions

We have presented high resolution spectroscopic analysis of 105 RGB stars in the GC M4 from UVES data.

We have found that M4 has an iron content $[Fe/H] = -1.07 \pm 0.01$ (the associated error here is the internal error only), and an α element overabundance $[\alpha/Fe] = +0.39 \pm 0.05$. Si and Mg are more overabundant than the other α elements, suggesting a primordial overabundance for these elements. Moreover,

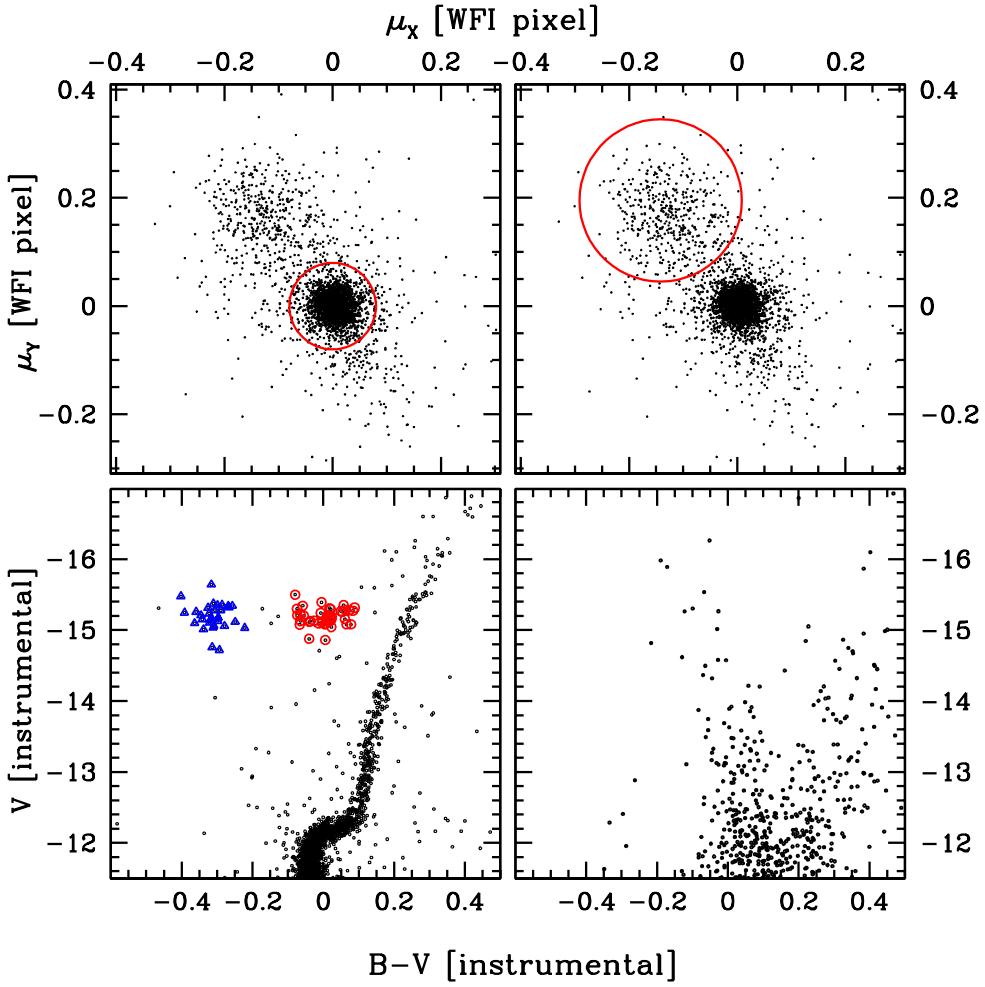

FIGURE 2.16— In the top panels, the proper motions diagrams show the separation of the probable cluster stars (left panel) from the field (right panel). In the bottom panels, the cluster and field CMD (V vs. $(B-V)$) are shown for the stars within the red circle in their respective upper panels. In the M4 CMD, the stars on the red and on the blue side of the RR Lyrae instability strip are represented with red and blue symbols respectively. For this figure, the photometry, which is not photometrically calibrated, is taken from Anderson et al. (2006).

we also find a slight overabundance of Al. The [Na/Fe] versus [O/Fe] ratios follow the well-known Na-O anticorrelation, signature of proton capture reactions at high temperature. No Mg-Al anticorrelation was found.

We find a strong dichotomy in Na abundance, and show that it must be associated to a CN bimodality. Tab. 2.7 synthesizes the spectroscopic and photometric differences we found for the two groups of stars. Comparing our results to those in the literature on the CN band strength, the CN-strong stars appear to have higher content in Na and Al, and lower O than the CN-weak ones. Apparently, M4 hosts two different stellar populations. This fact is evident from a chemical abundance distribution, and is also confirmed by photometry. In fact, an inspection of the U vs. $(U-B)$ CMD reveals a broadened RGB, and, as shown in our investigation, the two Na groups of stars occupy different positions (have different colors) along the RGB. Our sample of stars is composed of objects with U brighter than $\sim$16, but, as shown in Fig. 2.11, the RGB appears to be similarly spread from the level of the SGB to the RGB tip. Since our photometry has been corrected for differential reddening, we conclude that the observed RGB spread at fainter magnitudes must also be due to the metal content dichotomy.

We did not find any evident dependence of the chemical abundance distribution on the evolutionary status (along the RGB) of the target stars, from below the RGB bump to the RGB tip. This is an additional indication that the abundance spread must be primordial.

The two groups of stars we have identified both spectroscopically and photometrically seem to be due to the presence of two distinct populations of stars. The abundance anomalies are very likely due to primordial variations in the chemical content of the material from which M4 stars formed, and not to different evolutionary paths of the present stellar population of M4. This is somehow surprising, because of the relatively small mass of M4 – it is an order of magnitude smaller than the mass of ω Cen, NGC 2808, NGC 1851, NGC 6388, the other clusters in which a multiple stellar generation has been confirmed. Where did the gas which polluted the material for the CN-Na rich stars come from? Has it been ejected from a first generation of stars? How could it stay within the shallow gravitational potential of M4?

The idea that M4 hosts two generations of stars makes the multipopulation phenomenon in GCs even more puzzling than originally thought. It becomes harder and harder to accept the idea that the phenomenon can be totally internal to the cluster, unless this object is what remains of a much larger system (a larger GC or the nucleus of a dwarf galaxy?). Surely, Because its orbit involves frequent passages at high inclination through the Galactic disk, always at distances from the Galactic center smaller than 5 kpc (see Dinescu et al. 1999),

M4 must have been strongly affected by tidal shocks, and therefore it might have been much more massive in the past.

2.8 Multiple stellar populations in NGC6752

In a recent paper (Milone et al. 2009), we have carried out high-precision photometry on a large number of archival HST images of the Galactic globular cluster NGC 6752, to search for signs of multiple stellar populations. We find a broadened main sequence, and demonstrate that this broadening cannot be attributed either to binaries or to photometric errors. There is also some indication of a main-sequence split.

The ACS/WFC CMD of the MS is shown in Fig. 2.17. We have applied the corrections for spatial variations of the zero point of colors, as described in the paper, and have excluded stars less than 1 arcmin from the cluster center, so as to avoid the most crowded regions. (Note that this is a post-core-collapse cluster.) A visual inspection of this CMD immediately suggests that NGC 6752 has a broad MS. The Hess diagram in the inset reinforces this impression, and even suggests that the cluster could have a second (but less populated) MS, on the blue side of the main MS, in close analogy with the multiple MSs that have been observed in ω Cen and in NGC 2808. We will not pursue this question further, but hope that future observations will clarify it. No significant spread could be found along the subgiant branch, however.

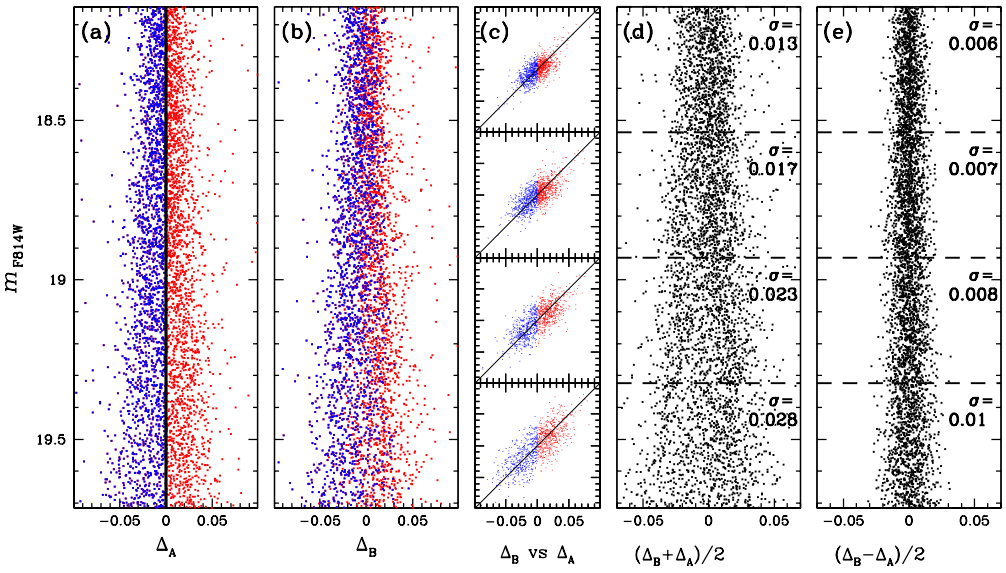

FIGURE 2.17— CMD of NGC 6752 from ACS/WFC data zoomed around the MS.

We have also used wide-field photometry to investigate the RGB. A broadened RGB is clearly visible in the U vs. U-B CMD of NGC 6752, derived from ground-based photometry by Momany et al. (2002) with ESO's Wide Field Imager, and shown in Fig.2.18. The broadening extends from the base of the RGB to the RGB tip, and looks extremely similar to the broadening of the RGB observed in M4, and associated with the presence of two stellar populations with different ratios in their [Na/Fe] and [O/Fe] abundances, and different CN band strengths. The two groups of stars studied in this chapter in M4 lie in two different regions of the RGB. One group, which consists of Na-rich, CN-strong stars, occupies a narrow sequence on the red side of the RGB, while the other group, made up of Na-poor and CN-weak stars, has a broader spread on the blue side of the RGB. The Na-O anticorrelation in NGC 6752 has been extensively studied by Gratton et al. (2001), and Carretta et al. (2005, 2007, 2009). In particular, both Gratton et al. (2001) and the 2005 Carretta et al. paper also found the Na-O anti-correlation in unevolved and barely evolved stars. Carretta et al. (2007, 2009) present an analysis of the largest sample of globular cluster RGB stars available in the literature. In Fig.2.18 we identify stars from Carretta et al. (2007) in our U vs. U-B CMD, by using the same symbols as in the inset, which shows the Na-O anticorrelation that they found. Here, following the criteria defined in Carretta et al. (2009), we isolate two subsamples: i) the primordial population, located in the Na-poor/O-rich region (marked with blue symbols), and ii) their extreme and intermediate components, which are Na-rich/O-poor. (We have lumped these two groups together as red symbols). The same two groups of stars are located in different regions of the RGB in the U vs. U-B CMD, in close analogy with the results for M4. Most of the Na-poor (primordial) stars are distributed on a bluer and broader sequence around the RGB, while the Na-rich stars tend to be distributed on a narrower sequence on the red part of the RGB. This stellar distribution continues well below the HB level. The bimodal color distribution also extends well below the RGB-bump, suggesting that it is not a consequence of the mixing of the stellar interiors. The MS of NGC 6752 is intrinsically broadened, and possibly split. Also, the Na-O anti-correlation is more extended in NGC 6752 than in M4.

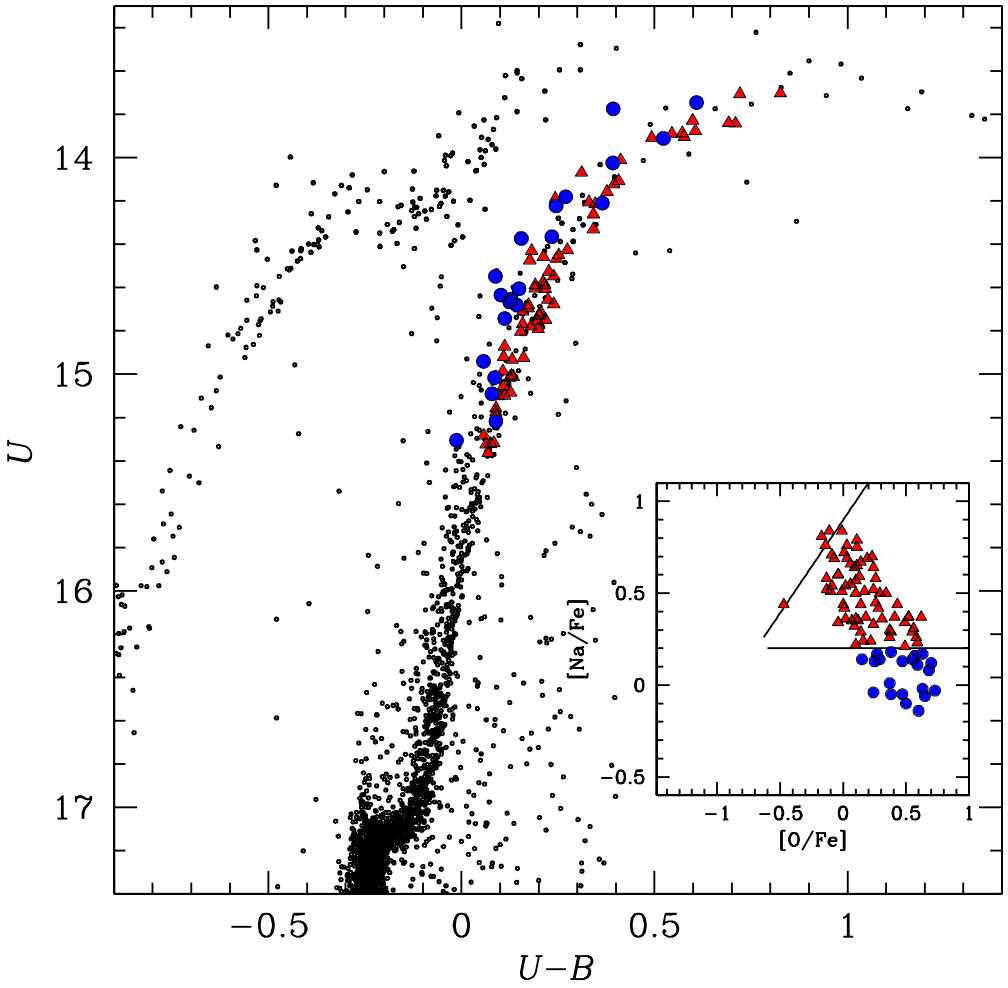

FIGURE 2.18— CMD from Wide Field Imager photometry, as obtained by Momany et al. (2002). The Na-O anti-correlation for the stars measured by Carretta et al. (2007) is shown in the inset, where the solid lines delimit the primordial, intermediate, and extreme populations, as defined in Carretta et al. The stars of the primordial population are represented by blue circles, while red triangles are the intermediate and extreme groups.

3

A double stellar generation in NGC 6656 (M 22)

At the basis of the present investigation, there is a result by our group, who identified a bimodal distribution of the stars in the SGB of the GC NGC 6656 (Piotto 2009, see also Fig. 3.18 of the present paper).

Located at a distance from the Sun of ∼3.2 kpc (Harris 1996), NGC 6656 (M 22) is a particularly interesting GC, because a large number of photometric and spectroscopic studies imply that it contains a complex metallicity spread, similar to, albeit significantly smaller than, that found in ω Centauri. In particular, it has often been suggested, although never convincingly confirmed, that M 22 may also have a spread in the abundance of iron.

The first evidence of a spread in metallicity came from the significant spread along the RGB (Hesser et al. 1977; Peterson & Cudworth 1994) observed both in $(B-V)$ and in Strömgren colors. However, it remains still uncertain whether this spread can be attributed to either a metallicity spread or reddening variations. Because of its location on the sky, close to the Galactic plane and toward the Galactic bulge $[(b,\ell) \simeq (10^\circ, 7^\circ)]$, M 22 is affected by high and spatially varying interstellar absorption, with a reddening in the interval $0.3 < E(B-V) < 0.5$. This differential reddening creates a degeneracy in measuring metallicity when the atmospheric parameters of the stars are derived from their color. Spectroscopic studies are divided between those that conclude that no significant metallicity variations is present in M 22 (Cohen 1981, based on 3 stars; Gratton 1982, 4 stars) and studies claiming a spread in iron, with $-1.4 <$ [Fe/H] < -1.9 (Pilachowski et al. 1984, 6 stars; Lehnert et al. 1991, 4 stars).

Particularly interesting are the findings about CN-band strengths. Norris & Freeman (1983) showed that CN variations in M 22 were correlated with Ca, H, and K line variations, similar to those in ω Cen. By studying a sample of 4 stars, Lehnert et al. (1991) found Ca and Fe variations that also correlated with variations in CH and CN band strength. However, Brown & Wallerstein (1992) found no Ca abundance differences between CN-strong and CN-weak stars, although they observed differences in [Fe/H] correlating with the CN-strength. Kayser et al. (2008) found some indications of a CN-CH anti-correlation in SGB stars, which was perhaps diluted by large uncertainties introduced by differential reddening.

In the present study, we analyze high resolution UVES spectra for a sample of seventeen RGB stars in M 22 to study the chemical abundances and possible relations to the identified split in the SGB. To increase the statistical significance and reinforce our findings, we also added the results from a sample of fourteen RGB stars from medium resolution, high S/N GIRAFFE spectra. In Sect. 3.1, we provide an overview of the observations and the data analysis, and in Sect. 3.2 we describe the procedure used to derive the chemical abundances. Our results about the chemical composition of M 22 are presented in Sect. 3.3, and a discussion of them is provided in Sect. 3.4. In Sect. 3.5, we look for possible connections between our spectroscopic results and the two stellar populations photometrically observed by Piotto (2009). A comparison between the results of this paper and those of Marino et al. (2008) on the GC M 4 is provided in Sect. 3.6. In Sect. 3.7, we present a brief discussion of the results obtained from GIRAFFE spectra. Sect. 3.10 summarizes the most relevant properties of the two stellar populations of M 22.

3.1 Observations and membership analysis

Our data set consists of spectra of seventeen RGB stars retrieved from the ESO archive. The observations were obtained using UVES (Dekker et al. 2000) and FLAMES@UVES (Pasquini et al. 2002). The spectra cover the wavelength range 4800-6800 Å, are of resolution $R \simeq 45\ 000$, and have a typical S/N $\sim 100 - 120$.

Data were reduced using the UVES pipeline (Ballester et al. 2000), including bias subtraction, flat-field correction, wavelength calibration, and spectral rectification. The membership of the analyzed stars was established from the radial velocities obtained using the IRAF-FXCOR task, which cross-correlates the object spectrum with a template. As template, we used a synthetic spectrum obtained from the spectral synthesis code SPECTRUM[1], using a Kurucz

[1]See http://www.phys.appstate.edu/spectrum/spectrum.html for more details.

model atmosphere with roughly the mean atmospheric parameters of our stars $T_{eff} = 4500$ K, log(g) = 1.3, $v_t = 1.6$ km/s, and [Fe/H] = −1.70. In the end, each radial velocity was corrected to the heliocentric system. We obtained a mean radial velocity of -146 ± 2 km/s from all the selected spectra, which agrees well with the values in the literature (Peterson & Cudworth 1994). To within 2σ, where σ is our measured velocity dispersion of 10 km/s, all our stars are members. The list of the analyzed stars, their coordinates, radial velocities, and magnitudes, are reported in Table3.1. Figure 1 shows the location of the target stars in the CMD of M 22.

We also analyzed a sample of stars observed with GIRAFFE HR09, HR13, and HR15 set-ups at a resolution of $R \sim 20\ 000$-$25\ 000$. These spectra were reduced by using the pipeline developed by Geneva observatory (Blecha et al. 2000). More details about these data and their analysis are provided in Sect. 3.7.

TABLE 3.1— Right ascension, declination, heliocentric radial velocity, and magnitude for the analyzed stars.

ID	RA [degree]	DEC [degree]	RV_H [km s^{-1}]	B	V	I
71	279.032271	−23.848980	−136.74	13.7458	12.3171	10.6334
88	279.150166	−23.837640	−151.21	13.9042	12.5003	10.9469
51	279.107744	−23.932690	−166.65	13.6157	12.0413	10.3165
61	279.087911	−23.945560	−145.81	13.6269	12.2122	10.5598
224	279.056427	−23.915140	−147.87	14.6701	13.4704	12.0023
221	279.137364	−23.916380	−156.45	14.6746	13.4606	11.9562
200043	279.133958	−23.934417	−152.90	13.4254	11.9082	10.1801
200025	279.042375	−23.906056	−153.22	13.2488	11.5217	9.6761
200068	279.133875	−23.858667	−139.10	13.7589	12.2961	10.6084
200031	279.113999	−23.857222	−142.08	13.1504	11.6354	9.9282
200076	279.085417	−23.940111	−158.38	13.7089	12.3647	10.7539
200101	279.159833	−23.900361	−131.00	14.0444	12.6726	11.0746
200080	279.136750	−23.852972	−147.42	13.7257	12.4310	10.8985
200104	279.083958	−23.931611	−133.25	13.9028	12.6644	11.1595
200083	279.127417	−23.880083	−129.00	–	12.4350	10.8732
200006	279.072917	−23.907249	−148.16	12.8797	11.0304	9.0975
200005	279.171042	−23.971999	−149.84	12.7874	10.9295	8.9453

3.2 Abundance analysis

Abundances of all elements, with the exception of oxygen, were measured by an equivalent width analysis by using the local thermodynamical equilibrium (LTE) program MOOG (freely distributed by C. Sneden, University of Texas at Austin). The atmospheric parameters, i.e., temperature, gravity, and microturbolence, were determined from Fe lines by removing trends in the excitation

potential (EP) and equivalent widths (EW) as a function of abundance respectively, and satisfying the ionization equilibrium.

In contrast to other elements, we measured the O content by comparing observed with synthetic spectra, because of the blending of the target O line at 6300 Å with other spectral features.

More details about the linelist, atmospheric parameters, and abundance measurements can be found in Marino et al. (2008). In Table 3.2, we report the reference chemical abundances obtained for the Sun used in this paper. The stellar parameters obtained for the M 22 stars analyzed are listed in Table 3.3.

TABLE 3.2— Measured solar abundances ($\log\epsilon(X) = \log(N_X/N_H) + 12$).

Element	abund.	# lines	Element	abund.	# lines
O	8.83	1	Ti_{TiII}	4.96	12
Na	6.31	4	V	3.89	17
Mg	7.54	3	Fe_{FeI}	7.48	145
Al	6.43	2	Fe_{FeII}	7.51	14
Si	7.61	13	Ni	6.26	47
Ca	6.39	16	Y_{YII}	2.24	8
Sc_{ScII}	3.12	12	Zr_{ZrII}	2.37	1
Ti_{TiI}	4.94	33	Ba_{BaII}	2.45	2

We note that the method employed for the measurements of the atmospheric parameters is based on the spectra, and hence our temperatures are not color dependent. This is an important advantage when analyzing GCs, such as M 22, that are affected by high differential reddening.

In Fig. 3.1, we mark with red symbols the location of our seventeen UVES target stars on the B as a function of $(B - I)$ CMD. Photometry was obtained with the Wide Field Imager (WFI) camera at the ESO/MPI 2.2 m telescope by Monaco et al. (2004) and stars with the highest photometric quality were carefully selected. Magnitudes were corrected for sky concentration (i.e. the increase in the background level in frames near the center because of light reflected back from the detector to the optics) by using the most accurate available solution (Bellini et al. 2009). Since the photometry is affected by spatially variable interstellar reddening, we corrected the CMD for this effect (by using the method described in Sarajedini et al. 2007). To separate probable asymptotic giant branch (AGB) from RGB stars, we drown by hand the black dashed line of Fig. 3.1. On the basis of their position in the CMD, stars that are possible AGB stars, are marked as triangles, while RGB stars are marked by circles.

TABLE 3.3— Atmospheric parameters for the analyzed stars.

ID	T_{eff} [K]	log(g)	v_t [km s^{-1}]	[Fe/H] [dex]
71	4460	1.15	1.44	−1.76
88	4460	1.15	1.55	−1.70
51	4260	0.90	1.60	−1.63
61	4430	1.05	1.70	−1.78
224	4700	1.70	1.45	−1.76
221	4750	1.66	1.20	−1.75
200043	4400	1.01	1.70	−1.77
200025	4100	0.67	1.80	−1.62
200068	4500	1.30	1.52	−1.84
200031	4300	0.77	1.55	−1.85
200076	4500	1.23	1.35	−1.83
200101	4500	1.35	1.55	−1.74
200080	4600	1.00	1.45	−1.81
200104	4700	1.35	1.75	−1.92
200083	4490	1.46	1.66	−1.63
200006	3990	0.20	2.08	−1.66
200005	4000	0.05	2.02	−1.94

3.2.1 Internal errors associated with chemical abundances

The primary goal of this paper is to study the intrinsic variation in chemical abundances of M 22 stars.

The differences in the measured chemical abundances between stars are a consequence of both measurement errors and intrinsic variations in their chemical composition. In this section, we attempt to differentiate between internal errors, caused by measurement uncertainties, and true variations in the chemical content of the stars. We compare the observed dispersion in the chemical abundances σ_{obs}, listed in Table 3.4, with that produced by internal errors σ_{tot}. Since we wish to study the star-to-star intrinsic abundance variations, we do not consider possible external sources of errors that do not affect relative abundances.

There are two primary sources of errors contributing to σ_{tot}: the uncertainties in the EWs, and the uncertainties in the atmospheric parameters.

To derive the typical error in the EWs, we considered two stars (#200101 and #71) with similar atmospheric parameters and roughly the same iron abundance. The dispersion in the distribution of the differences between the EWs of the iron lines for the two selected stars, that is 2.3 mÅ, was taken as our estimate

TABLE 3.4— The average abundances for M 22 stars.

El.	Abundance [dex]	σ_{obs}	N_{stars}
[O/Fe]	0.28±0.05	0.20	17
[Na/Fe]	0.24±0.08	0.30	17
[Mg/Fe]	0.39±0.03	0.11	17
[Al/Fe]	0.34±0.08	0.31	17
[Si/Fe]	0.43±0.01	0.03	17
[Ca/Fe]	0.31±0.02	0.07	17
$[Sc/Fe]_{ScII}$	0.04±0.01	0.04	17
$[Ti/Fe]_{TiI}$	0.24±0.01	0.06	17
$[Ti/Fe]_{TiII}$	0.34±0.01	0.06	17
[V/Fe]	−0.09±0.02	0.10	17
[Cr/Fe]	−0.13±0.02	0.08	17
[Fe/H]	−1.76±0.02	0.10	17
[Ni/Fe]	−0.07±0.01	0.04	17
$[Y/Fe]_{YII}$	0.05±0.07	0.27	17
$[Zr/Fe]_{ZrII}$	0.36±0.06	0.23	17
$[Ba/Fe]_{BaII}$	0.19±0.06	0.23	17

of the typical error in the EW measurement. The corresponding error in the chemical abundances was calculated by varying the EWs of a star (#200101) at intermediate temperature, representative of our sample, by adding to the EWs of all spectral lines 2.3 mÅ. The variations in the obtained abundances for each chemical species, listed in Table 3.5 (Col. 7), were taken as our most reliable estimate of the internal errors introduced by uncertainties in the EWs.

We used the same procedure described in Marino et al. (2008) to estimate the uncertainties associated with the atmospheric parameters, and the corresponding errors related to chemical abundances. From our analysis, the derived uncertainties related to atmospheric parameters are: $\Delta T_{eff}=\pm 50$ K, $\Delta\log(g)=\pm 0.14$, and $\Delta v_t=\pm 0.13$ km/s. These internal errors in the atmospheric parameters translate into the errors in chemical abundances listed in Table 3.5 (Cols. 2, 3 and 4).

We also investigated the influence of a variation in the total metallicity ([A/H]) of the model atmosphere on the derived abundances. By varying the metallicity of the model by 0.10 dex, that is the iron observed dispersion, the element abundances change by the amount listed in Col. 5 of Table 5. A variation in the metallicity of the model atmosphere changes mainly the ionization equilibrium, and hence the values of log(g), since we used the ionization equilib-

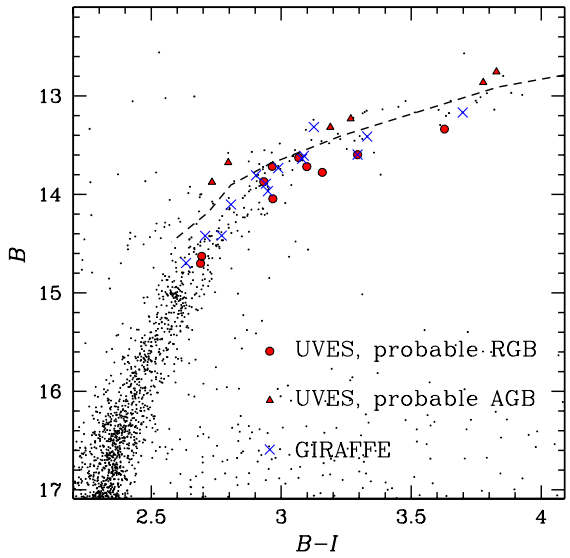

FIGURE 3.1— Distribution of the UVES target stars (red symbols) on the B vs. $(B-I)$ CMD corrected for differential reddening. Data for the star #200083 are not plotted because the B magnitude is not available for this star. The stars observed with GIRAFFE are shown by blue crosses.

rium between FeI and FeII to derive gravities. We calculated that by increasing [A/H] by 0.10 dex, log(g) decreases by ∼0.06, while temperature and microturbolence do not change significantly. Since we are interested in the search for possible small star-to-star variations in the iron abundances, we measured the effect on the [Fe/H] abundances of this change in gravity in a model atmosphere with increasing metallicity, and verified that it does not affect the derived iron abundances by more than 0.01 dex. By increasing the total metallicity by 0.2 dex, the FeII abundances change by ∼0.06 dex, and we have to decrease log(g) by ∼0.12 to re-establish the ionization equilibrium between FeI and FeII. In this case, the effect on the iron abundances is also smaller than 0.01 dex.

Column 8 of Table 5 reports the quadratic sum ($\sigma_{\rm tot}$) of the errors coming from the EW ($\sigma_{\rm EW}$) and the atmospheric parameter ($\sigma_{\rm atm}$) uncertainties. Column 9 gives the observed dispersion ($\sigma_{\rm obs}$).

Since the oxygen abundance was calculated from the same spectral line and the spectra are of similar S/N, we assume as an estimate of the error related to [O/Fe], the $\sigma_{\rm tot}$ calculated in Marino et al. (2008) for M 4 red giants. This error, for M 4 stars, was calculated to be the dispersion in O of the O-rich stars,

i.e., the Na-poor group, assumed to be homogeneous in oxygen content.

3.3 The chemical composition of M 22

3.3.1 Iron-peak and α elements

The wide spectral range of UVES data allows us to obtain chemical abundances for fifteen chemical species. Table 3.4 gives the mean abundance for each element (Col. 2), the RMS of the mean of the abundances $\sigma_{\rm obs}$ (Col. 3), and the number of stars ($N_{\rm stars}$) used to calculate the mean (Col. 4). In Table 3.4, we associate with each average abundance an uncertainty that is the RMS scatter ($\sigma_{\rm obs}$) divided by $\sqrt{N_{\rm stars}-1}$, although some of the distributions are clearly not Gaussians. A plot of our measured abundances is shown in Fig. 3.2, where, for each box, the central horizontal line is the mean value for each element, and the upper and lower lines contain the 68.27% of the distribution around the mean. The points represent individual measurements.

Our results confirm M 22 to be a metal poor GC of a mean metallicity

$$[{\rm Fe/H}]=-1.76\pm0.02 \text{ dex}, \quad \sigma_{\rm obs}=0.10$$

where $\sigma_{\rm obs}$ is the RMS of the 17 measurements. The iron-peak elements Ni, Cr, and V have abundances of [Ni/Fe]$=-0.07\pm0.01$, [Cr/Fe]$=-0.13\pm0.02$, and [V/Fe]$=-0.09\pm0.02$, respectively.

We measured the chemical abundances of five α elements: O, Mg, Si, Ca and Ti. The corresponding mean abundances are listed in Table 3.4. Here we consider only Mg, Si, Ca, and Ti. The results for oxygen will be discussed in Sect. 3.3.2. These four α elements are all overabundant with respect to solar values, with an average of

$$[\alpha/{\rm Fe}]=+0.36\pm0.04.$$

For calcium, we obtained a mean value of [Ca/Fe]$=+0.31\pm0.02$, similar to that found in other GCs. Interestingly, our stars exhibit quite a large dispersion ($\sigma_{\rm obs}=0.07$, see Table 3.4) in the Ca abundance. This spread will be discussed more in detail in Sect. 3.4.

3.3.2 NaO anticorrelation

As displayed in Fig. 3.3, sodium and oxygen exhibit the well established NaO anti-correlation found in RGB stars in all GCs for which Na and O have been measured so far (see Carretta et al. 2006). The [Na/Fe] values range from ~ -0.25 to $\sim$0.7 dex, with a dispersion $\sigma_{\rm obs}$=0.30, and [O/Fe] abundances ranging from ~ -0.10 to $\sim +0.5$ dex, with a dispersion $\sigma_{\rm obs}$=0.20.

TABLE 3.5— Sensitivity of derived UVES abundances to the atmospheric parameters and EWs. We reported the error $\sigma_{\rm atm}$ caused by the uncertainties in the atmospheric parameters ($\Delta T_{\rm eff}$, Δlog(g), $\Delta v_{\rm t}$, and Δ([A/H])), related to the error in EW measurements ($\sigma_{\rm EW}$), the squared sum of the two ($\sigma_{\rm tot}$), and the observed dispersion ($\sigma_{\rm obs}$) for each element.

	$\Delta T_{\rm eff}$ [K]	Δlog(g)	$\Delta v_{\rm t}$ [km s^{-1}]	Δ([A/H]) [dex]	$\sigma_{\rm atm}$	$\sigma_{\rm EW}$	$\sigma_{\rm tot}$	$\sigma_{\rm obs}$
	+50	+0.14	+0.13	+0.10				
[O/Fe]	–	–	–	–	–	–	0.04	0.20
[Na/Fe]	−0.02	−0.01	+0.01	−0.01	0.03	0.01	0.03	0.30
[Mg/Fe]	−0.03	+0.00	+0.01	−0.01	0.03	0.02	0.04	0.11
[Al/Fe]	−0.03	−0.01	+0.02	−0.01	0.04	0.06	0.07	0.31
[Si/Fe]	−0.05	+0.01	+0.01	+0.01	0.05	0.01	0.05	0.03
[Ca/Fe]	−0.01	−0.01	−0.01	−0.01	0.02	0.01	0.02	0.07
[Sc/Fe]	+0.03	+0.00	+0.00	+0.00	0.03	0.03	0.04	0.04
$[Ti/Fe]_{TiI}$	+0.04	−0.01	+0.00	−0.02	0.05	0.01	0.05	0.06
$[Ti/Fe]_{TiII}$	+0.02	−0.01	−0.02	−0.01	0.03	0.02	0.04	0.06
[V/Fe]	+0.03	+0.00	+0.03	−0.01	0.04	0.01	0.04	0.10
[Cr/Fe]	+0.02	−0.03	−0.01	−0.02	0.04	0.01	0.04	0.08
$[Fe/H]_{FeI}$	+0.07	+0.00	−0.02	−0.01	0.07	0.06	0.09	0.10
$[Fe/H]_{FeII}$	−0.02	+0.05	−0.02	+0.02	0.06	0.06	0.08	0.10
[Ni/Fe]	−0.01	+0.00	+0.01	+0.00	0.01	0.01	0.01	0.04
[Y/Fe]	+0.03	−0.01	−0.02	+0.00	0.04	0.01	0.04	0.27
[Zr/Fe]	+0.03	+0.00	+0.02	+0.00	0.04	0.01	0.04	0.23
[Ba/Fe]	+0.05	−0.01	−0.09	+0.00	0.10	0.03	0.10	0.23

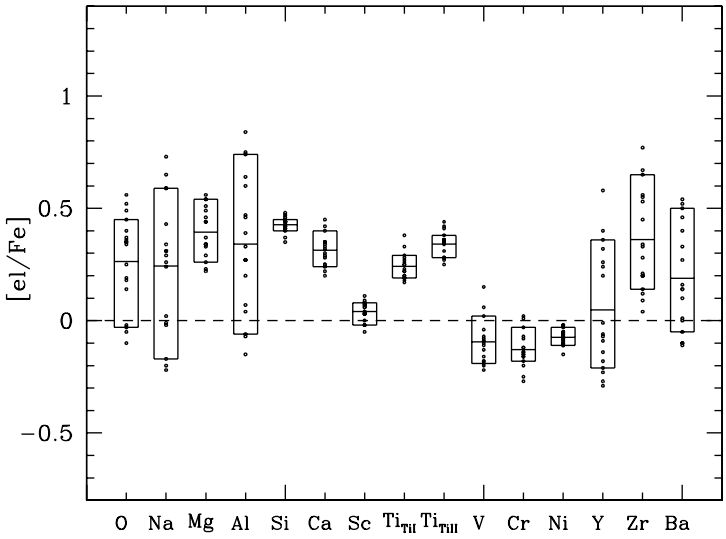

FIGURE 3.2— Box plot for M 22 star element abundances. The points are the individual measurements. The central horizontal line of each box is the mean of the data; the upper and lower lines represent the 68.27% levels of the distribution around the mean value.

As discussed in Sect.3.5, Piotto (2009) demonstrated that the SGB of M 22 is split into two separate branches, indicating the presence of two stellar populations. In Fig. 3.4, we compare the Na versus O trend for M 22 with those observed in other four GCs where multiple stellar populations have been identified: NGC 2808 (data from Carretta et al. 2006), NGC 1851 (data from Yong & Grundahl 2008), NGC 6388 (data from Carretta et al. 2007), and M 4 (data from Marino et al. 2008).

In NGC 2808, the presence of multiple stellar populations is inferred by the triple MS (Piotto et al. 2007). The three MS branches may be associated with the complexities of the cluster horizontal branch (D'Antona & Caloi 2004) and its oxygen abundance distribution (Carretta et al. 2006). In contrast, the MS of M 22 is narrow and any spread or split, must be smaller than 0.02 magnitudes in $m_{\rm F435W} - m_{\rm F814W}$ color (see Piotto 2009). Figure 3.4 shows that NGC 2808 stars cover almost the same range of Na abundances as M 22, but span a range of O abundance at least two times larger.

In M 4, the presence of multiple populations is inferred by the bimodal distribution of the Na abundance (Marino et al. 2008). In addition, stars from the two groups of different Na content populate two distinct RGB sequences in the U vs. $U-B$ CMD. Moreover, no split in either the MS or SGB has been identified. Interestingly, in M 4, the maximum variations in [Na/Fe] and [O/Fe] are 0.39 and 0.31 dex respectively smaller than those observed in M 22. In particular, a few O-poor stars with [O/Fe]$\leq$0.00 and [Na/Fe]$\geq$0.50 are present among M 22 stars but not in M 4.

As in M 22, in NGC 1851 (Milone et al. 2008) and NGC 6388 (Piotto 2008; Moretti et al. 2008; Piotto 2009) the presence of multiple populations is inferred from a split in the SGB. Unfortunately, for both of these clusters, the available chemical measurements from high resolution spectroscopy are limited to seven RGB stars for NGC 6388 (Carretta et al. 2007) and eight RGB stars for NGC 1851 (Yong & Grundahl 2008). In the case of NGC 6388, the stars are located in a portion of the NaO plane that is not populated by any M 22 star in our sample, since the stars in NGC 6388 are systematically O-poorer. In contrast, the range of NaO anticorrelation in NGC 1851 matches quite well that of M 22.

At variance with the case of M 4 and NGC 2808, both NGC 1851 and M 22 seem to show a continuum distribution in [Na/Fe], without any hint of multimodalities; this is in spite of the small number of stars studied in this paper and in Yong & Grundahl (2008) for NGC 1851, preventing us from definitively excluding the presence of discontinuities in the [Na/Fe] or [O/Fe] distribution.

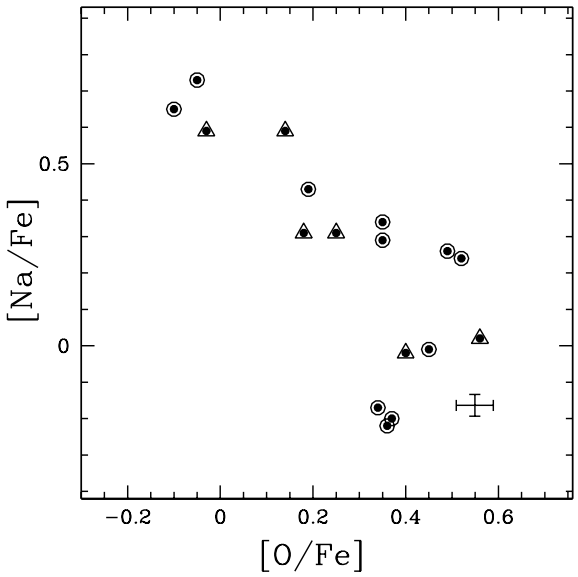

FIGURE 3.3— The anticorrelation between [Na/Fe] and [O/Fe] abundance ratios. Triangles indicate stars that, on the basis of their position on the CMD, should be AGB.

3.3.3 Aluminum and magnesium

The abundances of aluminum and magnesium were determined from Al lines at 6696 Å, and 6698 Å, from the Mg doublet at 6318-6319 Å, and the Mg line at 5711 Å.

Figure 3.5 shows the [Mg/Fe] ratio as a function of [Al/Fe]. There is no clear MgAl correlation, despite the presence of a clearly defined NaO anticorrelation, and a clear AlNa correlation, as shown in Fig. 3.6. Assuming that the Na enhancement is caused by proton capture process at the expense of Ne, we also expect to observe a MgAl anticorrelation, since Al forms at the expense of Mg. This means that we expect a decrease in Mg abundance with increasing Al content. We do not observe this effect but, given our uncertainties, it could be too small to be detected. The lack of this correlation was also found for M 4 by Marino et al. (2008). However, they found a small difference in Mg content among stars with a large range of Na abundances, according to the scenario proposed by Ivans et al. (1999), who predicted that a decrease of only 0.05 dex in Mg is required to explain the increase in abundance of Al (see their Sect. 4.2.2).

However, as we will discuss in the Sect. 3.4, the Mg variations in M22

probably reflect a more complicated nucleosynthesis, like enrichment from Supernovae.

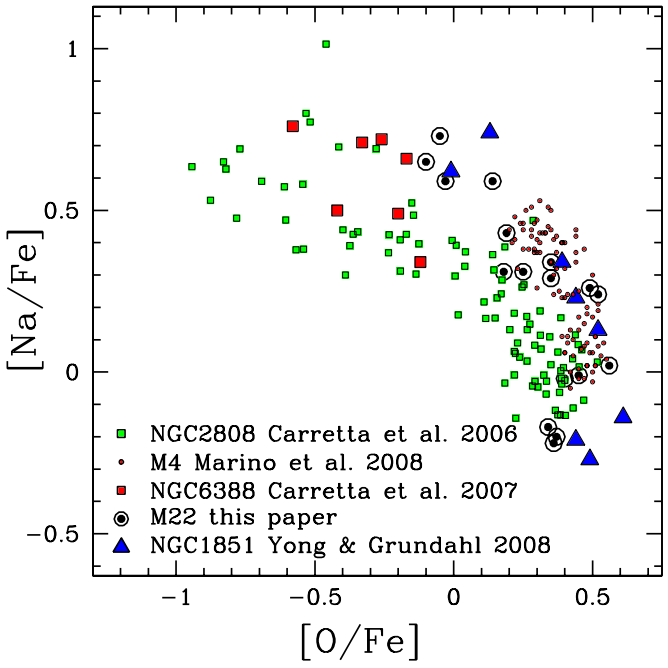

FIGURE 3.4— NaO anticorrelation for M 22 stars superimposed on a collection of stars of four GCs that host multiple stellar populations.

3.3.4 *s*-process elements

Barium, yttrium, and zirconium can be considered as a signature of the *s* processes that occur in intermediate mass AGB stars (Busso et al. 2001).

We measured abundance for three *s*-process elements: yttrium, zirconium, and barium, all of which span a wide range of abundance values. The maximum variations in [Y/Fe], [Zr/Fe], and [Ba/Fe] are of amplitudes 0.87, 0.73, and 0.65 dex, respectively, despite the small estimated internal error ($\sigma_{\rm tot} \leq 0.1$, see Table 3.5).

In Fig. 3.7, we show [Zr/Fe] and [Ba/Fe] as a function of [Y/Fe] (left and central panels), and [Ba/Fe] as a function of [Zr/Fe] (right panel). A clear correlation between each pair of *s*-process elements is evident, and the slopes of the best fitting lines are also similar.

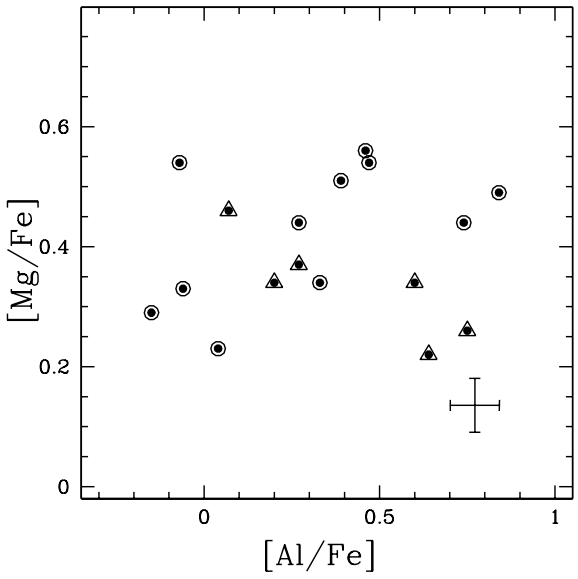

FIGURE 3.5— [Mg/Fe] as a function of [Al/Fe] abundance ratios. Symbols are as in Fig. 3.3.

Most importantly, the *s* elements clearly show a bimodal distribution: one group is overabundant in *s*-elements with average values of [Y/Fe]=+0.34±0.05, [Zr/Fe]=+0.60±0.04, and [Ba/Fe]=+0.43±0.04. This group contains seven out of seventeen stars (i.e., ∼40% of the entire sample studied in this paper). The remaining ten stars have [Y/Fe]=−0.16±0.03, [Zr/Fe]=+0.20±0.03, and [Ba/Fe]=+0.02±0.04.

Figure 3.7 suggests that we can isolate a *s*-process element rich group, and a *s*-process element poor one, by selecting stars with [Y/Fe] greater and smaller than 0, respectively. Stars rich in *s*-process elements are represented by red filled symbols, while *s* poor stars by the black empty ones. In Table 3.6, we list the mean abundances of all the elements studied in this paper, calculated separately for each of these two groups.

As an example, in Fig. 3.8 we show the [Y/Fe] ratio as a function of the [Na/Fe], [Al/Fe] and [O/Fe] ratios. There is no one-to-one correlation between Y, as well as Ba, and Zr abundances and Na, O or Al. However, we note that stars enriched in *s*-process elements are all Na-rich and Al-rich, while the group of stars with lower *s*-process element abundances spans almost all the values of Na and Al.

The bimodality in *s*-process elements in M 22 resembles the case of NGC 1851.

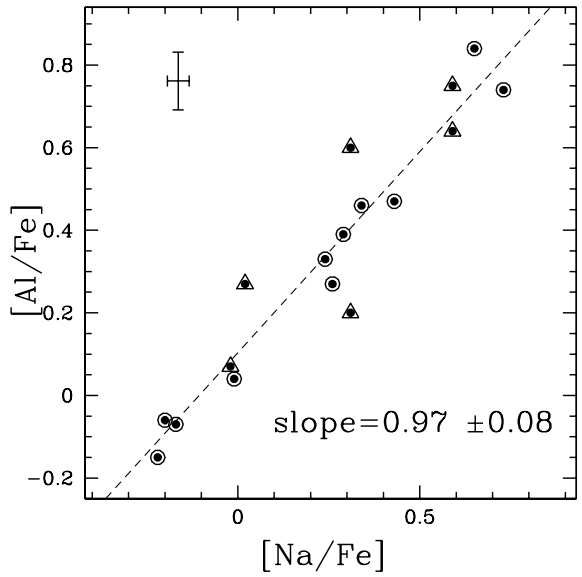

FIGURE 3.6— [Al/Fe] as a function of [Na/Fe] abundance ratios. Symbols are as in Fig. 3.3, dashed line is the best least squares fitting straight line.

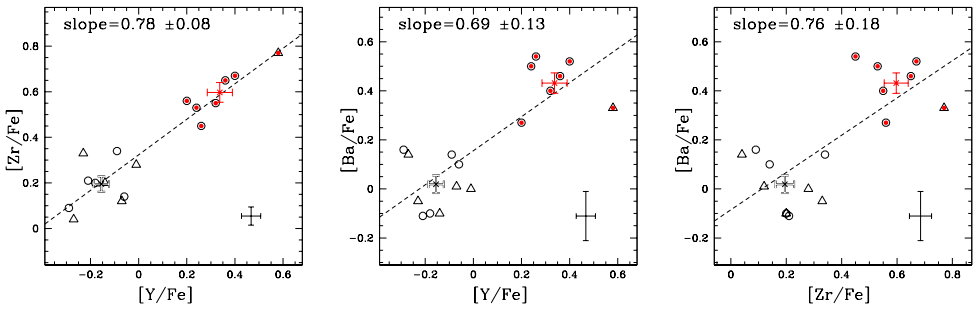

FIGURE 3.7— From left to right: [Zr/Fe] and [Ba/Fe] versus [Y/Fe] and [Ba/Fe] versus [Zr/Fe] abundance ratios. Red filled symbols represent the *s* element rich stars, and the black empty ones represent the *s* poor stars. The red and the black crosses with error bars indicate the average abundances of stars in each group, dashed lines are the best least squares fitting straight lines. Triangles indicate probable AGB stars.

In NGC 1851, Yong & Grundahl (2008) noted that the abundances of the *s*-process elements Zr and La appear to cluster around two distinct values. They suggested that the two corresponding groups of stars should be related to the two stellar populations photometrically observed by Milone et al. (2008) along

TABLE 3.6— Average abundances of *s*-element process poor and rich stars.

Element	*s*-process elements poor	*s*-process elements rich
[O/Fe]	0.30±0.06	0.26±0.10
[Na/Fe]	0.13±0.11	0.40±0.08
[Mg/Fe]	0.36±0.04	0.45±0.03
[Al/Fe]	0.26±0.11	0.46±0.10
[Si/Fe]	0.42±0.01	0.44±0.01
[Ca/Fe]	0.27±0.01	0.38±0.02
[Sc/Fe]	0.04±0.02	0.04±0.02
$[Ti/Fe]_{TiI}$	0.22±0.01	0.27±0.03
$[Ti/Fe]_{TiII}$	0.33±0.02	0.36±0.03
[V/Fe]	−0.10±0.04	−0.09±0.03
[Cr/Fe]	−0.16±0.02	−0.09±0.04
[Fe/H]	−1.82±0.02	−1.68±0.02
[Ni/Fe]	−0.09±0.01	−0.06±0.01
[Y/Fe]	−0.16±0.03	0.34±0.05
[Zr/Fe]	0.20±0.03	0.60±0.04
[Ba/Fe]	0.02±0.04	0.43±0.04

the SGB. In NGC 1851, the *s*-element abundance also appears to correlate with the Na, Al, and O abundance.

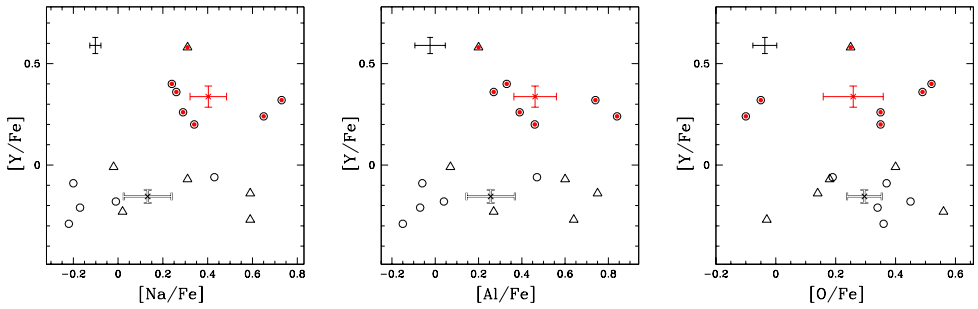

FIGURE 3.8— From the left to the right: [Y/Fe] as a function of [Na/Fe], [Al/Fe] and [O/Fe] abundance ratios. Symbols are as in Fig. 3.7.

Because of the similarity between our results and those of Yong & Grundahl (2008) for NGC 1851, it is tempting to associate the presence of the two groups of stars with different *s*-process element contents, with the two populations of stars isolated along the SGB of M 22 by Piotto (2009, see also Fig.3.18).

The *s*-element rich stars may also to be appear rich in Na and Al because of the pollution from intermediate mass AGB stars, although the lack of a clear correlation is more difficult to interpret.

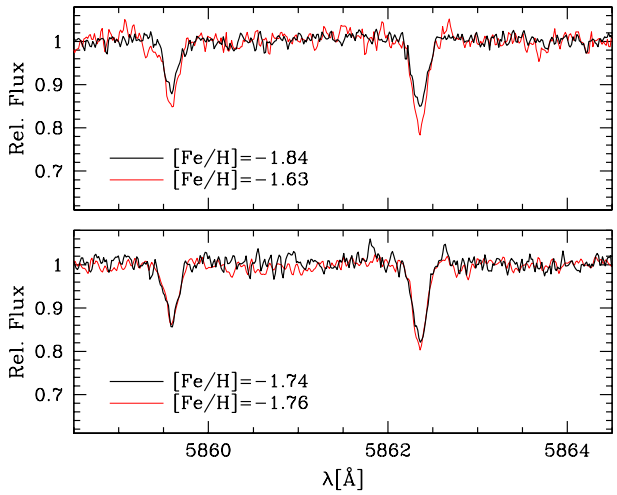

FIGURE 3.9— The upper panel shows the spectra of the metal-poor star #200068 ([Fe/H]=−1.84) and of the metal-rich star #200083 ([Fe/H]=−1.63) centered on the lines of FeI. The stellar parameters are very similar, although, the Fe lines differ significantly. The bottom panel shows the same lines for stars #200101 and #71 with similar metallicity and stellar parameters.

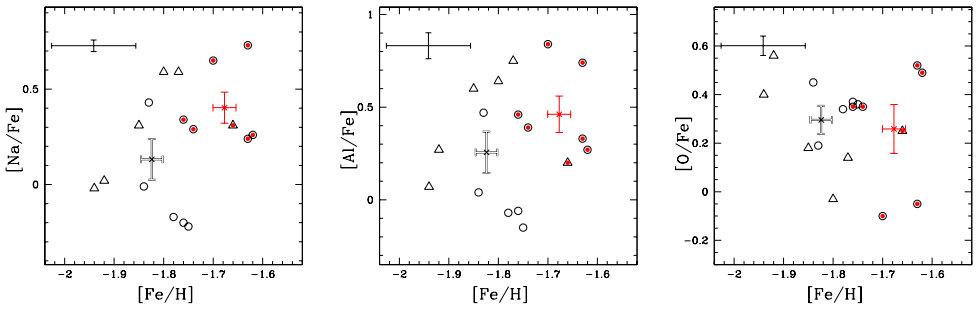

FIGURE 3.10— From the left to the right: [Na/Fe], [Al/Fe], and [O/Fe] as a function of [Fe/H] abundance ratios. Symbols are as in Fig. 3.7

We note that the results of Piotto et al. (2005) about the metal content of the stars in the two main MSs of ω Centauri can be interpreted within this scenario. Piotto et al. (2005) measured [Ba/Fe]∼0.5 for the metal-poorer ([Fe/H]=−1.68) red MS, and [Ba/Fe]∼0.8 for the metal-richer ([Fe/H]=−1.37)

bluer MS. This result was confirmed by Villanova et al. (2007), who observed that SGB metal-poor stars have a Ba content lower than intermediate-metallicity ones by about 0.2 dex. The relationship between the *s*-process element abundance and the iron content of M 22 is the subject of the following section.

3.4 The spread in Fe of M 22

For a long time, the existence of an intrinsic Fe spread in M 22 has been debated in the literature (see Ivans et al. 2004 for a review), since photometric and spectroscopic studies have yielded conflicting results. Some spectroscopic studies have found no significant variations (Gratton 1982, Ivans et al. 2004), whereas others seem to find a variation in [Fe/H] of up to ∼0.5 dex (Pilachowski et al. 1984). Photometric studies have derived similarly controversial results. Undoubtedly, the RGB of M 22 has a large spread in color. This spread is observed both in *BVI* and Strömgren photometry, but can be interpreted in terms of either metallicity variation or differential reddening, or a combination of both.

We emphasize that the [Fe/H] measurements presented in this paper are not based on photometric data, and therefore do not suffer the effects of differential reddening. For this reason, they represent an appropriate tool to measure the [Fe/H] variations in M 22.

From Table 3.5, we see that the observed dispersion $\sigma_{\rm obs}$ in iron is comparable with the estimated internal error $\sigma_{\rm tot}$, i.e., the observed star-to-star metallicity scatter could be interpreted as being caused by measurement errors only. This demonstrates the difficulty in establishing the statistical significance of any intrinsic spread in [Fe/H]. In this paper, we can tackle the problem of the iron dispersion in M 22 in a different way. The observed dispersion in iron content alone could be a poor indicator of any intrinsic metallicity dispersion. First of all, because of the abundance measurement errors. In addition, we note that if anomalies in [Fe/H] affect only a small fraction of M 22 stars, their effect on the iron dispersion of the entire sample of stars could be negligible.

A visual inspection of some spectra reinforces the suggestion that there may be star-to-star iron variations. As an example, in Fig. 3.9, we show spectra of two pairs of stars with very similar stellar atmospheric parameters. The two spectral lines in Fig. 3.9 are iron lines. The upper panel shows the spectra of the stars #200068 and #200083 for which we measured an iron abundance [Fe/H]=−1.84 and [Fe/H]=−1.63, respectively (see Table 3.3). The line depths differ significantly and, because of the similarity in their atmospheric parameter, must be indicative of an intrinsic iron difference. For comparison, in the bottom panel we plot the same spectral region for two stars (#200101 and #71) of

almost the same iron content.

Our results for the iron dispersion are not conclusive in themselves. However, it is instructive to look for possible correlations between [Fe/H] and the other chemical abundances (mainly the ones showing a spread or bimodal distribution, such as the *s*-process elements).

Figure 3.10 shows that the Fe abundance is not significantly correlated with the Al, Na, and O abundances, elements that, on the other hand, exhibit clearly defined correlations, as discussed in Sect. 3.3.2.

However, when we compare the iron abundances with the *s*-process element abundances, we find a strong correlation, with *s*-process element rich stars having systematically higher [Fe/H], as shown in the three panels of Fig. 3.11. The two *s* element rich and poor groups have average $[Fe/H]_{s-rich}=-1.68\pm0.02$ and $[Fe/H]_{s-poor}=-1.82\pm0.02$, respectively ($\delta$ [Fe/H]=0.14±0.03).

We emphasize that the significance of the Fe variation can be appreciated only when we consider the average iron content of the two groups characterized by a different *s*-element content. This is demonstrated by a simple test that we computed whose results are summarized in Fig. 3.12. We simulated 100,000 stars with an iron content, and iron abundance dispersion identical to that of observed stars, i.e., 41% of the sample are *s*-process element rich stars (red Gaussian) and a 59% are *s*-process element poor ones (blue Gaussian) with a mean [Fe/H] of −1.82 and −1.68 dex, respectively. The dispersion in iron content of each group was taken to be equal to 0.09 dex, that is the error that we estimated for the iron abundance (see Table 5). The resulting metallicity abundance dispersion for the entire sample is 0.11 dex, which is close to, and only marginally greater, than the dispersion expected from the measurement errors.

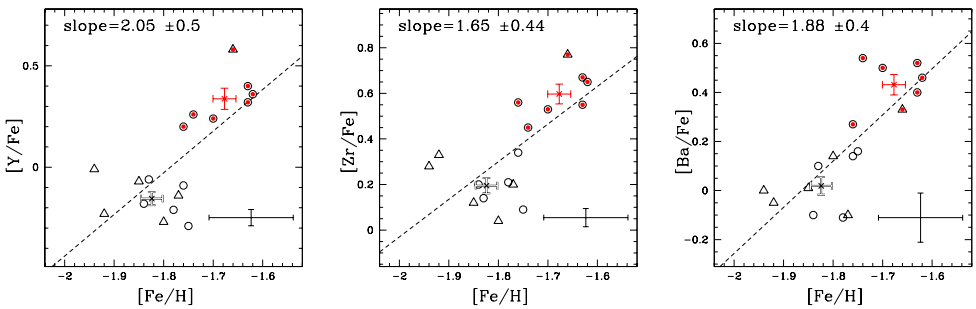

FIGURE 3.11— [Y/Fe] (*left*), [Zr/Fe] (*center*), and [Ba/Fe] (*right*) as a function of [Fe/H]. Symbols are as in Fig. 3.7, dashed lines are the best least squares fitting straight lines.

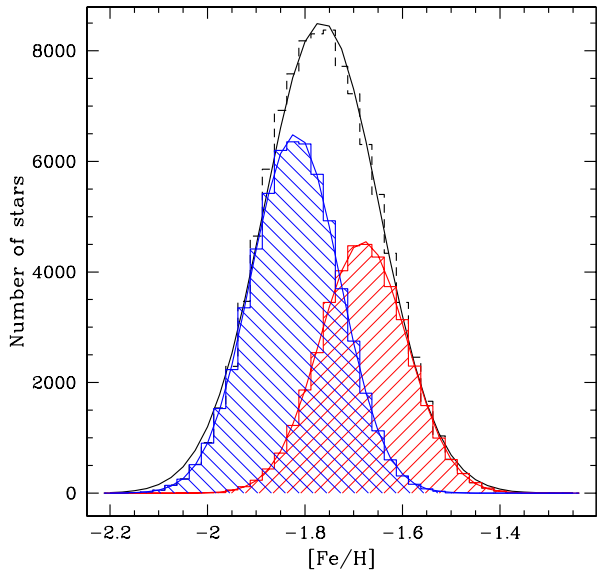

FIGURE 3.12— Simulation of 100000 stars with the properties of the two observed groups of stars. The red and the blue histograms represent the *s*-rich and the *s*-poor groups of stars, respectively.

The presence of two groups of stars, one of which is enriched in both *s*-process elements and iron, is analogous to the case of ω Centauri discussed in Sect. 3.3.4, where Piotto et al. (2005) and Villanova et al. (2007) found that the more metal rich, He-enriched stars also have a higher Ba content.

As shown in Fig. 3.13, the iron abundances are also well correlated with calcium abundances, and the Ca content correlates with the *s*-process element abundance. A similar behavior is again present in ω Centauri, where a spread in Ca was first detected by Freeman & Rodgers (1975). Villanova et al. (2007) showed that the SGB population with [Fe/H]~ -1.2 has a mean [Ca/Fe] that is higher by ~ 0.1 dex, than that found for the more metal-poor population. However, the α abundance of the most metal-rich population in ω Centauri is still debated, since Pancino et al. (2002) found the metal-rich stars to be α-poor.

In M 22, evidence of a calcium spread was noted by Norris & Freeman (1983), who showed a correlation between CN variations and Ca, similar to those in ω Centauri. By studying a sample of 4 stars, Lehnert et al. (1991), found both Ca and Fe variations that were correlated with CN-band strengths.

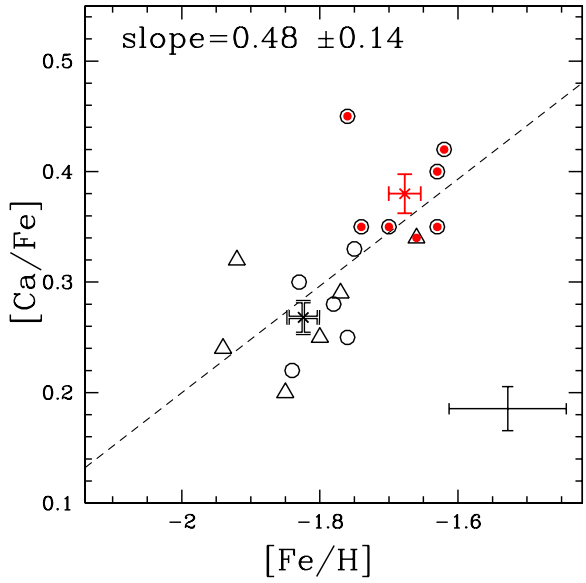

FIGURE 3.13— [Ca/Fe] as a function [Fe/H]. Symbols are as in Fig. 3.7.

Our abundance measurements indicate that both calcium and iron correlate with the *s*-process elements (Fig. 3.14 and Fig. 3.11). As shown in Fig. 3.15, we also found that calcium, like iron, is not clearly correlated with Na, although the stars with an higher Ca content seem to be slightly Na rich.

Figure 3.16 shows [Mg/Fe] and [Si/Fe] as a function of [Fe/H]. Both Mg and Si are slightly overabundant in *s*-process element rich stars with respect to *s*-process element poor ones (see also Table 3.6). This seems to suggest that core-collapse SNe (CCSNe) are the most probable candidates to produce the iron excess of the second generation of stars. If iron was produced instead by Type Ia SNe, we would expect lower [Mg/Fe] and [Si/Fe] ratios for the group of stars enriched in *s*-process elements than the first generation of (*s*-process element poor) stars. SNe Ia events are selectively enriched in iron (although a modest quantity of Si is also produced). In contrast, CCSNe in addition to iron, also produce Mg and Si in higher quantities than SNe Ia.

With a present day mass of $\sim 5{\times}10^5$ $M_\odot$, (Pryor & Meylan 1993) NGC 6656 is one of the most massive GCs in the Milky Way. Its *s*-element rich population of mass $\sim 2 \times 10^5$ $M_\odot$ and iron abundance [Fe/H]$=-1.68 \pm 0.02$ dex, includes $\sim$1.5 $M_\odot$ of fresh iron if we assume that $Z_\odot^{Fe}= 0.0013$. Each CCSN on average produces $\sim$0.07 $M_\odot$ of iron (Hamuy 2003), therefore about twenty SNe are

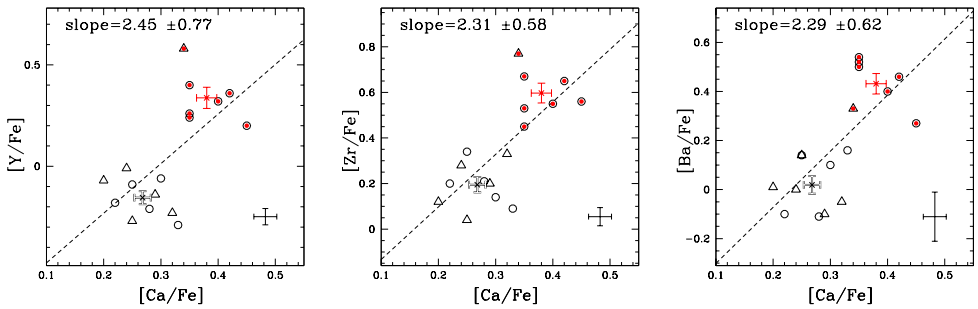

FIGURE 3.14— [Y/Fe] (*left*), [Zr/Fe] (*center*), and [Ba/Fe] (*right*) as a function of [Ca/Fe]. Symbols are as in Fig. 3.7, dashed lines are the best least squares fitting straight lines.

needed to produce the fresh iron in the second stellar population. In this scenario, the fainter SGB (and TO) of this second generation of stars is caused by their different chemical mixture, rather than an age difference.

In Fig. 3.7, Fig.3.8, Fig. 3.10, Fig. 3.11, Fig.3.13, and Fig 3.14, six out of seven probable AGB stars, represented by triangles, belong to the *s*-poor group. We emphasize that our selection of the probable AGB stars is based only on a visual inspection of the stars on the CMD, without consideration of the photometric errors. In any case, assuming that all these stars are indeed true AGB members, our *s*-poor sample would include both RGB and AGB stars. If there is really a group of AGB stars in our *s*-poor sample, they could represent the evolved low mass stars of the primordial population, which did not experience the third dredge-up and enrich their surfaces with *s*-process elements. Hence they should trace the primordial composition of the cluster. Because of their higher iron abundance, stars with higher *s* element abundances may have systematically redder colors than *s*-process element poor stars and have a low probability of being shifted by photometric errors into the AGB region.

3.5 Can the iron abundance spread account for the SGB split?

Figure 3.18 from Piotto (2009) shows that the SGB of M 22 splits into two branches. In the previous section, we have shown that there are two groups of stars in M 22 with both different *s*-process element abundances, and two different average iron contents. In this section, we investigate whether the variation in iron content can explain the split of the SGB.

In Fig. 3.19, we compare two isochrones from Pietrinferni et al. (2004) in the ACS/WFC plane $m_{\rm F606W}$ vs. $m_{\rm F606W} - m_{\rm F814W}$ of Fig. 3.18. Both of them have

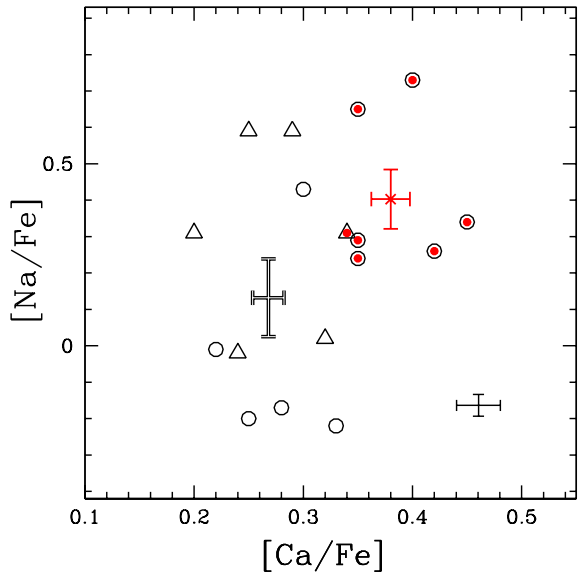

FIGURE 3.15— [Na/Fe] as a function of [Ca/Fe]. Symbols are as in Fig. 3.7.

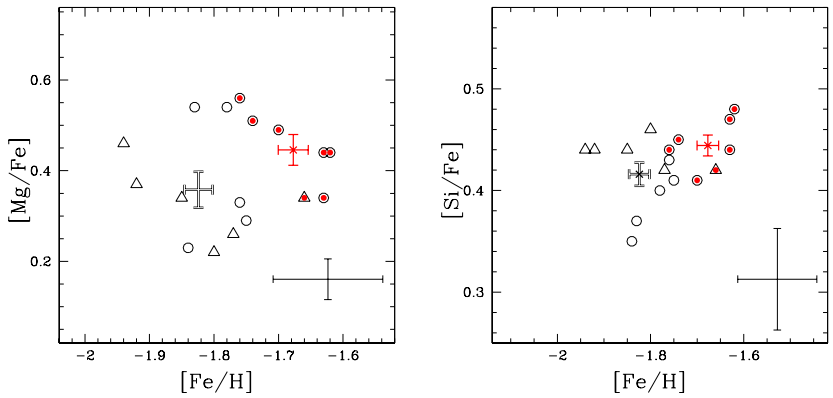

FIGURE 3.16— [Mg/Fe] (*left*), and [Si/Fe] (*right*) as a function of [Fe/H]. Symbols are as in Fig. 3.7.

an age of 14 Gyr, but different metallicities. The black line corresponds to the mean metallicity of the group of *s*-process element poor stars ([Fe/H]=−1.82) and the dashed red line is an isochrone with the average [Fe/H]=−1.68 of the *s*-process element rich stars. The different metallicity reflects mainly in a split

in both the RGB and the SGB. In the inset, we show a zoom of the SGB region. At $m_{\rm F606W} - m_{\rm F814W} = 0.85$, the difference in magnitude $m_{\rm F606W}$ between the two isochrones is $\delta m_{\rm F606W} = 0.10$, about 0.07 magnitudes smaller than that observed by Piotto (2009). We conclude that the observed difference in [Fe/H] can contribute to produce the split of the SGB observed by Piotto (2009), but that it is not sufficient. On the other hand, the entire shape of the turn off-SGB-RGB region is difficult to reproduce with standard, alpha-enhanced isochrones. This probably indicates that the reason for the SGB split may be far more complicated and also involve the NaCNO abundances, as suggested by Cassisi et al. (2008) for the case of NGC 1851.

3.6 Comparison with M 4

We compare the chemical abundances obtained in this paper for M 22 with the abundance measurements of M 4 RGB stars derived by Marino et al. (2008) to highlight the complexity of the multiple populations in different clusters.

This comparison is instructive, first of all, because M 4, in a similar way to M 22, is affected by high differential reddening (Lyons et al. 1995, Ivans et al. 1999), and moreover, their spectra were analyzed employing the same procedure. We also note that the UVES spectra of M 4 were collected with the same set-up and have almost the same S/N ratio as the M 22 spectra analyzed in this work.

Marino et al. (2008) demonstrated that M 4 hosts two distinct stellar populations, characterized by different Na contents, and different CN-band strengths. These two groups of stars also define two sequences along the RGB, although there is no split detected in the SGB. In contrast to M 22, M 4 does not show any evidence of an intrinsic Fe spread. Marino et al. (2008) set an upper limit to the [Fe/H] spread of 0.05 dex (1σ) in M 4. In the case of M 22, as discussed in Sect. 3.3.2, we identified a clearly NaO anticorrelation, but found no evidence of a dichotomy in Na distribution similar to that found in M 4. We found a dichotomy instead, in the *s*-process elements and that the SGB is split into two branches.

For comparison purposes, we show in Fig.3.17 the Fe abundances as a function of Ba and Ca in M 4, using the same scale used for the same plots as our M 22 targets (Fig. 3.11, right panel, and Fig. 3.13 respectively). In the case of M 4, there is no evidence of a chemical spread in [Ba/Fe] versus [Fe/H] nor in [Ca/Fe] versus [Fe/H]. We note that the RMS of the calcium abundance in M 4 is 0.04 dex, to be compared with the $\sigma_{\rm obs} = 0.07$ (see Table 3.5) that we found for the same element in M 22. We find a RMS in the calcium abundance almost equal to that found in M 4 when we divide our stellar sample into the

two *s*-process element rich and poor groups ($\sigma_{\rm obs}$ = 0.04 for both the two *s* groups).

The two stellar populations in M 4 and M 22 are apparently of different origin, or the mechanisms responsible for this dichotomy must have been operating with different efficiencies in the two clusters.

3.7 An independent check of our results

We have presented clear evidence of a spread in [Fe/H] and the presence of a bimodal distribution in the *s*-process element abundances of M 22 stars. These results are based on high resolution UVES spectra of seventeen stars. Because of the high relevance of these results to the ongoing lively debate about the multipopulation phenomenon in star clusters, we searched the ESO archive for additional spectra of M 22 stars to strengthen the statistical significance of our results for UVES data. We found GIRAFFE spectra data for 121 stars which we reduced. Data for only fourteen were in the appropriate RGB location to have high enough S/N to pass all of our quality checks (see the following discussion) and be useful to the abundance measurements. In any case, we were able to double the original UVES sample of stars.

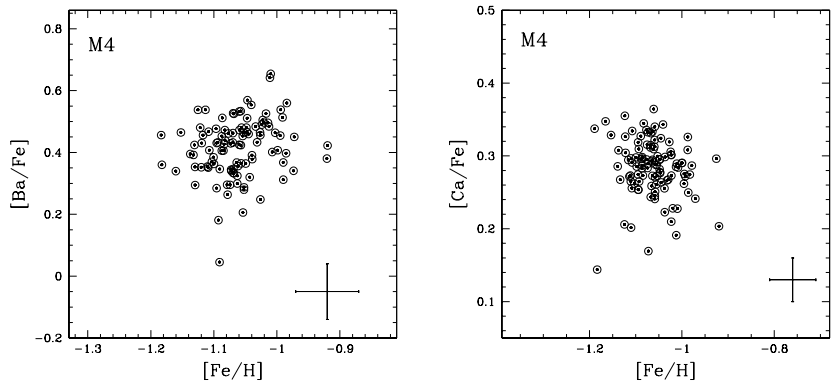

FIGURE 3.17— [Ba/Fe] (*left*), and [Ca/Fe] as a function [Fe/H] (*right*) for 104 stars in the GC M 4 (from Marino et al. 2008).

Each star was observed with HR09, HR13, and HR15 set-ups, which provided a resolution of about R∼20 000-25 000 in the wavelength ranges of 514-535, 612-640, and 660-696 nm, respectively. Data were reduced using the last version of the pipeline developed by Geneva observatory (Blecha et al. 2000), and were bias-subtracted, flat-field corrected, and extracted by applying a wave-

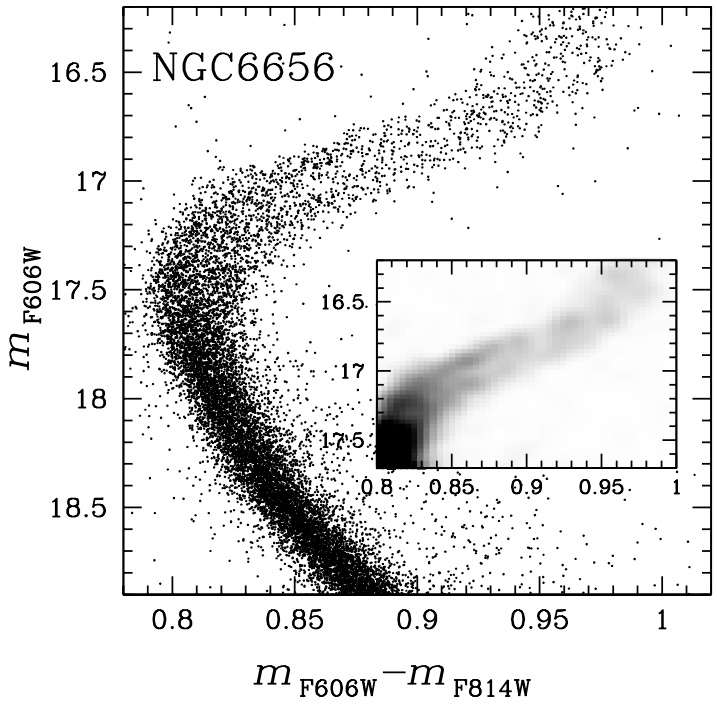

FIGURE 3.18— ACS/WFC CMD of M 22 from Piotto (2009).

length calibration derived with ThAr lamps. Each spectrum was then normalized. Finally, for each star we obtained a radial velocity and applied a membership criterion as performed for the UVES data. Spectra of each member star were then shifted to a velocity rest-frame and combined together. We also performed a test to verify the influence of scattered light on the spectral line shape, which could alter the final abundances. We also reduced some spectra covering the whole GIRAFFE CCD with and without scattered-light subtraction and compared spectral features. We found that scattered-light has no significant influence on the line strengths.

For GIRAFFE data analysis, we followed the same procedure for UVES, i.e., obtaining atmospheric parameters only from spectroscopy and not from photometry, which can be altered by differential reddening. This approach has the advantage of placing the abundance determinations from the two data sets on the same abundance scale, avoiding systematic effects. However, this choice, coupled with the selection of stars located only in the RGB, required the

rejection of 103 spectra because of their low S/N($\leq$70-80). A high S/N ratio is necessary to measure a sufficient number of isolated FeI/II lines in GIRAFFE spectra, which have lower resolution and cover a smaller wavelength range than UVES. In addition, the brightest stars were not analyzed because of their very low temperature ($T_{eff} < 4000$). In this T_{eff} regime metal poor stars (as in the case of M 22) also have very strong lines, which are blended in the GIRAFFE data, preventing a reliable EW measurement.

After a star had passed our selection criteria, atmospheric parameters (and Fe content) were obtained by the EW method, as for the UVES data, using the same linelist for the spectral lines in common between the two set-ups.

Some comparisons are needed between the results obtained for data from the two spectrographs. Since we have only one star (#51) in common between the two data-sets, we could not compare the results directly (apart for this star). In Table 3.7, we list the chemical abundances in common obtained for this star from the two different data sets. We note that the atmospheric parameters are in agreement within the errors calculated for the UVES data, the values of Fe and Y abundances agree within the σ_{tot} margins of error listed in Table 3.5, while for the other elements there are larger discrepancies probably because of the errors associated with the GIRAFFE results (that we have not considered here). Since the comparison of one star is not enough to verify the compatibility between the two sets of abundances, we compared the atmospheric parameters and the mean metallicity.

Figure 3.20 summarizes our tests. Filled circles represent GIRAFFE results and open squares the UVES ones. In the upper left panel, we plot log(g) as a function of T_{eff}, while the upper right panel shows v_t versus log(g). Both gravity as a function of temperature and microturbolence velocity as a function of gravity follow the same general trend for the two datasets, with similar dispersions. Further tests are shown in the two lower panels. The lower left one shows the Fe abundance vs. V magnitude (i.e., as a function of the evolutionary state of the star along the RGB). No correlation is apparent, meaning that no systematic errors due to the different evolutionary phase are present. The lower right panel reports T_{eff} vs. $B-V$ color. The line is the empirical relation by Alonso et al. (1999), obtained by assuming a reddening $E(B-V)$=0.34 (Harris 1996). In this case good agreement was also found, not only for the zero point of the relations (i.e., the absolute average reddening of the cluster), but also for the shape of the relations themselves.

An important test comes from the comparison of the mean iron content obtained from the two data-sets. From the fourteen GIRAFFE stars, we obtain

$$< [Fe/H] >= -1.74 \pm 0.03$$

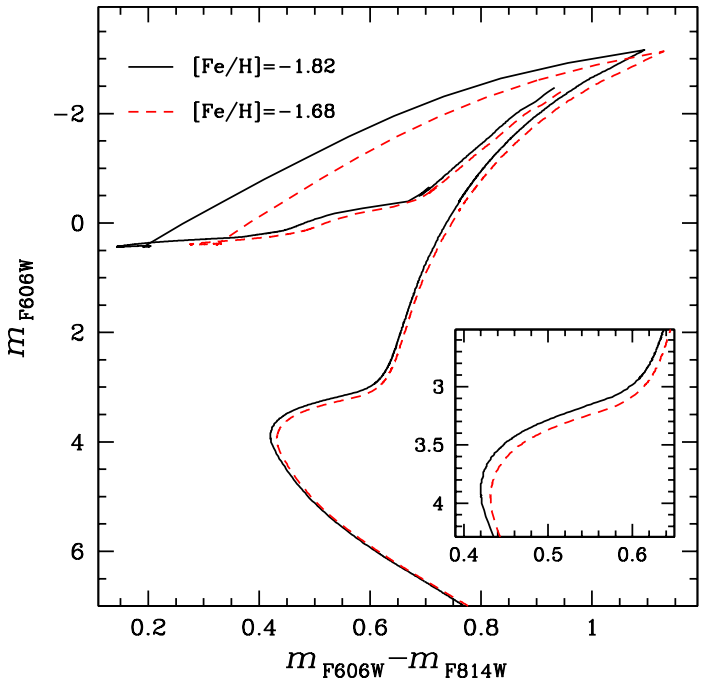

FIGURE 3.19— Red and blue lines are theoretical isochrones from Pietrinferni et al. (2004), with [Fe/H]=−1.68 and [Fe/H]=−1.82. The difference in metallicity produces in the CMD a split of the RGB and the SGB.

which perfectly agrees with the UVES value to within 1 σ.

A rough estimate of errors in the atmospheric parameters can be made as in Marino et al. (2008), assuming that stars of the same V magnitude (corrected for differential reddening) have the same parameters. In this way, we obtain: $\Delta T_{eff}=\pm 65$ K, $\Delta\log(g)=\pm 0.20$, and $\Delta v_t=\pm 0.11$ km/s. We can see that the errors are a bit larger, but still comparable with UVES ones.

All the other elements, with the exception of Ti, in GIRAFFE data were measured by spectral synthesis because of the severe blends with other lines. In addition to Fe and Ti, we measured O (from the forbidden line at 630 nm), Na (from the doublet at 615 nm), Y (from the doublet at 520 nm), Ba (from the line at 614 nm), Nd (from the line at 532 nm), and Eu (from the line at 665 nm).

After verifying the good agreement between the atmospheric parameters and the iron content obtained from the two data-sets, we proceed by verifying

whether the results for the GIRAFFE data agree with our UVES results. For this reason, in Fig. 3.21 we show some of the trends discussed in the previous sections. Filled circles are GIRAFFE measurements, while open circles are UVES ones. It is clear from this comparison that UVES results are fully confirmed. In particular, we can confirm the Y-Ba bimodality (central panel), as well as the different Fe content for the two *s*-element rich and *s*-element poor groups of stars (see leftmost and rightmost middle panels).

In addition, from GIRAFFE data we also measured Nd (a combined *s* and *r* element) and Eu (a pure *r* element) lines. Their abundances as a function of [Fe/H] are shown in the central and right lower panels. No trend is evident for [Eu/Fe], while [Nd/Fe] clearly correlates with [Fe/H]. This is further evidence that the iron enrichment of the *s*-process rich group is caused by core-collapse SNe.

TABLE 3.7— Atmospheric parameters and chemical abundances for the star #51 obtained from UVES and GIRAFFE data.

	T_{eff}	log(g)	v_t	$[\frac{Fe}{H}]$	$[\frac{O}{Fe}]$	$[\frac{Na}{Fe}]$	$[\frac{Ti}{Fe}]$	$[\frac{Ni}{Fe}]$	$[\frac{Y}{Fe}]$	$[\frac{Ba}{Fe}]$
UVES	4260	0.90	1.60	−1.63	−0.05	0.74	0.23	−0.07	0.32	0.40
GIRAFFE	4300	1.05	1.75	−1.55	0.05	0.60	0.38	−0.18	0.29	0.59

3.8 Additional data of RGB stars in M22

In this section I describe the results obtained from an additional sample of spectra of M22 coming from different telescopes. This new sample consists of spectra of RGB stars collected at McDonald (mcd), Apache Point (apo), Lick, and Anglo-Australian (AAT) Observatories. The spectral coverage of data is different, depending on the telescope, with AAT spectra in the range ∼5200-6800 Å, and mcd, apo and lick spectra ranging from *U* to infrared. The S/N ratio of data goes from ∼50 at ∼4800 Å to ∼130 at ∼6800 Å. In Tab.3.8 the analyzed stars identifications (from Peterson & Cudworth 1994) are listed together with the telescopes at which they were observed.

3.8.1 Spectroscopic analysis

For these spectra, we performed the same analysis used for UVES spectra (see Sect. 3.2 for more details). We analyzed the spectral region between 4800 and 6800 Å, that corresponds to the wavelength coverage of the UVES data, we used the same linelist, and the same method to obtain atmospheric parameters that, as fully explained in Sect. 3.2, were derived from Fe spectral lines.

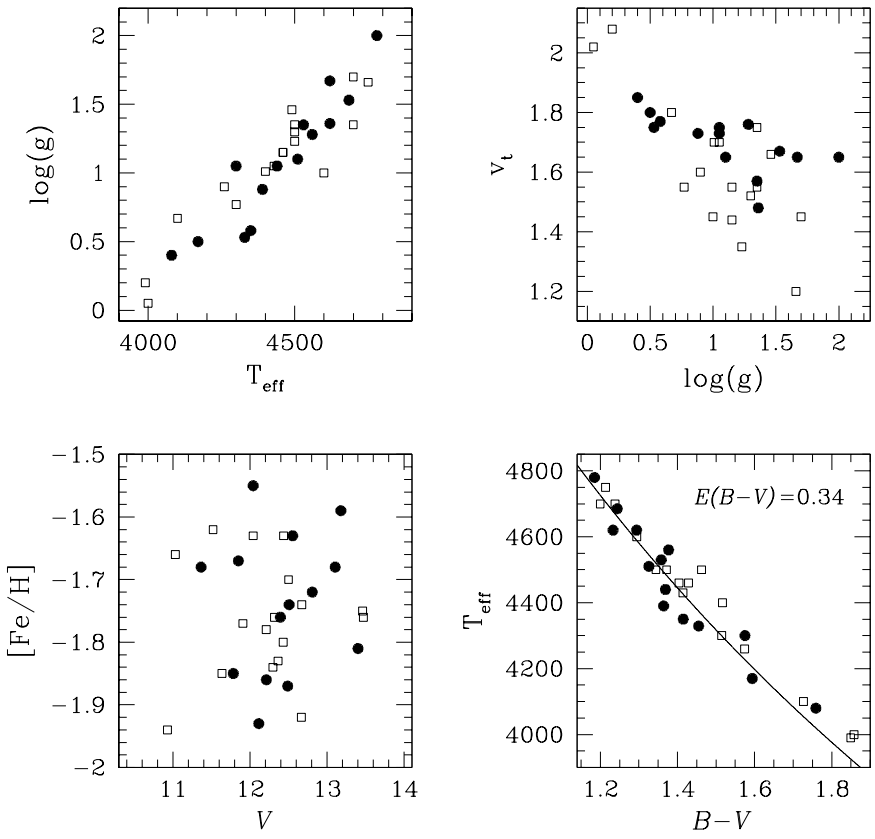

FIGURE 3.20— Check of the atmospheric parameters used in this paper. Filled circles are GIRAFFE stars, while open squares are UVES ones. See Sect. 8 for a full explanation.

In Tab.3.9 the obtained atmospheric parameters $T_{\rm eff}$, log(g), metallicity (considered as [Fe/H]), and v_t are listed, with the telescope (Col. 2) where each star was observed. For stars with more observations, the model atmospheres derived from each telescope are reported, together with the averaged parameters. To verify our adopted atmospheric parameters we performed some tests represented in Fig.3.22. In the left and middle panels we compare temperatures and gravities derived from spectroscopy ($T_{\rm EP}$, $\log(g)_{\rm IE}$) with the ones obtained from photometry. Photometric temperatures $T_{(V-K)}$ have been derived from the colors $(V-K)$ corrected for differential extinction, by using

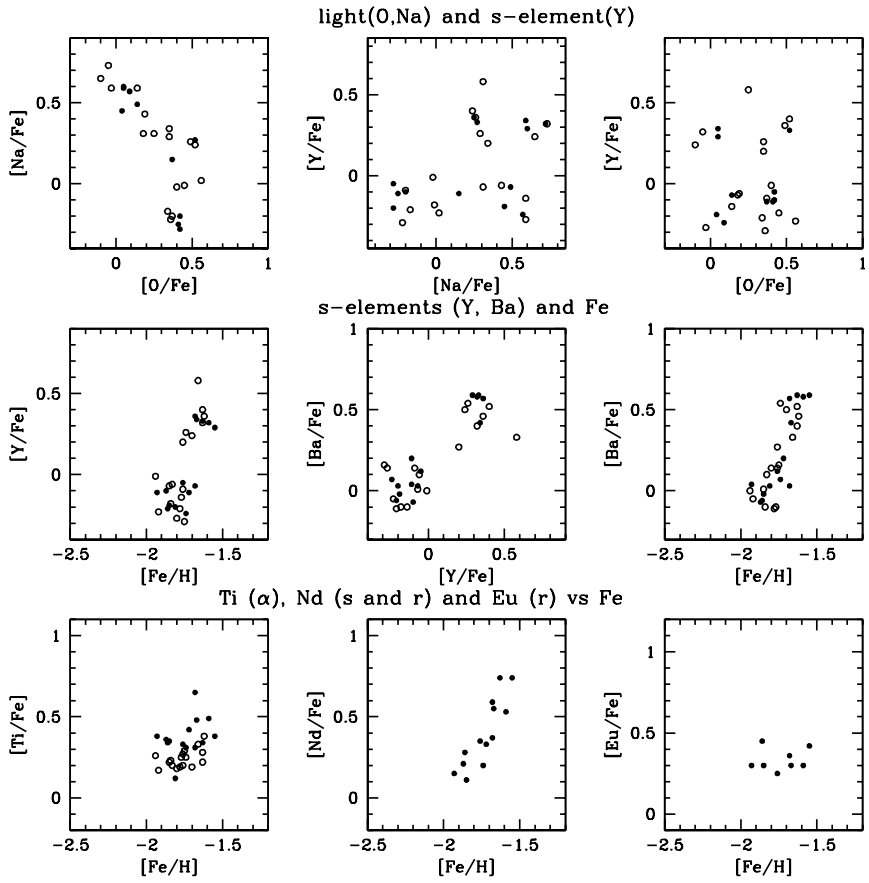

FIGURE 3.21— Comparison of our final results we obtained for UVES (open circles) and GIRAFFE (filled circles).

the calibrations by Alonso et al. (1999, 2000), and reddening corrections recommended by Harris (1996) of $E(B-V)$=0.34, and Cardelli et al. (1989) for $E(V-K)/E(B-V) = 2.75$. The scatter of the points plotted in the left panel of Fig.3.22 is ∼50 K, both in T_{EP} and $T_{(V-K)}$, that is what we expect from observational errors. Since we used colors corrected for differential reddening, we have minimized this effect in $T_{(V-K)}$. Photometric gravities $\log(g)_{\rm photometry}$ were determined by $T_{(V-K)}$ and bolometric magnitude (M_{bol}) through the standard relation:

$$log(g) = 0.40(M_{bol} - M_{bol,\odot}) + log(g_{\odot}) + 4(log(T/T_{\odot})) \quad (3.1)$$

by using the bolometric corrections from Alonso et al. (1999), and a distance modulus of $(m - M)_V = 13.60$ (Harris 1996). In the right panel we show spectroscopic log(g) values compared with estimates based on spectroscopic gravity calibrations of GCs provided by Kučinskas et al. (2006). All the tests represented in Fig.3.22 show that our estimates of the atmospheric parameters are quite reliable, some offset ($\sim \pm 50$ K in temperature, and $\sim \pm 0.15$ in gravities) are present between the photometric and spectroscopic parameters, but are comparable with the uncertainties.

For Lick, AAT, APO and McD spectra we obtained the abundances for Fe, La, Eu, Na and O, using the LTE line analysis code MOOG (Sneden 1973). Model atmospheres were interpolated from the grid of Kurucz models (with overshooting) by using the values of T_{eff}, log(g), metallicities, and v_t determined as previously explained. Iron was obtained from an EWs analysis, for all the other abundances we used spectral synthesis.

3.8.2 Chemical abundances

From the analysis of this additional sample of data we obtained a mean iron abundance of:

$$[Fe/H] = -1.76 \pm 0.02 \text{ dex}, \sigma_{obs} = 0.12$$

where σ_{obs} is the RMS, and the error is the internal error. The obtained mean value for iron is in agreement with the one derived from UVES and GIRAFFE. In Fig.3.24, as done for UVES spectra in Fig.3.9, we compare some iron spectral lines for stars with similar [Fe/H] (lower panels), and with a difference in [Fe/H] (upper panels) observed with AAT. In Fig.3.23 we show the distribution of [Fe/H] obtained from the new analyzed data, with superimposed the histograms obtained from UVES and GIRAFFE data in blue and red respectively. Yet, from this distribution, we see that the iron is intrinsically spread, and mainly from the new sample of stars, it appears to be bimodal.

Lanthanium

As discussed in previous sections, the iron intrinsic variations in M22 are related to the bimodality in s elements. Here we determine the abundance of another s element, lanthanium. Lanthanium abundances were derived from spectral synthesis of the lines at 6262, 6390, and 6774Å. The hyperfine splitting has been taken into account for the lines at 6262 and 6390 Å by using data from Lawler et al. (2001). As an example, some synthesis for the La spectral lines are shown

TABLE 3.8— Identifications (ID, from Peterson & Cudworth 1994) of the additional analyzed sample of stars, and telescopes at which each star was observed.

ID	Lick	McD	APO	AAT
I-36	×			
III-52	×			
I-37	×			
I-92	×			
II-1	×			
II-31	×			
III-14	×			×
III-15	×			
IV-102	×	×		×
V-2	×			
C		×		
II-96		×		
III-12		×		×
III-3		×	×	
I-12		×		×
I-27			×	
I-57			×	×
C513			×	
I-86				×
III-47			×	
IV-76				×
III-96				×
IV-20				×
IV-88				×

for three different stars in Fig.3.25. Our results for La abundances are shown in Fig.3.26, where data collected at different telescopes are shown with different symbols. In the top panels we represent [La/Fe] versus [Fe/H] obtained from single lines, while in the bottom panel the mean La abundances from the three lines are shown. Each spectral line confirms the bimodality in the abundance of s elements found from UVES and GIRAFFE data in M22. La rich (s-rich) stars, represented as filled symbols in Fig.3.26, have also higher Fe abundances, La (s-poor) stars, represented as open symbols, show lower Fe. The s-rich group has a mean [La/Fe]=+0.32 ± 0.04, the s-poor one [La/Fe]=+0.01 ± 0.02 dex. The mean iron abundance for the two groups are [Fe/H]=−1.66 ± 0.01 and [Fe/H]=−1.85 ± 0.02 dex, for s-rich and s-poor stars respectively, in agreement,

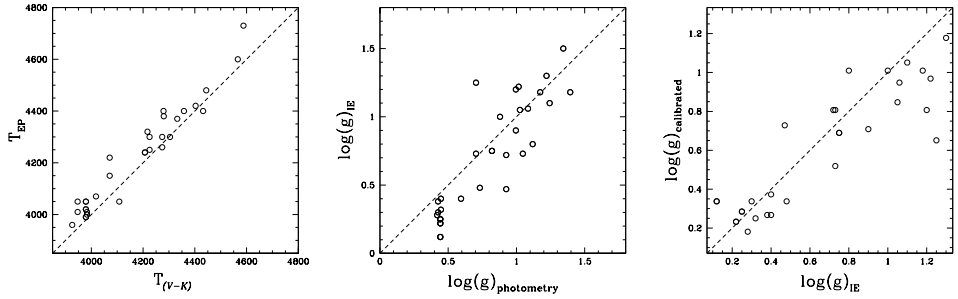

FIGURE 3.22— *Left panel*: Our adopted temperatures derived from the potential equilibrium (T_{EP}) are plotted as a function of photometric temperatures obtained from $(V-K)$ colors. *Middle panel*: Adopted gravities from ionization equilibrium ($\log(g)_{IE}$) as a function of gravities obtained from the standard relation 3.1. *Right panel*: Adopted gravities versus the calibrated T_{eff}-log(g) relation from Kučinskas et al. (2006). In all panels the straight line indicates the perfect agreement.

within the errors, with the UVES and GIRAFFE results.

Europium

Europium abundances were determined from the spectral synthesis of the line at 6645 Å and considering the hyperfine splitting structure provided by Sneden et al. (2004). Eu contents were derived for Lick, McD, and APO spectra, while AAT data do not cover the spectral region around the Eu line. Due to the poor S/N (<30) and the line crowding we could not obtain reliable abundances from the other Eu lines present in the blue-violet region.

We obtained a mean [Eu/Fe]=+0.25±0.02 (σ=0.07). Results for the Eu abundances are shown in Fig.3.27 where we represent the s-rich and s-poor stars by filled and open symbols respectively, and data from different telescopes are plotted by using different symbols (as in Fig.3.26). In the right and middle panels we show [Eu/Fe] as a function of [Fe/H] and [La/Fe], with error bars associated to the two groups representing the mean abundances, and the corresponding errors, found for s-rich and s-poor stars. In each panel of Fig.3.27 are represented also the error bar representing the uncertainty associated to each single measure, calculated averaging RMSs of abundances for the two groups. The mean abundances for s-poor and s-rich stars are [Eu/Fe]=0.29±0.02, and [Eu/Fe]=0.22±0.07 respectively, in agreement within $\sim 1\sigma$ level. We note also that there are three stars observed at Lick that should be outliers. However, as shown in the right panel, [Eu/Fe] does not vary with [Fe/H] within 1 σ level. We conclude that, within our errors, we do not find variations of [Eu/Fe] contents

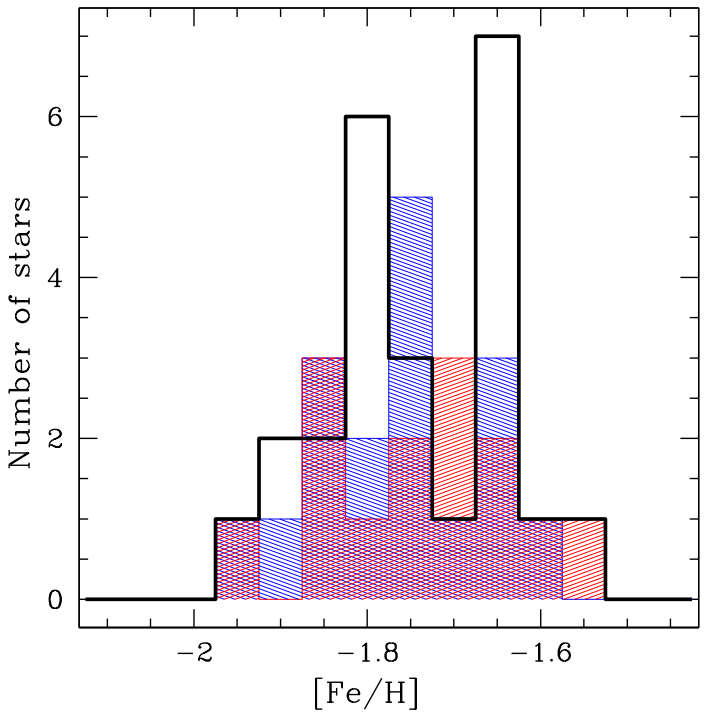

FIGURE 3.23— Iron distribution obtained from the new sample of data. For stars with multiple observations we used the average metallicity listed in Tab.3.9. The over-imposed histograms shaded in blue and red are the distributions obtained from UVES and GIRAFFE data respectively.

in the two s-groups.

In the right panel of Fig.3.27, we show the ratio [La/Eu] as a function of iron. A significant difference in the [La/Eu] ratio is present between s-rich and s-poor stars: the s-poor group has a mean [La/Eu]+0.15±0.09, the s-rich one shows higher values with a mean [La/Eu]=+1.52±0.28.

NaO anticorrelation

We determine Na abundances from spectral synthesis of the two doublets at 5680 Å and 6150 Å. Oxygen content was obtained from the synthesis of the forbidden line at 6300 Å, once cleaned our spectra from tellurics by dividing for a telluric standards observed the same nights of M22 stars.

In Fig.3.28 Na abundances are plotted as a function of O. Results obtained

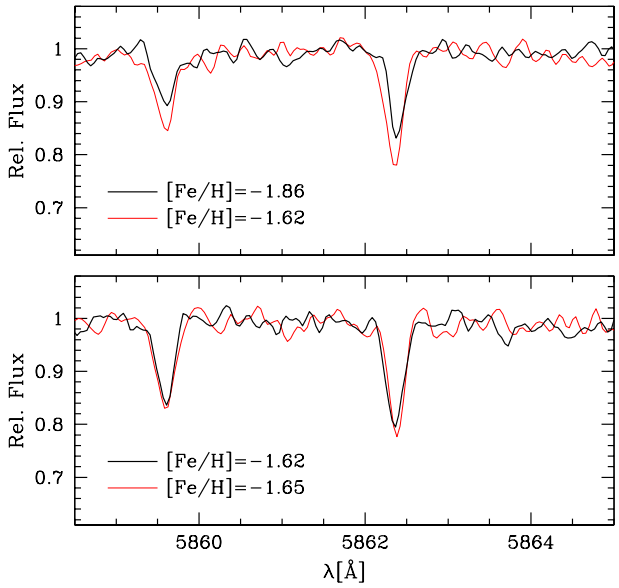

FIGURE 3.24— As in Fig.3.9 for two AAT spectra. In upper panels we represent the two stars I-12 and I-57, in lower panels the two stars IV-88 and IV-20.

from the entire analyzed sample of data have been plotted with different symbols corresponding to data from the various telescopes. For stars that were observed at more the one telescope, we represent all the results from different data, indicating measures of the same star with a single color.

Na and O define the NaO anticorrelation, as also found from FLAMES data. In Fig.3.29 the NaO anticorrelation obtained from the new analyzed set of spectra (points with large circles) are over-imposed to the results derived from the analysis of UVES and GIRAFFE spectra (points with small squares). In red we represent the stars belonging to the s-rich group, in blue the stars of the s-poor group. Measures from the heterogeneous data are in agreement and we can conclude that there are not serious problems or offsets between different type of spectra.

Results plotted in Fig.3.29 indicate that the NaO anticorrelation is present in both the populations with different s abundance hosted in M22. The s-rich and s-poor stars appear to span a similar range in oxygen that goes from [O/Fe]$\sim$0 to [O/Fe]$\sim$0.6 dex. On the contrary, evidence for a different level of the sodium s-poor and s-rich groups are present: the NaO anticorrelation starts

from significantly lower Na ([Na/Fe]~-0.25) and also extends until slightly lower Na ([Na/Fe]$\sim+0.6$) for s-poor stars, for s-rich stars NaO anticorrelation ranges from [Na/Fe]>0 to [Na/Fe]>0.6. Figure 3.30 shows the difference in the NaO anticorrelation between the two stellar groups. In the left panel the NaO anticorrelation for s-poor stars is represented, with a fiducial line drawn by hand, in the right panel we over-impose to the same fiducial the abundances for s-rich stars. From our results it is evident that both the populations in M22 show the NaO anticorrelation, each defining different tracks on the Na-O plane. This difference is also shown in Fig.3.31 where Na abundances are represented as a function of Fe.

3.9 The red giant branch

Richter et al. (1999) by using Strömgren photometry revealed that M22 exhibits a bimodal distribution in the m_1 index among RGB stars that they associated to CN variations.

At the light of our results on the presence of two populations with different s elements, and iron in M22, we match our spectroscopic data with their Strömgren photometry. Results are shown in Fig.3.32 where we over-imposed all our spectroscopic data with available photometry on the I versus the m_1 CMD, carefully corrected for differential reddening. It is evident that s-Fe poor and s-Fe rich stars separate on RGB, defining two different sequences. The s poor population is distributed on the CN-poor branch, and the s poor stars on the CN-rich one. This is also indicated by Fig.3.33 where we represent the S(3839) index from Norris & Freeman (1983) as a function of our derived [Fe/H] values: the two groups of stars clearly correlate with the index S(3839). This indicates that the two s groups in M22 are related to variations in CN band strengths.

3.10 Conclusions

We have presented a high resolution spectroscopic analysis of seventeen RGB stars in the GC M 22 from UVES and FLAMES+UVES data.

We confirm that M 22 is a metal poor GC, with a mean iron content of [Fe/H]$=-1.75 \pm 0.02$ (weighted mean between UVES and GIRAFFE) and a mean α-enhancement [α/Fe]$=+0.36 \pm 0.04$. Sodium and oxygen follow the well known anticorrelation, while there is no evidence of a MgAl anticorrelation. A clear correlation was found between Na and Al.

We found a clear dichotomy in the distribution of the *s*-process elements barium, yttrium, and zirconium. Most importantly, we found that the abundance of these elements is correlated with iron. Stars enriched in *s*-process

elements also exhibit systematically higher values of [Fe/H], by $\sim$ 0.14 dex. The correlation between *s*-process elements, and Ca abundances, with [Fe/H] is the strongest support for the presence of two groups of stars with a different Fe content in M 22. The *s*-process element abundance correlates with calcium, and the calcium with the iron abundance. The s rich stars also show an overabundance of magnesium and silicon.

All these results have been confirmed for a sample of fourteen lower resolution GIRAFFE spectra, which has allowed us to double our original UVES sample.

Moreover, we analyzed an additional set of spectra of M 22 RGBs coming from different telescopes (Lick, McD, APO and AAT). From these data we determined the abundance of lanthanium, that similarly to the other studied s elements, has a bimodal distribution that corresponds to the difference in iron. Europium does not change, within observational errors, as a function of metallicity. The [La/Eu] ratio is different for the two s groups, with s rich stars at high values of [La/Eu]>1.5 indicating the domination by the s-process, similarly to the case of ω Centauri (Johnson et al. 2008).

No clear correlation is present between *s*-process elements and sodium, and between iron and sodium, but we noted that *s*-element and Fe enriched stars show higher values of sodium. Both the populations in M22 show the NaO anticorrelation, but the Na range is different.

The s poor and s rich stars show a bimodal distribution in Strömgren photometry, with s rich group populating the RGB related to the CN-rich stars and s poor group the sequence of CN-poor stars (Richter et al. 1999).

We investigated if the difference in iron can account for the M22 SGB split. According to theoretical models by Pietrinferni et al. (2004), a difference in metallicity of 0.14 dex should cause a difference of $\sim$0.10 mag in the F606W ACS/WFC band at the level of the SGB. Piotto (2009) indeed found that the SGB of M 22 is separated into two, distinct branches. However, the average separation in F606W band is of the order of 0.17 magnitudes: it appears that the SGB split cannot be caused by a difference in [Fe/H] alone.

The fraction of stars on the bright SGB (bSGB) corresponds to 62%$\pm$5% of the total SGB population, while the faint SGB (fSGB) includes the remaining 38%$\pm$5% of the SGB stars (Piotto 2009). In the stellar sample of the present paper, the fraction of Ba-strong, Y-strong, Zr-strong stars is $\sim$41%. It is therefore tempting to connect the *s*-process element poor sample to the bright SGB stars, while the faint SGB stars could be the stars with enhanced *s*-process elements. The correct reproduction of the two SGBs requires an accurate determination of the NaCNO abundances, as shown by Cassisi et al. (2008) for the analogous case of NGC 1851. He variations between the two populations

can also affect the SGB morphology. We note that M 22 shares similarities with ω Centauri and NGC 1851: these clusters, where multiple stellar populations have been photometrically identified along the SGB, exhibit a large range, not only in C, N, O, Na, Al, but also in *s*-process element abundance. M 22 is the only globular, apart from ω Centauri, where some evidence of an intrinsic spread in iron has been observed. Some hints (even if very uncertain due to the low number statistics of the analyzed sample) of a some iron spread in NGC 1851 was suggested by Yong & Grundahl (2008). NGC 1851, ω Centauri, and M 22 show a large variation in the Strömgren index, traditionally used as a metallicity indicator. All of these three GCs exhibit a splitted SGB.

From our observations and the results of Piotto (2009), it is tempting to speculate that the SGB split could be related to the presence of two groups of stars with different *s*-process element contents and a difference, albeit small, in iron. According to this interpretation, *s*-process element poor stars would correspond to the brighter SGB stars and constitute the first M 22 population. The second stellar generation should have been formed after the AGB winds of this first stellar generation had polluted the protocluster interstellar medium with *s*-process elements. This second generation may have formed from material that was also enriched by core-collapse supernovae ejecta, as indicated by their higher iron, magnesium, and silicon content, and the lack of correlation of the iron content with a pure r-process element (Eu). A detailed analysis of the C, N, and O abundances of SGB stars in M 22 is strongly needed to resolve this problem.

TABLE 3.9— Atmospheric parameters for the analyzed stars. In Col. 2 the telescope at which the star was observed is also listed.

ID	telescope	T_{eff} [K]	log(g)	v_t [km s^{-1}]	[Fe/H] [dex]
I-36	lick	4400	0.80	1.70	−1.89
III-52	lick	4050	0.48	1.70	−1.63
I-37	lick	4370	1.06	1.52	−1.73
I-92	lick	4240	0.75	1.55	−1.75
II-1	lick	4300	0.73	1.50	−1.66
II-31	lick	4380	1.22	1.65	−1.65
III-15	lick	4070	0.40	1.85	−1.82
V-2	lick	4130	0.65	1.75	−1.57
C	mcd	3960	0.28	2.23	−1.69
II-96	mcd	4400	1.00	2.12	−1.82
I-27	apo	4420	1.43	1.58	−1.82
C513	apo	4100	0.40	1.65	−1.86
I-86	aat	4420	1.10	1.20	−1.80
III-47	apo	4600	1.18	2.00	−1.82
IV-76	aat	4730	1.50	2.32	−1.63
III-96	aat	4480	1.30	1.65	−1.86
IV-20	aat	4320	1.05	1.70	−1.65
IV-88	aat	4400	1.18	1.72	−1.62
III-14	lick	4010	0.38	2.15	−1.84
	aat	4050	0.30	2.16	−1.80
	average	4030	0.34	2.16	−1.82
IV-102	lick	4020	0.25	2.15	−1.96
	mcd	4050	0.12	2.36	−1.95
	aat	3990	0.22	2.15	−2.01
	average	4020	0.20	2.22	−1.97
III-12	mcd	4150	0.73	1.94	−1.69
	aat	4220	1.25	2.00	−1.61
	average	4185	0.99	1.97	−1.65
III-3	mcd	4000	0.32	2.25	−1.72
	apo	4010	0.40	2.25	−1.78
	average	4005	0.36	2.25	−1.75
I-12	mcd	4260	0.47	1.54	−1.90
	aat	4300	0.72	1.72	−1.86
	average	4280	0.60	1.63	−1.88
I-57	apo	4300	1.20	1.68	−1.65
	aat	4250	0.90	1.66	−1.62
	average	4275	1.05	1.67	−1.64

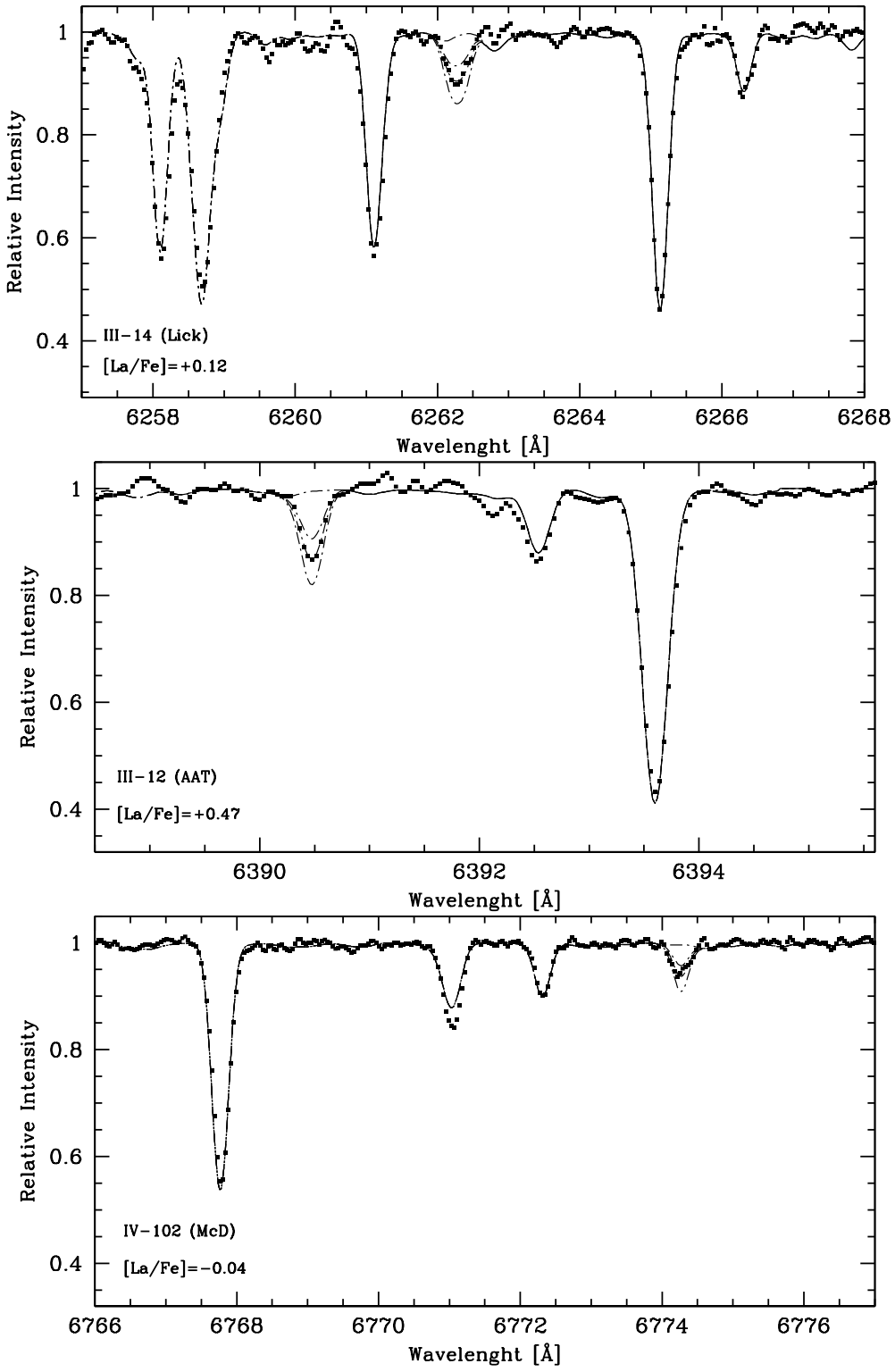

FIGURE 3.25— Sample spectrum syntheses are shown for the La spectral lines at 6262 Å (top panel), 6390 Å (middle panel) and 6774 Å (bottom panel). Three stars with different [La/Fe] abundances and observed at different telescopes are shown. The synthesis without La, the synthesis of best fit with the observed spectrum, and deviations of ±0.20 dex are shown. Atmospheric parameters used for these synthesis are listed in Tab.3.9.

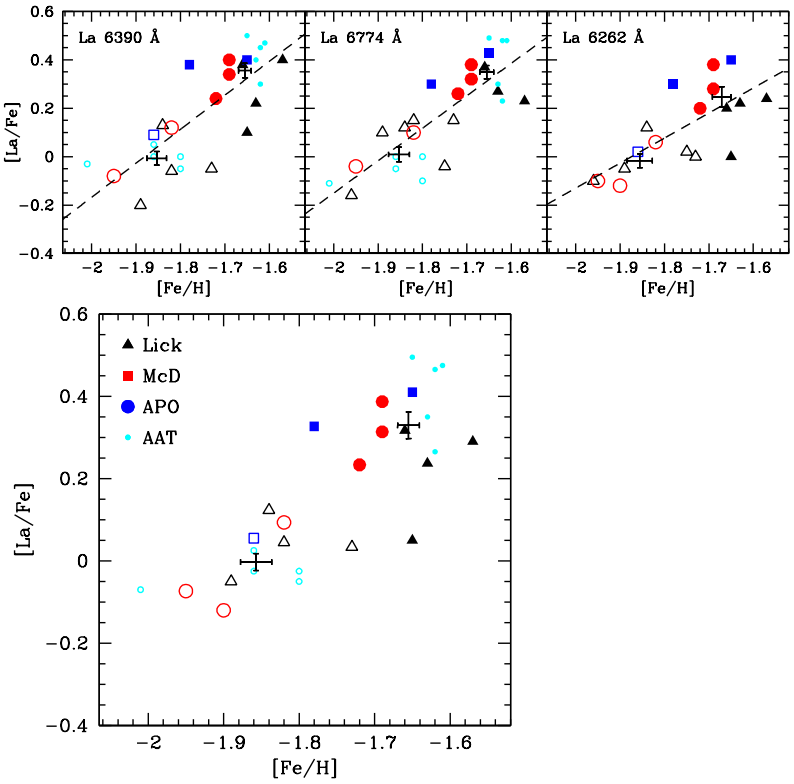

FIGURE 3.26— [La/Fe] as a function of [Fe/H]: In the top panels the results obtained from the 6390, 6774, and 6262 Å lines are shown, the mean La abundances from all the spectral lines are represented in the lower panel. In all panels, open symbols represent the s (and Fe) poor stars, filled symbols the s (and Fe) rich ones, error bars indicate the average abundances of stars in each group, dashed lines are the best least squares fitting straight lines. Different colors and symbols correspond to data collected at different telescopes.

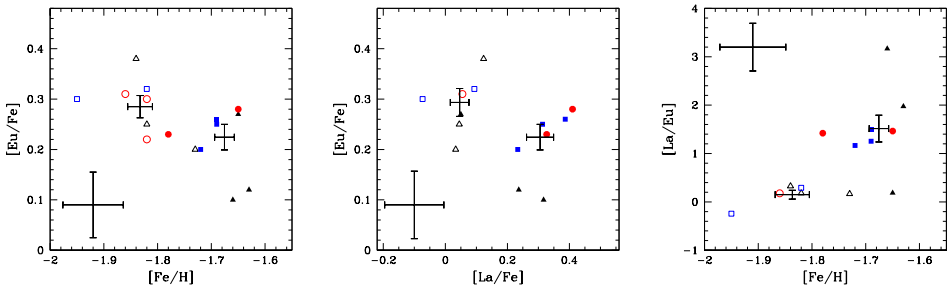

FIGURE 3.27— From left to right: [Eu/Fe] versus [Fe/H], versus [La/Fe], and ratio [La/Eu] versus [Fe/H]. Symbols are as in Fig.3.26. Error bars represent the mean and the error of mean for each group, and the error associated to each single measure.

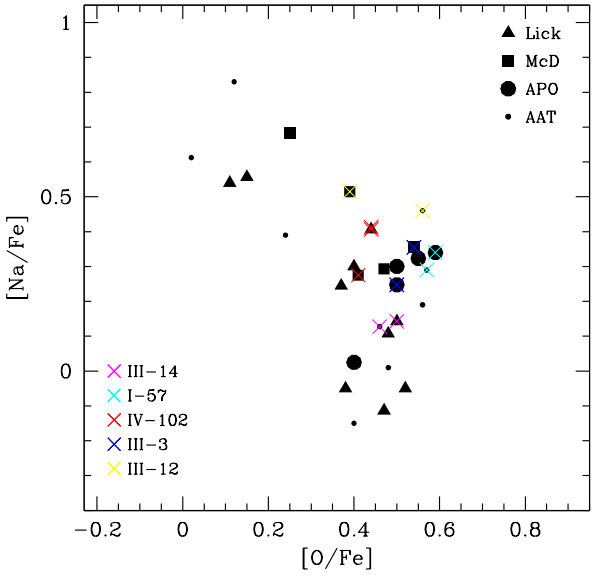

FIGURE 3.28— NaO anticorrelation determined from Lick, McD, APO, and AAT spectra. Data from different telescopes are represented with different symbols as indicated in the figure. Stars with multiple observations are marked with crosses of different colors.

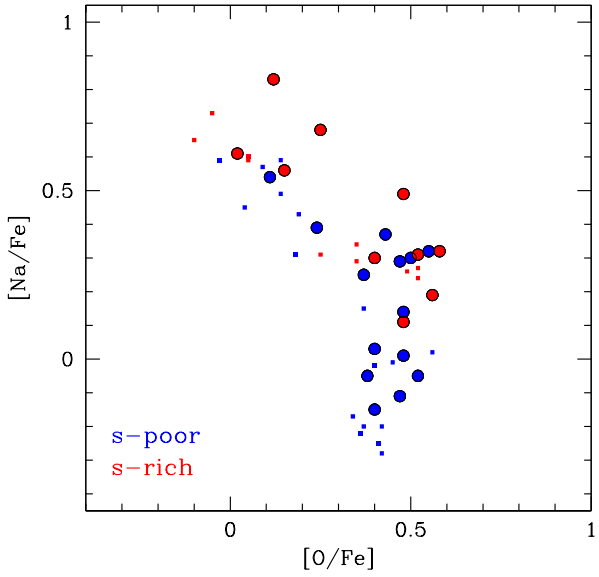

FIGURE 3.29— NaO anticorrelation for the new sample of data (large circles), and FLAMES data (small squares). For the new data we plotted the average abundances for stars with multiple observations. Red and blue colors represent s-rich and s-poor stars respectively.

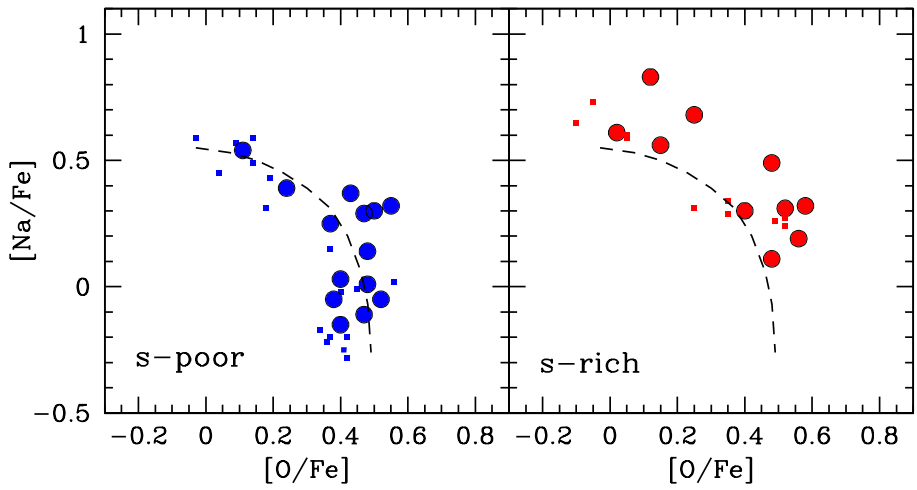

FIGURE 3.30— NaO anticorrelation for s-poor (right panel) and s-rich stars (left panel). Dashed line represents a fiducial for the s-poor group.

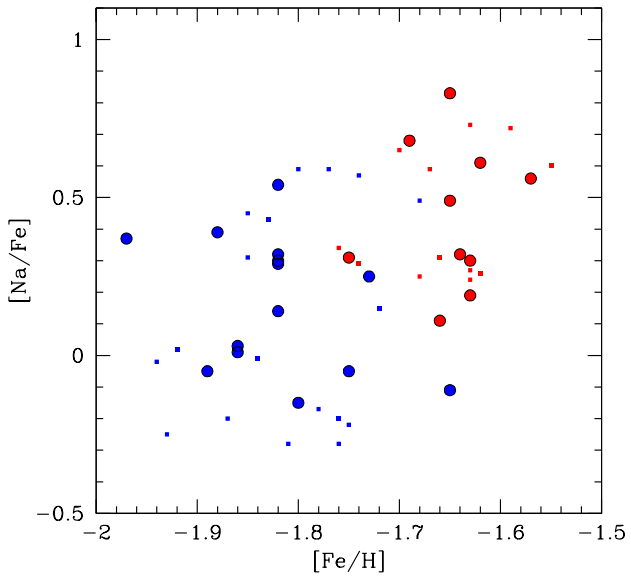

FIGURE 3.31— [Na/Fe] as a function of [Fe/H]. Symbols are as in Fig.3.29.

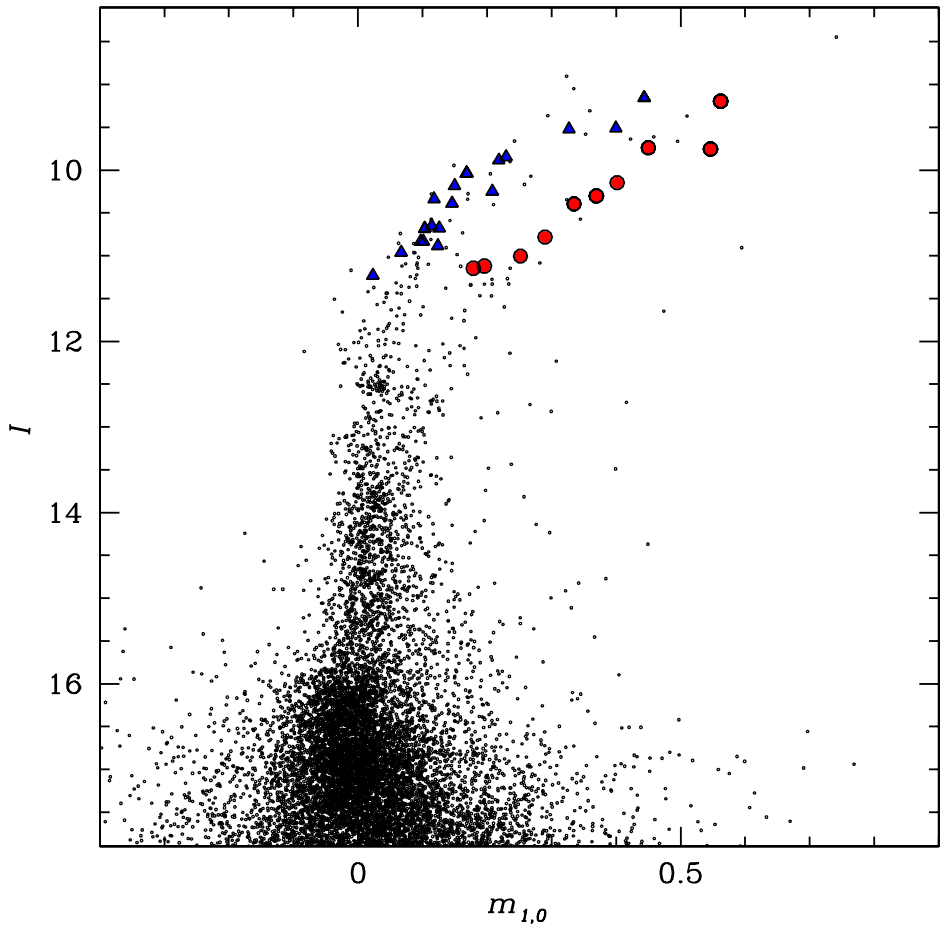

FIGURE 3.32— I-m_1 CMD for M22, corrected for differential reddening. Spectroscopic data are over-imposed with s-rich stars represented by red symbols, and s-poor stars by blue symbols.

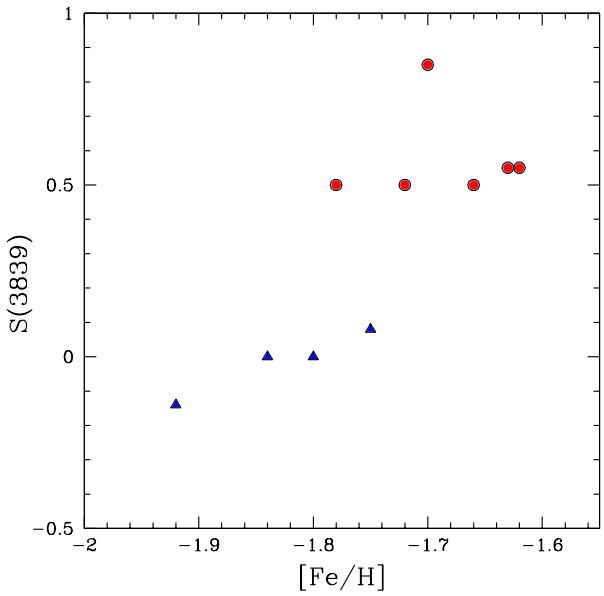

FIGURE 3.33— S(3839) index from Norris & Freeman (1983) as a function of [Fe/H]. Symbols are as in Fig.3.32.

4

Omega Centauri

ω Centauri is the most studied and enigmatic stellar system of our Galaxy. It hosts the most complex multiplicity of stellar populations observed in GCs, with an anomalous large spread in [Fe/H] that ranges from $\sim$−2.0 dex to $\sim$−0.6 dex (Cannon & Stobie 1973; Norris & Bessell 1975; Freeman & Rodgers 1975; Butler et al. 1978; Norris & Da Costa 1995; Suntzeff & Kraft 1996; Norris et al. 1996), with a primary component at [Fe/H] ~ -1.7 to -1.8, and a long tail extending up to [Fe/H] ~ -0.6, containing three or four secondary peaks (see Johnson et al. 2009) for a recent update.

The ω Centauri stars also show large variations in chemical abundances for several elements, not only light elements (as observed in all GCs), but also in some heavy elements. As an example, the more metal rich stars are strongly enriched in s elements.

The complexity of ω Centauri stellar populations has been revealed both from ground-based photometry (Lee et al. 1999; Pancino et al. 2000; Rey et al. 2004; Sollima et al. 2005a; Villanova et al. 2007) and *Hubble Space Telescope* (*HST*) photometry (Bedin et al. 2004; Ferraro et al. 2004) that have shown that ω Centauri hosts different stellar populations, most of them clearly visible in most of their evolutionary phases.

The populations have been linked to the mentioned metallicity peaks, in photometric studies of the red-giant branch (RGB) (Pancino et al. 2000; Hilker & Richtler 2000; Sollima et al. 2005a), the subgiant branch (SGB) (Hilker et al. 2004; Sollima et al. 2005b; Stanford et al. 2006; Villanova et al. 2007), and the main sequence (MS) (Piotto et al. 2005). The most puzzling feature in ω Centauri was discovered by Piotto et al. (2005), who showed that, contrary to any expectation from stellar-structure theory, the bluer of the two principal

main sequences (bMS) is more metal-rich than the redder one (rMS). The only possible way of reconciling the spectroscopic observations with the photometric ones is to assume a high overabundance of He for the bluer MS (Bedin et al. 2004; Norris 2004; Piotto et al. 2005). How such a high He content could have been formed is still a subject of debate (see Renzini 2008 for a review). A scenario proposed to account for the observed peculiarities of this object is a tidal stripping of an originally much more massive object (Zinnecker et al. 1988; Freeman 1993; Dinescu et al. 1999; Ideta & Makino 2004; Tsuchiya et al. 2004; Bekki & Norris 2006). In this scenario, ω Centauri was born as a dwarf elliptical galaxy subsequently disrupted by the Milky Way.

Very recently, it has been shown that some peculiar features observed in ω Centauri are shared with other GCs: A spread in s elements is present also in NGC 1851 (Yong et al. 2008) and M22 (Marino et al. 2009), and intrinsic variations in [Fe/H] were detected in M22 (Marino et al. 2009). These findings suggest that ω Centauri could not be so peculiar, but a real GC, possibly in a particular stage of its evolution. However ω Centauri still remains the most exceptional GC in the Milky Way as concerns its complex of numerous populations of stars clearly indicated both from spectroscopy and photometry.

Here we present a spectroscopic study of a large and homogeneously analyzed sample of RGB stars distributed on the different branches in the CMD. We analyzed the chemical abundances of iron, sodium, oxygen and s elements in order to characterize the different stellar populations hosted in ω Centauri in terms of their chemical content.

4.1 Observations

In order to investigate the complex stellar population system of ω Cen and shed new light on its star formation history we coupled a large number of mid and high resolution spectra from UVES and GIRAFFE@VLT, with high accuracy photometry taken both with *HST* and ground based telescopes.

4.1.1 Spectroscopic data

Data set consists in a large amount of FLAMES/UVES [proposal 082.D-0424(A)] and FLAMES/GIRAFFE spectra [from archive: proposal 071.D-0217(A)].

GIRAFFE data include the four set-ups HR09B, HR11, HR13, and HR15 with spectral coverage of 5095-5404, 5597-5840, 6120-6405, 6607-6965 Å, respectively, and a resolution of $R \sim$ 20 000-25 000. The stars analyzed with GIRAFFE consist in a sample of 201 RGB with a V magnitude brighter than 15. Among these stars a sample of 68 giants were observed with the four GIRAFFE set-ups, for the remaining 133 stars we have available the two set-ups

HR09 and HR13. The typical S/N of GIRAFFE spectra is ∼70-100.

At high resolution (∼45 000) with UVES we observed a sample of 40 RGB stars. UVES spectra were obtained by using the RED 580 setting, and have a spectral coverage of ∼2000 Å with the central wavelength at 5800 Å. Each star was observed for four times, obtaining a final signal to noise ratio for the co-added spectra of ∼100-120.

We take advantage of the photometry obtained with the Wide Field Imager (WFI) camera at the ESO/MPI 2.2m telescope (total field of view 34 × 33 arcmin^2) (Bellini et al. 2009) corrected for differential reddening and cleaned for proper motions, in order to accurately identify the position of the spectroscopic sample on the CMD.

4.2 Data reduction and analysis

Data were reduced including bias subtraction, flat-field correction, wavelength calibration, sky subtraction and spectral rectification, by using the dedicated pipelines: BLDRS v0.5.3, written at the Geneva Observatory (see http://girbld-rs.sourceforge.net) for GIRAFFE, and the UVES pipeline (v2.9.7) (Ballester et al. 2000) for UVES. The chemical abundances were derived from a local thermodynamic equilibrium (LTE) equivalent width and spectrum synthesis analysis by using the spectral analysis code MOOG (C. Sneden 1973, PhD. Thesys). For the UVES spectra we derived the chemical abundances for Fe, Na, O, Mg, Al, and s elements from EQWs. For GIRAFFE, because of the lower resolution, apart from iron, whose abundances were determined from EWs, we determined the chemical contents for Na, O, Ba and La from spectral synthesis.

The chemical abundances analysis was performed by using model atmospheres extracted by interpolation from the grid by Kurucz (1992; models with overshooting). Atmospheric parameters defining these models were estimated as follows. Effective temperatures (T_{eff}) were obtained via empirical relations of the $(V-K)$ colors with temperatures by using the calibrations by Alonso et al. (1999, 2000). We used V magnitudes from Bellini et al. (2009), and K magnitudes retrieved from 2MASS catalog. Our final $(V-K)$ colors were corrected both for interstellar extinction using a $E(B-V)$ =0.12 (Harris 1996) and $E(V-K)/E(B-V)$ =2.70 (McCall 2004), and for differential reddening effects. We finally verified that our adopted photometric temperatures satisfied excitation equilibrium.

Surface gravities log(g) were obtained from T_{eff} through the canonical equation:

$$log(g/g_{\odot}) = log(M/M_{\odot}) + 4 \times log(T_{eff}/T_{\odot}) - log(L/L_{\odot}) \qquad (4.1)$$

where we adopted a mass of the star of M=0.80M$_\odot$, the bolometric correction from Alonso et al. (1999), and a distance modulus of $(m-M)_V$ =13.7 (van de Ven et al. 2006).

Microturbolent velocities were determined from Fe lines by removing trends in the EWs as a function of abundances.

4.3 Results

In this section I will describe the results obtained from the UVES and the GIRAFFE samples. In Sect.4.3.1 I describe the results obtained from GIRAFFE, whose larger sample allow us to study the overall properties of the different populations in ω Centauri. In Sect.4.3.2 I present the results obtained at high resolution with UVES.

4.3.1 Characterizing the chemical abundances of the ω Centauri populations from the GIRAFFE sample

Iron

As already said, ω Cen is the only GC with large star-to-star variations in [Fe/H].

A large number of photometric and spectroscopic studies (e.g. Norris & Da Costa 1995, van Leeuwen et al. 2000, Sollima et al. 2005, Villanova et al. 2007, Johnson et al. 2008, 2009) have shown that the several stellar populations span a wide range of metallicities that goes from [Fe/H]~ -2.0 to [Fe/H]~ -0.5.

Although it is now unequivocally accepted that more than half of stars have [Fe/H]~ -1.7 and the rest form a high metallicity tail (e.g. Sollima et al. 2005), it is not clear whether ω Cen stars are clustered around discrete [Fe/H] values or present a nearly continuous distribution.

Several authors detected distinct peaks in the metallicity distribution. Villanova et al. (2007) studied a sample of 48 SGB stars and found three populations with the bulk of stars having [Fe/H]=-1.68 and two less populated stellar groups located at [Fe/H]=-1.37, and [Fe/H]=-1.14.

Johnson et al. (2009) analyzed more than 200 RGB stars and detected four distinct peaks in the metallicity distribution having [Fe/H]=~ -1.75, ~ -1.45, ~ -1.05 and ~ -0.75. The 55% of ω Cen stars have [Fe/H]~ -1.75, while the other peaks constitute roughly the 30%, 10%, and 5% of their observations, respectively.

From our analysis of the GIRAFFE data for $N \sim 200$ RGB stars we find that the [Fe/H] ranges from ~ -2.1 to ~ -0.7 dex.

Fig.4.1 shows the B versus (U-I) from WFI photometry zoomed around the RGB. Stars for which iron measurements are available, are marked as large circles, with the grey scale proportional to the iron content. Most of the metal poor stars populate the bluest RGB and a well defined increasing of the [Fe/H] abundances is present towards redder RGBs. Nearly all the most metal rich stars are located along the RGB-a.

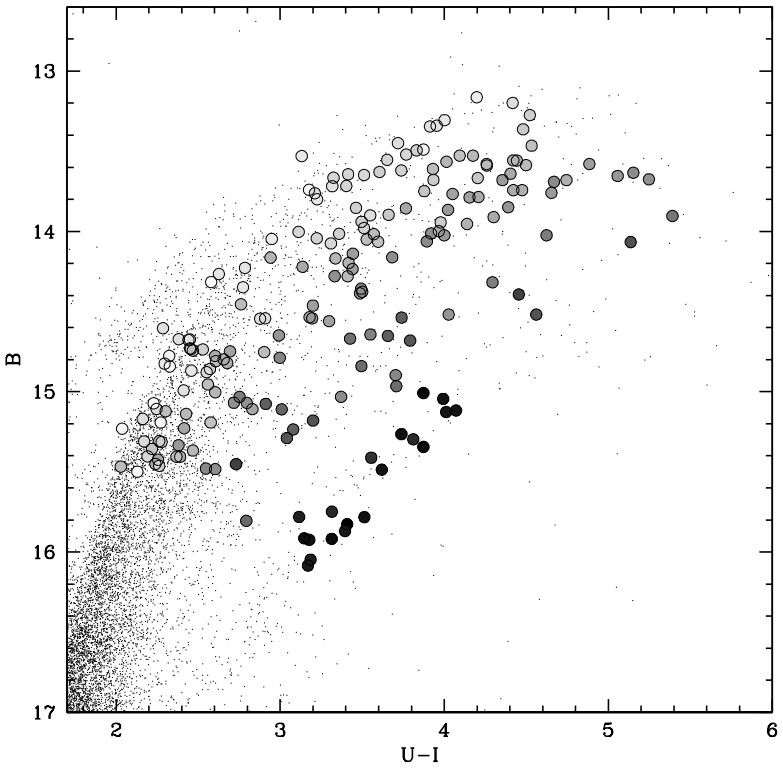

FIGURE 4.1— Position of the GIRAFFE sample on the B vs. $(U-I)$ WFI CMD. The stars are represented with a grey scale proportional to the obtained iron content.

The histogram of the normalized metallicity distribution is represented in Fig.4.2. The red over-imposed shaded curve is the normalized kernel density distribution:

$$K = \sum_{i=1}^{N} e^{\frac{-(x-x(i))^2}{2\sigma^2}}$$

where x = [Fe/H] and σ is the observational error associated to [Fe/H].

We used for each star $\sigma = 0.04$ dex that has been taken equal to the dispersion of the group of the RGB-a stars with [Fe/H]> -1.0. If we assume that all the RGB-a stars have the same [Fe/H] content, such value is indicative of the observational error.

A visual inspection at the histogram and the kernel density distribution suggests that ω Cen has five peaks at [Fe/H] ~-1.82, ~-1.65, ~-1.50, ~-1.20, and ~-0.85.

In Fig.4.3 we simulated the histogram distribution expected for five distinct stellar groups with the observed discrete metallicity values. The relative numbers of stars are chosen to match the observed distribution, and the errors associated to each [Fe/H] value correspond to the average observational error. Simulations (black histogram) are compared with the observations (red histogram).

The histogram distribution [Fe/H] is significantly much broaden than simulated histogram, suggesting that the observed spread in iron is much larger than expected from observational errors alone

In particular, the tail towards [Fe/H]~-1.95 suggests the presence of star-to-star iron variations for star with lower metallicities. It is not clear whether this tail indicates an intrinsic spread in iron or is due to a distinct group of star poorly resolved by observational errors.

NaO anticorrelation

Sodium as a function of oxygen is shown in Fig. 4.4 for the entire GIRAFFE sample while in Fig.4.5 we show the Na-O anticorrelation for $\sim$2000 stars belonging to nineteen GCs from Carretta et al. (2009).

We note that in ω Cen, apparently, there is no clear NaO anticorrelation as found in GCs.

To further investigate the chemical properties of ω Cen stars, in the following, we isolated five stellar groups with almost the same metallicity, that we selected on the basis of both their measured [Fe/H] abundance, and the position on the CMD.

We started by selecting stars on the iron distribution of Fig. 4.2, and then, to minimize the contamination from other populations, we looked at the position of these stars on the CMD and eliminate the ones (few stars for each population) lying outside the RGB section defined by the bulk of stars. The position on the CMD of these selected groups are represented in the lower panels of Fig.4.6. For simplicity we refer to these groups by using the following names:

- RGB-MP group with a mean iron of ~ -1.80, represented in the most

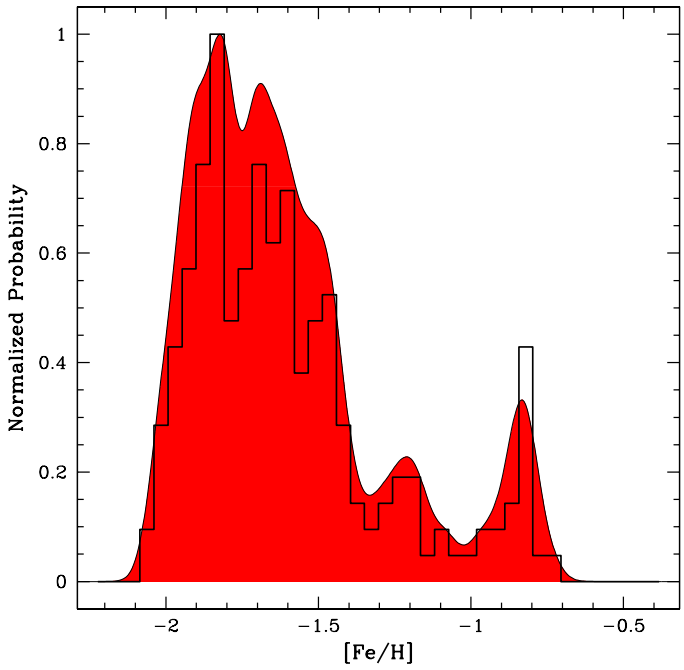

FIGURE 4.2— Histogram of the [Fe/H] contents obtained from GIRAFFE archive data. The Kernel density distribution has been superimposed to the histogram.

left lower panel of Fig.4.6;

- RGB-Int1 group with a mean iron of ~ -1.65 (red symbols in the second lower panel of Fig.4.6);
- RGB-Int2 group with a mean iron of ~ -1.5 (red symbols in the third lower panel of Fig.4.6);
- RGB-unk group with a mean iron of ~ -1.2 (green symbols in the right lower panel of Fig.4.6);
- RGB-a group with a mean iron of ~ -0.85 (red symbols in the right lower panel of Fig.4.6);

For these working groups, we studied the chemical abundances of the critical elements Na, O, and s elements.

However, when we consider our simple selection of the different stellar groups, as shown in Fig. 4.6, we found that the NaO anticorrelation is clearly

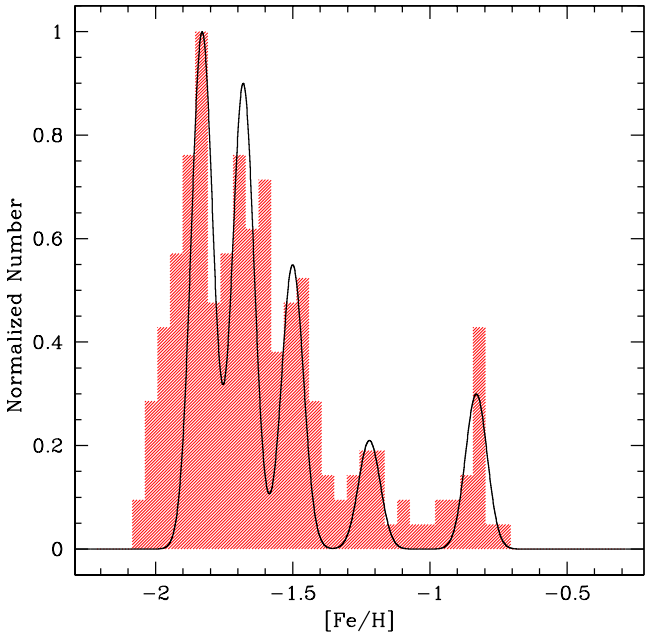

FIGURE 4.3— The same histogram of Fig.4.2 is represented, with superimposed the simulated distribution expected for five distinct stellar groups with the observed discrete metallicity values.

present in some metallicity ranges.

In the lower panels of Fig. 4.6, the position on the CMD for the different selected groups is shown, with the corresponding NaO anticorrelation in each upper panel. We note that the NaO anticorrelation is well observed for the stars belonging to the Int1 and Int2 populations, and some hints of a probably less extended one are also present for the MP population. Apparently, the anticorrelation disappears for the most metal rich populations RGB-unk and RGB-a. The RGB-unk population shows a very high Na enrichment with [Na/Fe]$\sim$1 dex, while its oxygen is quite spread ranging from [O/Fe]~-0.5 to [O/Fe]$\sim$0.7. Interestingly, no stars in the others GCs populate this region of the Na-O plane as shown in the Fig. 4.5. A similar range in O seems to be present also in RGB-a stars, even if they also show large variations in Na. For comparison, we over-imposed to each Na-O plane, a fiducial traced by hand on the NaO anticorrelation for stars with $-1.80<$[Fe/H]< -1.34.

It is important to remark here, that, possibly, there are overlaps between

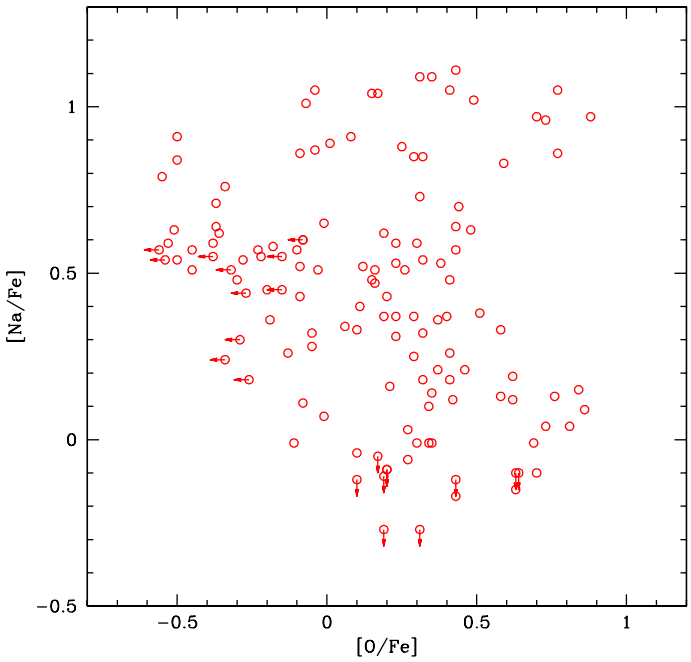

FIGURE 4.4— [Na/Fe] as a function of [O/Fe] for the GIRAFFE archive sample.

the various groups of stars due to our selection, however the RGB-a group is quite clustered in Fe abundances, and also define a clear sequence on the RGB. Johnson et al. (2009) found that, at [Fe/H]> -1.2, the 95% of stars are very Na rich, in agreement with Norris & Da Costa (1995) who found that at least 75% of stars in the same metallicity range are Na-rich and at least 50% are O-poor. Our findings also agrees with these previous results, nevertheless here we attempted to distinguish two populations in this metallicity range.

Noteworthy, the lowest value of Na of the anticorrelation grows with iron, from the left to the right panels. The pattern of Na abundances with Fe is represented in the left panel of Fig.4.7, where clearly we see, besides the general correlation with iron, that almost in all the metallicity intervals, [Na/Fe] ranges over large spread values. The increase of [Na/Fe] as a function of iron was also found by Johnson et al. (2009). The ranges of variation of Na and O are also in agreement with the study by Norris & Da Costa (1995), based on 40 stars observed at a resolution of R$\sim$38,000.

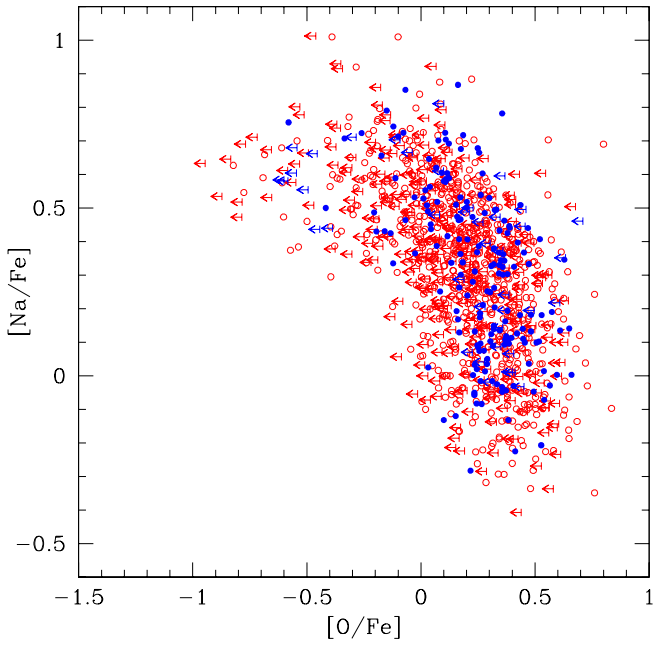

FIGURE 4.5— NaO anticorrelation for ∼2000 RGB stars in 19 GCs from Carretta et al. (2009). Red and blue symbols indicate the GIRAFFE and UVES measures respectively.

s-elements

We analyzed the s element abundances of La and Ba. Their abundances as a function of [Fe/H] are shown in Fig.4.8. We find a clear correlation between s elements and Fe. The increasing of s elements with iron seems to saturate at higher [Fe/H] ($\gtrsim -1.3$). As previously noted by other studies (e.g., Francois et al. 1988; Norris & Da Costa 1995; Smith et al. 1995, 2000, Johnson et al. 2009), the most of ω Centauri stars are strongly s enhanced. Some stars, because of their extremely high abundances of [Ba/Fe] and [La/Fe], may be Ba stars.

As done for the NaO anticorrelation, we attempted to study the s element abundances in the different populations of ω Centauri, together with the Na abundances. In Fig.4.10 there are the same NaO anticorrelations represented in Fig.4.6 for our selected groups of stars. In each panel we divided the stars on the basis of their position on the Na-O plane. In upper panels it is reported the position of the stars on the Ba-La plane of the corresponding lower panel: for each population the stars with lower Na content have generally lower s element abundances, this trend is particularly evident for the RGB-Int1 stars. This

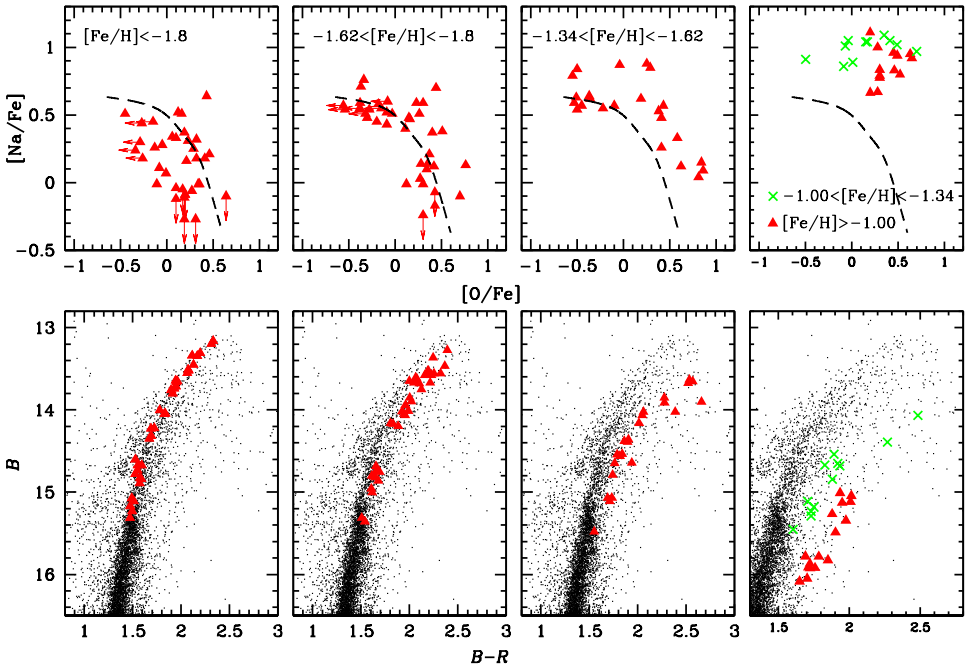

FIGURE 4.6— *Lower panels*: B vs.$(B\text{-}R)$ CMD from WFI photometry. In each panel we selected (in red and green) stars in the quoted metallicity range. *Upper panels*: Na-O anticorrelation for the stars of each population. A fiducial, traced by hand on the NaO anticorrelation for stars with $-1.80<$[Fe/H]<-1.34, has been over-imposed to each Na-O plane.

behavior recalls the case of NGC 1851, a GC hosting two stellar populations inferred from the presence of a split SGB. Spectroscopic studies demonstrated that the stellar generation associated to the bright SGB is made up by Na-poor, O-rich, s-elements poor stars, while stars in the faint SGB are Na-rich, O-poor, s-elements rich.

4.3.2 Chemical abundances for the UVES sample

From the analysis of the UVES spectra we obtained that the [Fe/H] ranges from ~ -2.0 to ~ -0.6 dex, in agreement with previous results. In Fig.4.11 we represent the position of the UVES sample on the CMD, with grey scale proportional to the iron abundances. From UVES data we also analyzed the abundances of Na, O, Al, Mg, Ba, Y, Zr.

In Fig.4.12 we plot the elements involved in the known anticorrelations. From the analysis of this sample of stars we found a well extended NaO anticorrelation (upper-left panel), like found in all the *normal* GCs, and also a

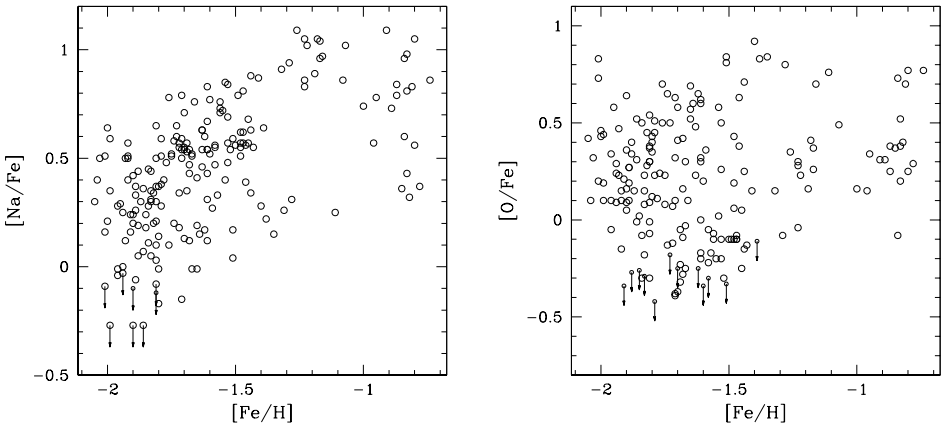

FIGURE 4.7— [Na/Fe] and [O/Fe] as a function of [Fe/H] obtained from GIRAFFE.

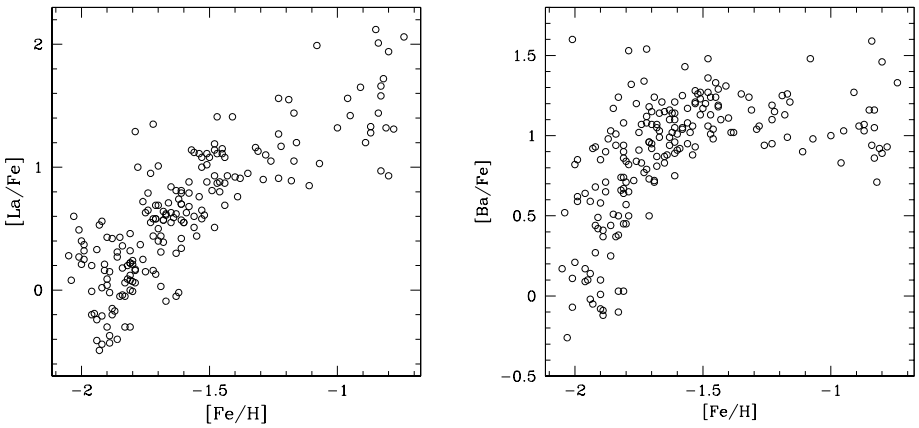

FIGURE 4.8— [La/Fe] and [Ba/Fe] as a function of [Fe/H] obtained from GIRAFFE.

clear MgAl anticorrelation (upper-right panel), found in some GCs. In the lower panels we also show that Al correlates with Na, and Mg with Al. UVES results on NaO anticorrelation are in agreement with the GIRAFFE ones. The complicate NaO anticorrelation found from the GIRAFFE sample, not observed for UVES, simply is due to the larger sample of GIRAFFE targets that allows us to observe a statistically consistent number of stars in each population.

As shown in Fig.4.13, sodium abundances grow with iron with the exception

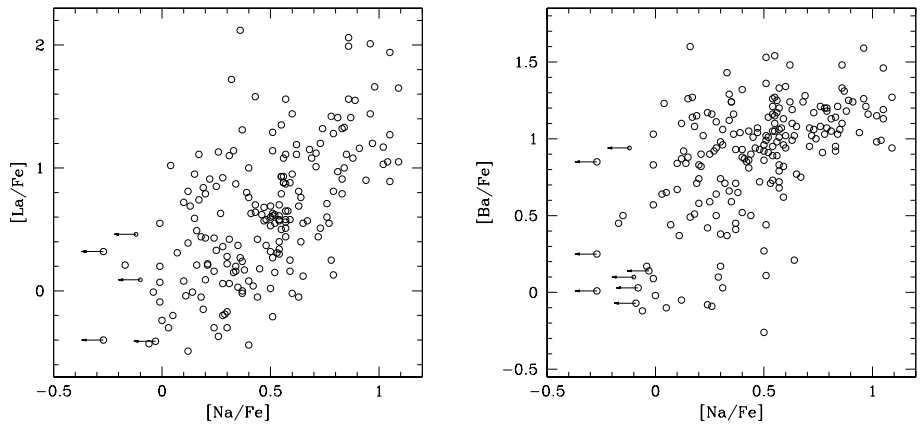

FIGURE 4.9— [La/Fe] and [Ba/Fe] as a function of [Na/Fe] obtained from GIRAFFE.

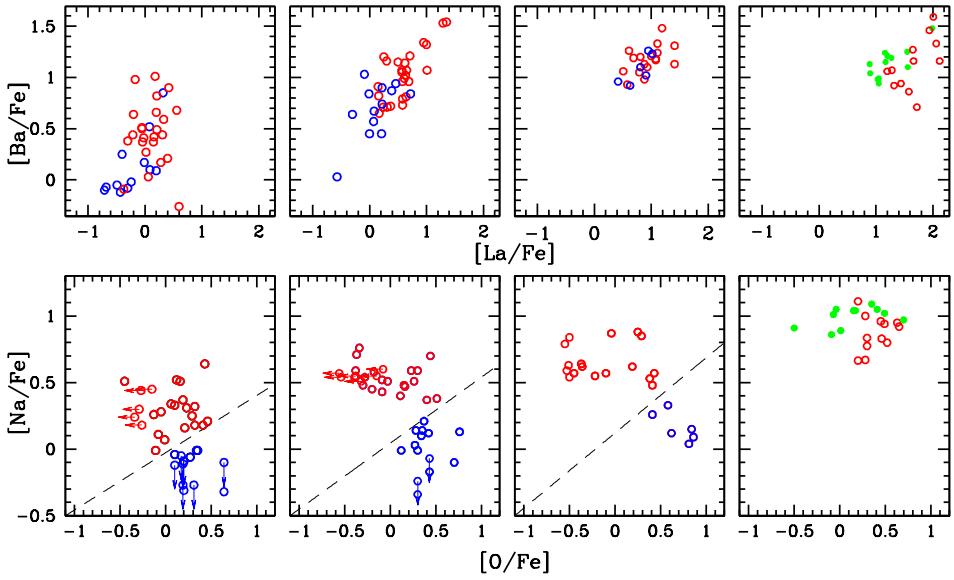

FIGURE 4.10— *Lower panels*: Na-O anticorrelations for the stars selected in Fig.4.6. The dashed line in each panel defines two subsample of Na-rich and Na-poor stars. *Upper panels*: Ba as a function of La for the stars of each group.

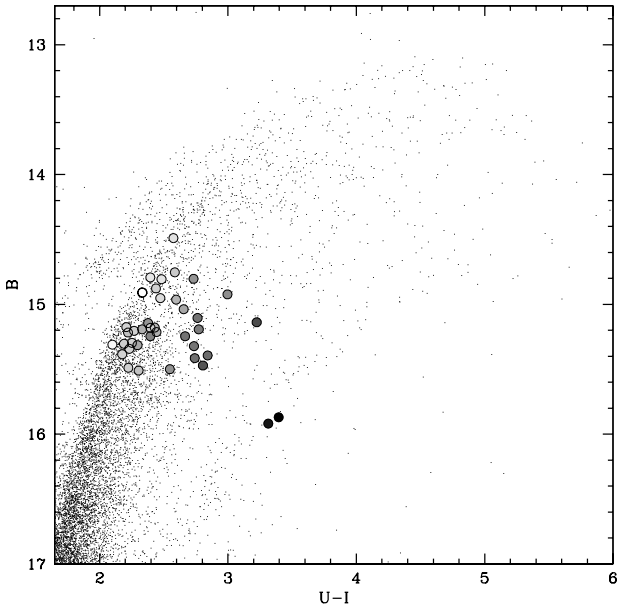

FIGURE 4.11— As in Fig.4.1 for the UVES sample.

of the two Fe richest stars. Also Al seems to show a trend with iron with the metal poorer stars spanning a large range of abundances from ∼0.1 to ∼1.0 dex, the metal intermediate stars have all high Al abundances ([Al/Fe]≥1.0). The two metal richest stars have [Al/Fe] around 0.5 dex. More complex is the relation between oxygen and magnesium with iron (as shown in the lower panels of Fig.4.13), however it seems that these two elements follow a similar behavior with [Fe/H].

The s elements Y, Zr and Ba well correlate with [Fe/H] as shown in Fig.4.14, reaching high values as also found in previous studies (see Johnson et al. 2009).

4.3.3 Summary

By analyzing a sample of 40 RGB at high resolution with UVES and a sample of ∼200 stars with GIRAFFE we found a spread in iron for ω Centauri that ranges from ~ -2.1 to ~ -0.7. The metallicity distribution peaks to the five values ~ -1.82, ~ -1.65, ~ -1.50, ~ -1.20, and ~ -0.85.

We are not able to discriminate whether ω Cen stars are clustered around

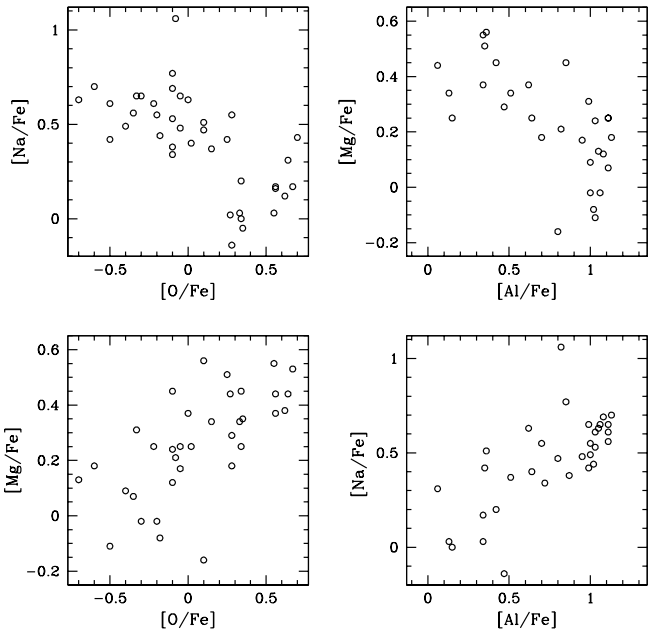

FIGURE 4.12— In upper panels the NaO anticorrelation (left panel), and MgAl anticorrelation (right panel) obtained from UVES are represented. In lower panels we also show that Al correlates with Na, and Mg with Al.

discrete [Fe/H] values or present a nearly continuous distribution. From the comparison of observed iron distribution and the simulated one we found that, if this GC has experienced discrete episodes of star formation (as opposite of a prolonged star formation), it should hosts more than five distinct stellar groups.

From our analysis, it appears that the classification of the populations in ω Cen on the basis of only their iron content alone reflects only an aspect of its complex stellar population system.

We represent the Na and O abundances for the five groups of stars in ω Cen, selected on the basis of different iron content and their position on the CMD. We found that the NaO anticorrelation is well defined for the stars belonging to the metal intermediate populations, and some hints of a probably less extended one are present for the more metal poor stars. Apparently, the anticorrelation disappears for the most metal rich populations. We note that the Na level grows with iron.

From the analysis of the s elements La and Ba we derive that the s element abundance grows with increasing iron, and interestingly enough, in each group

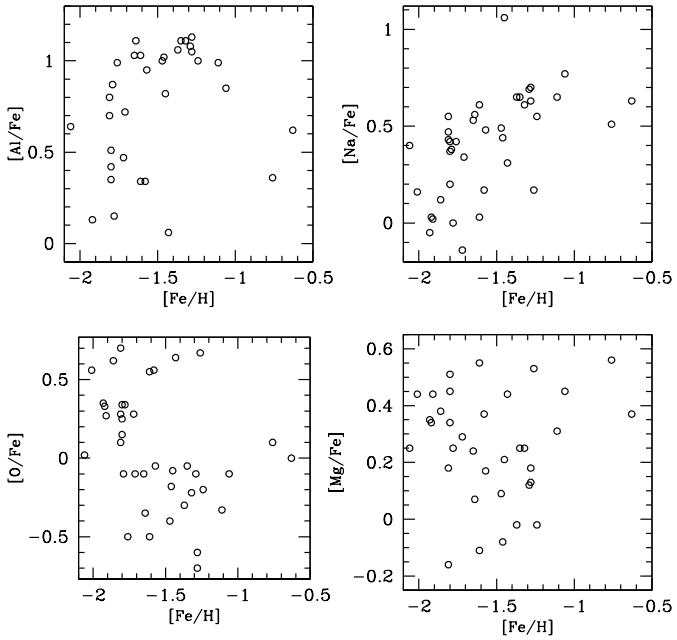

FIGURE 4.13— [Na/Fe] and [Al/Fe] (upper panels) and [Mg/Fe] and [O/Fe] (lower panels) are represented as a function of [Fe/H] for the UVES sample.

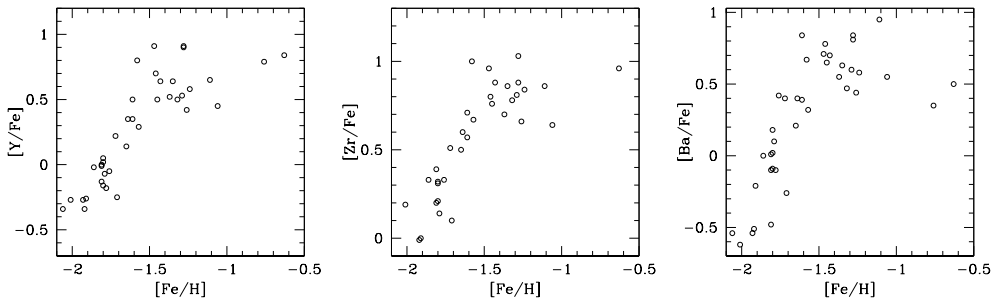

FIGURE 4.14— s elements [Y/Fe], [Zr/Fe], and [Ba/Fe] as a function of [Fe/H] obtained from UVES.

defined as in Fig.1.1, s elements apparently increase with Na. Such behavior of s-elements and Na-O anticorreletion strongly resembles the less complex case of M22.

5

Conclusions

In this thesis I presented spectroscopic results for the three GCs M4, M22 and ω Centauri.

The most relevant result for M4 is that this globular hosts two stellar populations with a different content of Na, O, and CN. These two groups of stars define two RGB sequences when the magnitude U, strongly affected by CN bands, is used. The broadening of the RGB in the CMD $(U - B)$-U is due to chemical variations in the CN molecular bands, and it is visible from the base to the tip of the RGB, indicating that the abundance differences must be primordial. No indications for intrinsic variations in heavy elements were found.

In M22, similarly to the other GCs, there are variations in light elements that define the classical patterns of the NaO anticorrelation and NaAl correlarrelation. The most surprising finding is that M22 also shows intrinsic differences in iron of $\sim$0.14 dex. This makes M22 similar to ω Centauri, that was always considered as the only GC with a spread in iron, and M54, where spectroscopic evidence for iron variations were recently found by Carretta et al. (submitted to ApJL). Moreover, iron differences in M22 correspond to a variation in calcium and to a bimodality in s-process elements (as Y, Zr, Ba, and La). Stars with higher Fe and Ca have also higher s abundances (s-rich group), and stars with lower Fe and Ca show a lower content of s elements (s-poor group). The main result of this study is that two stellar populations characterized by different iron, and s elements are hosted in this cluster. These two groups define two RGB sequences in the CMD obtained by using the Strömgren index m_1, sensitive to the CN molecular bands, suggesting that they have also a different CN abundance. However, the two s groups do not show evidence for a difference

in Na and O: both have the NaO anticorrelation, but the Na range is different, with the s rich stars having its NaO anticorrelation starting at a higher Na level. The populations might be related to the bimodal distribution of the SGB stars revealed by HST photometry, that could be due to differences in the total CNO abundances, as suggested by Cassisi et al. (2008) and Ventura et al. (2009) for the similar case of the SGB split in NGC1851. It is worth noting that also in NGC1851 two groups of stars with different s element abundances have been found by Yong et al. (2008) from the analysis of eight RGBs, but, differently from M22, in that case s elements correlate with Na, although their low statistic prevent us from firm conclusions.

Omega Centauri is the most puzzling case of GC with multiple populations. Despite iron intrinsic variations have been detected also in M22, ω Centauri have a much larger spread. From this study it results that the NaO anticorrelation is present among the metal poor and metal intermediate populations, and apparently disappears for the iron richer stars. Similarly to the case of M22, the Na level of the NaO anticorrelation grows with [Fe/H]. s elements increase with iron reaching high abundance values. Evidence for a variation in s elements inside each population with a given iron are also present, with the s abundance increasing with higher Na.

The complex chemical patterns and the large variations in chemical abundances in ω Centauri make difficult to think that it is a real GC. It has been suggested (Bekki & Norris 2006) that it could be the remnant of a larger system, for example a dwarf galaxy. However, results presented in this thesis show that GCs, in general, are not as simple systems as thought in the past. All the three studied cases show evidence of multiple populations, but they reveal themselves in different ways. The main results for the three analyzed GCs are compared in Fig.5.1. The [Fe/H] distribution peaks around one single value in the case of M4 (top left panel), is bimodal for M22 (middle left panel), and more complex with multiple peaks in ω Centauri (bottom left panel). s elements do not seem to vary in M4 (top middle panel), double-peak with iron in M22 (middle panel), and show a much larger range, with a general increase with iron, in ω Centauri. The NaO anticorrelation is present in all the three GCs, and, as previously said, in M22 and ω Centauri, that have populations with different abundances in heavy elements, the Na level of the NaO anticorrelation increases with iron.

The differences among these three clusters indicate that they have experienced different enrichment histories.

In the case of M22 and ω Centauri the iron enrichment indicate a pollution by Core Collapse Supernovae Supernovae Type II (SNeII). ω Centauri, with a mass of M$\sim 3\times10^6$M$_\odot$; is the most massive GC in our Galaxy, and M22 (M $> 10^5$M$_\odot$) among the most massive. In spite of this, their mass is not

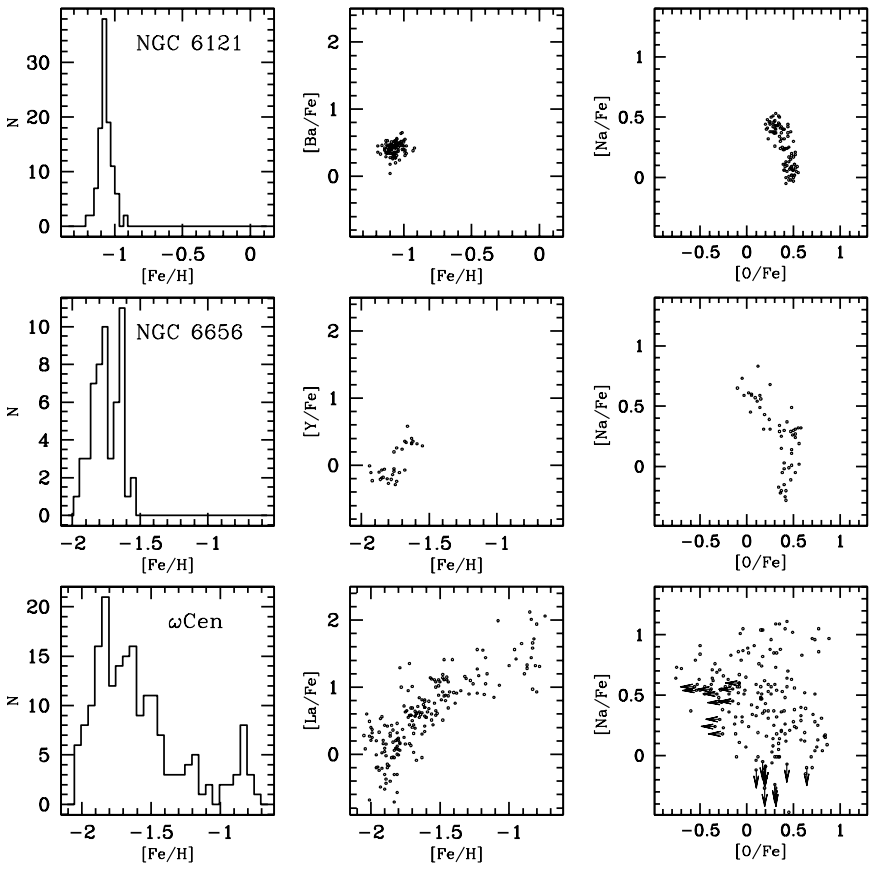

FIGURE 5.1— From the left to the right: [Fe/H] distribution, s element abundances, and NaO anticorrelation obtained for M4 (top panels), M22 (middle panels), and ω Centauri (lower panels).

enough to retain the high velocity SNeII ejecta within the shallow gravitational well of a GC, suggesting that they could have been much more massive in the past. Besides the SNeII enrichment, a further enrichment of the intracluster medium interests stars with the same iron content in ω Centauri and M22, and is responsible for the observed NaO anticorrelations.

Today, it is generally accepted that the chemical anticorrelations are due to the fact that a fraction of stars in GCs formed from matter that has been

polluted with the yields of a previous stellar generation, the debate about the kind of stars responsible for this pollution is still open. If the polluting matter is identified with the envelopes of asymptotic giant branch stars (Ventura et al. 2001, 2002), these AGB stars should be very massive in order to experience the second dredge-up, which brings a large amount of fresh He to the envelope, and the hot bottom burning process, which converts C into N. Such massive AGB stars should not live long enough, however, for a sufficient number of them to experience a third dredge-up and significantly increase the total C+N+O abundance in the envelope (Renzini 2008). As an alternative, polluted material could come from the envelopes of fast-rotating stars during the H-burning phase; in this case we expect a He-enriched second generation without any C+N+O enhancement at all (Decressin et al. 2007).

Hence, the pollution from massive AGB, or fast-rotating stars can account for the observed NaO anticorrelations, and also for He enrichment in GCs like ω Centauri (Piotto et al. 2005), NGC2808 (D'Antona et al. 2005; Piotto et al. 2007), and NGC6752 (Milone et al. 2009). Pollution from AGB stars that have experienced the third dredge-up, can account also for possible variations in the total CNO abundances that have been proposed to explain the SGB split in NGC1851. Additionally, material ejected from these stars should be enriched also in s elements, as observed in M22 and NGC1851.

In any case, the presence of multiple populations in less massive GCs, like M4, makes the multipopulation phenomenon even more complicated than originally thought. It becomes harder and harder to accept that the phenomenon can be totally internal to the cluster, unless GCs are the remnant of much larger systems, probably the nucleus of a dwarf galaxy, idea that has important consequences for cosmological theories.

At this stage, observational insight into such processes could come from further and detailed spectroscopic analysis. A study of the overall C+N+O and relations with Fe, α and s-elements in GCs with a split SGB, will give important information on the complex star formation in GCs, and the nature of the stars that polluted the medium from which the second generation was born. An interesting target for these studies is M22. The surprising spectroscopic and photometric findings have shown that this object could be the link between *normal* GCs and more massive objects like ω Centauri and even dwarf galaxies. A detailed study of chemical abundances in this cluster, mainly the measure of the overall C+N+O content in its stellar subpopulations, is mandatory to understand the nature of M22.

A

Linelist

In this appendix I report the linelist (Tab.A.1) used for the chemical abundances obtained from equivalent widths. This linelist was obtained from the VALD database (Kupka et al. 1999) and calibrated using the Solar-inverse technique. For this purpose we used the high resolution, high S/N Solar spectrum obtained at NOAO (*National Optical Astronomy Observatory*, Kurucz et al. 1984). We used the model atmosphere interpolated from the Kurucz (1992) grid using the canonical atmospheric parameters for the Sun: $T_{eff} = 5777$ K, log(g) = 4.44, $v_t = 0.80$ km/s and [Fe/H] = 0.00. The EWs for the reference Solar spectrum were obtained in the same way as the observed spectra, with the exception of the strongest lines, where a Voigt profile integration was used.

Table A.1: Linelist: wavelengths, excitation potentials (E.P.), and the loggf for spectral lines.

Wavelength [Å]	Element	E.P. [eV]	loggf
4754.039	25.0	2.280	0.020
4758.124	22.0	2.250	0.370
4759.276	22.0	2.250	0.460
4761.528	25.0	2.950	−0.330
4762.782	22.1	1.080	−2.870
4767.857	24.0	3.560	−0.540
4768.082	27.0	3.180	−0.740
4773.959	58.1	0.920	0.240
4778.258	22.0	2.240	−0.360
4789.342	24.0	2.540	−0.380
4792.862	27.0	3.240	−0.030

Table A.1: continued.

Wavelength [Å]	Element	E.P. [eV]	loggf
4798.537	22.1	1.080	−2.650
4801.031	24.0	3.120	−0.140
4810.537	30.0	4.080	−0.080
4812.352	24.1	3.860	−1.740
4813.479	27.0	3.200	0.220
4820.414	22.0	1.500	−0.380
4827.457	23.0	0.040	−1.520
4831.651	23.0	0.020	−1.360
4832.431	23.0	0.000	−1.630
4836.857	24.0	3.100	−1.020
4848.252	24.1	3.860	−1.220
4854.873	39.1	0.990	−0.420
4856.195	24.1	3.850	−2.250
4864.738	23.0	0.020	−1.110
4865.618	22.1	1.120	−2.810
4867.874	27.0	3.100	0.350
4874.014	22.1	3.090	−0.900
4875.492	23.0	0.040	−0.730
4883.440	23.1	3.790	−0.320
4883.690	39.1	1.080	0.040
4884.598	24.1	3.860	−2.080
4900.124	39.1	1.030	0.120
4904.420	28.0	3.540	−0.170
4911.199	22.1	3.120	−0.520
4913.978	28.0	3.740	−0.580
4935.834	28.0	3.940	−0.250
4936.341	24.0	3.110	−0.270
4953.212	28.0	3.740	−0.570
4954.809	24.0	3.120	−0.130
4964.933	24.0	0.940	−2.530
4967.523	28.0	3.800	−1.580
4981.740	22.0	0.850	0.470
4982.136	39.1	1.030	−1.440
4995.659	28.0	3.630	−1.630
4997.100	22.0	0.000	−2.120
4999.510	22.0	0.830	0.240
5001.472	20.1	7.500	−0.480

Table A.1: continued.

Wavelength [Å]	Element	E.P. [eV]	loggf
5003.747	28.0	1.680	−3.120
5004.894	25.0	2.920	−1.870
5005.171	22.1	1.570	−2.660
5009.655	22.0	0.020	−2.340
5010.943	28.0	3.630	−0.920
5016.168	22.0	0.850	−0.560
5022.874	22.0	0.830	−0.310
5039.964	22.0	0.020	−1.230
5048.853	28.0	3.850	−0.340
5062.104	22.0	2.160	−0.440
5069.088	22.1	3.120	−1.500
5072.298	22.1	3.120	−0.970
5087.426	39.1	1.080	−0.220
5094.418	28.0	3.830	−1.110
5105.545	29.0	1.380	−0.880
5112.279	40.1	1.660	−0.590
5113.447	22.0	1.440	−0.820
5123.006	57.1	0.320	−0.930
5145.468	22.0	1.460	−0.590
5147.482	22.0	0.000	−2.020
5148.846	11.0	2.100	−2.110
5152.190	22.0	0.020	−2.040
5157.984	28.0	3.510	−1.750
5173.750	22.0	0.000	−1.370
5185.908	22.1	1.890	−1.530
5193.502	24.0	3.420	−0.890
5197.170	28.0	3.900	−1.140
5200.185	24.0	3.380	−0.550
5200.415	39.1	0.990	−0.610
5205.730	39.1	1.030	−0.250
5210.392	22.0	0.050	−0.900
5212.691	27.0	3.510	−0.100
5214.130	24.0	3.370	−0.720
5214.616	24.0	3.320	−0.580
5218.209	29.0	3.800	0.320
5219.706	22.0	0.020	−2.240
5220.086	29.0	3.800	−0.590

Table A.1: continued.

Wavelength [Å]	Element	E.P. [eV]	loggf
5237.325	24.1	4.070	−1.150
5238.969	24.0	2.710	−1.390
5239.823	21.1	1.450	−0.620
5246.777	24.1	3.710	−2.520
5247.574	24.0	0.960	−1.550
5255.325	25.0	3.310	−0.930
5260.390	20.0	2.520	−1.830
5261.708	20.0	2.520	−0.410
5272.003	24.0	3.450	−0.490
5274.236	58.1	1.040	0.240
5279.877	24.1	4.070	−2.040
5280.633	27.0	3.630	−0.070
5282.443	22.0	1.050	−1.330
5295.784	22.0	1.050	−1.670
5296.702	24.0	0.980	−1.350
5299.984	22.0	1.050	−1.410
5300.751	24.0	0.980	−2.090
5304.185	24.0	3.460	−0.710
5305.866	24.1	3.830	−1.930
5308.429	24.1	4.070	−1.820
5310.697	24.1	4.070	−2.310
5312.863	24.0	3.450	−0.620
5313.585	24.1	4.070	−1.660
5318.361	21.1	1.360	−1.750
5318.776	24.0	3.440	−0.720
5319.820	60.1	0.550	−0.560
5336.790	22.1	1.580	−1.490
5340.454	24.0	3.440	−0.770
5342.708	27.0	4.020	0.630
5345.807	24.0	1.000	−1.040
5348.326	24.0	1.000	−1.210
5349.469	20.0	2.710	−0.470
5352.049	27.0	3.560	−0.020
5392.330	28.0	4.150	−1.360
5402.783	39.1	1.840	−0.600
5409.799	24.0	1.030	−0.700
5418.780	22.1	1.580	−2.050

Table A.1: continued.

Wavelength [Å]	Element	E.P. [eV]	loggf
5420.929	24.1	3.760	−2.290
5432.548	25.0	0.000	−3.940
5468.114	28.0	3.850	−1.660
5490.159	22.0	1.460	−0.950
5494.474	26.0	4.070	−1.970
5502.092	24.1	4.170	−1.950
5503.904	22.0	2.580	−0.130
5508.633	24.1	4.150	−2.020
5522.454	26.0	4.210	−1.450
5524.244	26.0	4.150	−2.870
5525.135	26.1	3.270	−4.070
5526.821	21.1	1.770	0.180
5534.848	26.1	3.240	−2.780
5539.291	26.0	3.640	−2.560
5547.000	26.0	4.220	−1.770
5552.687	26.0	4.950	−1.780
5560.220	26.0	4.430	−1.070
5568.862	26.0	3.630	−2.980
5577.028	26.0	5.030	−1.560
5578.729	28.0	1.680	−2.670
5587.581	26.0	4.140	−1.710
5587.868	28.0	1.930	−2.430
5589.366	28.0	3.900	−1.160
5590.126	20.0	2.510	−0.680
5593.746	28.0	3.900	−0.830
5595.051	26.0	5.060	−1.720
5608.976	26.0	4.210	−2.360
5609.965	26.0	3.640	−3.260
5611.357	26.0	3.630	−2.920
5618.642	26.0	4.210	−1.300
5619.609	26.0	4.390	−1.480
5627.642	23.0	1.080	−0.260
5628.650	24.0	3.420	−0.790
5635.831	26.0	4.260	−1.590
5636.705	26.0	3.640	−2.530
5640.989	21.1	1.500	−0.880
5643.087	28.0	4.160	−1.270

Table A.1: continued.

Wavelength [Å]	Element	E.P. [eV]	loggf
5645.618	14.0	4.930	−2.070
5647.241	27.0	2.280	−1.560
5649.996	26.0	5.100	−0.770
5651.477	26.0	4.470	−1.800
5652.327	26.0	4.260	−1.780
5657.880	21.1	1.510	−0.280
5658.346	21.1	1.500	−1.030
5661.017	26.0	4.580	−2.480
5661.354	26.0	4.280	−1.870
5662.159	22.0	2.320	−0.150
5665.563	14.0	4.920	−2.040
5667.153	21.1	1.500	−1.110
5669.040	21.1	1.500	−1.030
5670.858	23.0	1.080	−0.390
5671.826	21.0	1.450	0.560
5677.689	26.0	4.100	−2.660
5678.388	26.0	3.880	−2.960
5680.244	26.0	4.190	−2.360
5682.647	11.0	2.100	−0.770
5684.198	21.1	1.510	−0.960
5684.493	14.0	4.950	−1.760
5688.217	11.0	2.100	−0.500
5690.433	14.0	4.930	−1.860
5698.530	23.0	1.060	0.050
5701.108	14.0	4.930	−2.110
5701.557	26.0	2.560	−2.100
5702.328	24.0	3.450	−0.390
5703.587	23.0	1.050	−0.140
5708.405	14.0	4.950	−1.590
5711.095	12.0	4.340	−1.650
5717.841	26.0	4.280	−0.900
5727.057	23.0	1.080	0.090
5731.772	26.0	4.260	−0.970
5738.240	26.0	4.220	−2.230
5741.856	26.0	4.260	−1.660
5742.963	26.0	4.180	−2.340
5748.361	28.0	1.680	−3.300

Table A.1: continued.

Wavelength [Å]	Element	E.P. [eV]	loggf
5752.042	26.0	4.550	−0.920
5759.259	26.0	4.650	−2.040
5760.359	26.0	3.640	−2.480
5760.841	28.0	4.100	−0.830
5772.149	14.0	5.080	−1.700
5775.088	26.0	4.220	−1.110
5778.463	26.0	2.590	−3.510
5781.187	24.0	3.320	−0.840
5781.759	24.0	3.320	−0.710
5783.073	24.0	3.320	−0.450
5783.866	24.0	3.320	−0.200
5784.666	26.0	3.400	−2.610
5784.976	24.0	3.320	−0.440
5787.926	24.0	3.320	−0.070
5793.079	14.0	4.930	−1.940
5793.922	26.0	4.220	−1.600
5797.865	14.0	4.950	−2.040
5805.226	28.0	4.170	−0.630
5806.732	26.0	4.610	−0.840
5811.912	26.0	4.140	−2.390
5814.815	26.0	4.280	−1.860
5835.109	26.0	4.260	−2.170
5837.702	26.0	4.290	−2.320
5847.006	28.0	1.680	−3.450
5849.687	26.0	3.690	−2.960
5852.228	26.0	4.550	−1.130
5853.150	26.0	1.480	−5.160
5853.688	56.1	0.600	−1.020
5855.086	26.0	4.610	−1.570
5856.096	26.0	4.290	−1.570
5858.785	26.0	4.220	−2.210
5859.596	26.0	4.550	−0.590
5861.110	26.0	4.280	−2.380
5862.368	26.0	4.550	−0.410
5866.461	22.0	1.070	−0.780
5867.572	20.0	2.930	−1.620
5880.025	26.0	4.560	−1.940

Table A.1: continued.

Wavelength [Å]	Element	E.P. [eV]	loggf
5881.279	26.0	4.610	−1.780
5902.476	26.0	4.590	−1.810
5905.680	26.0	4.650	−0.690
5922.123	22.0	1.050	−1.450
5927.797	26.0	4.650	−1.040
5929.682	26.0	4.550	−1.130
5930.191	26.0	4.650	−0.240
5934.665	26.0	3.930	−1.100
5947.531	26.0	4.610	−2.060
5948.548	14.0	5.080	−1.160
5956.706	26.0	0.860	−4.540
5978.549	22.0	1.870	−0.530
5984.826	26.0	4.730	−0.350
5991.378	26.1	3.150	−3.470
5996.740	28.0	4.230	−1.040
6003.022	26.0	3.880	−1.030
6007.968	26.0	4.650	−0.850
6008.566	26.0	3.880	−0.860
6013.497	25.0	3.070	−0.090
6016.647	25.0	3.070	0.070
6019.369	26.0	3.570	−3.310
6021.803	25.0	3.080	0.110
6027.059	26.0	4.070	−1.220
6053.693	28.0	4.230	−1.080
6056.013	26.0	4.730	−0.390
6065.494	26.0	2.610	−1.540
6078.499	26.0	4.790	−0.380
6079.016	26.0	4.650	−0.940
6081.448	23.0	1.050	−0.620
6082.718	26.0	2.220	−3.550
6084.105	26.1	3.200	−3.820
6086.288	28.0	4.260	−0.420
6089.574	26.0	5.020	−0.900
6090.216	23.0	1.080	−0.070
6091.177	22.0	2.270	−0.430
6093.649	26.0	4.610	−1.360
6094.377	26.0	4.650	−1.620

Table A.1: continued.

Wavelength [Å]	Element	E.P. [eV]	loggf
6096.671	26.0	3.980	−1.790
6098.250	26.0	4.560	−1.800
6108.125	28.0	1.680	−2.470
6111.078	28.0	4.090	−0.790
6113.329	26.1	3.210	−4.180
6119.532	23.0	1.060	−0.370
6120.258	26.0	0.910	−5.910
6125.026	14.0	5.610	−1.580
6126.224	22.0	1.070	−1.370
6128.984	28.0	1.680	−3.360
6130.141	28.0	4.260	−0.990
6137.002	26.0	2.200	−2.880
6145.020	14.0	5.610	−1.510
6149.249	26.1	3.890	−2.740
6151.623	26.0	2.180	−3.280
6154.230	11.0	2.100	−1.590
6157.733	26.0	4.070	−1.280
6160.753	11.0	2.100	−1.310
6161.295	20.0	2.520	−1.390
6163.754	20.0	2.520	−1.330
6165.363	26.0	4.140	−1.490
6166.440	20.0	2.520	−1.160
6169.044	20.0	2.520	−0.760
6169.564	20.0	2.520	−0.670
6173.341	26.0	2.220	−2.870
6176.816	28.0	4.090	−0.220
6177.253	28.0	1.830	−3.590
6186.717	28.0	4.100	−0.920
6187.402	26.0	2.830	−4.170
6187.995	26.0	3.940	−1.610
6199.186	23.0	0.290	−1.420
6199.509	26.0	2.560	−4.390
6200.321	26.0	2.610	−2.310
6204.610	28.0	4.090	−1.140
6213.437	26.0	2.220	−2.490
6216.358	23.0	0.280	−0.820
6219.287	26.0	2.200	−2.360

Table A.1: continued.

Wavelength [Å]	Element	E.P. [eV]	loggf
6220.791	26.0	3.880	−2.380
6223.990	28.0	4.100	−0.930
6226.740	26.0	3.880	−2.070
6230.098	28.0	4.100	−1.240
6232.648	26.0	3.650	−1.040
6239.948	26.1	3.890	−3.510
6240.653	26.0	2.220	−3.300
6243.114	23.0	0.300	−0.960
6245.620	21.1	1.510	−1.060
6246.327	26.0	3.600	−0.810
6247.562	26.1	3.870	−2.360
6251.825	23.0	0.290	−1.350
6252.565	26.0	2.400	−1.670
6258.110	22.0	1.440	−0.380
6261.106	22.0	1.430	−0.440
6265.141	26.0	2.180	−2.420
6270.231	26.0	2.860	−2.530
6279.740	21.1	1.500	−1.160
6280.622	26.0	0.860	−4.350
6297.799	26.0	2.220	−2.710
6301.508	26.0	3.650	−0.510
6303.466	26.0	4.320	−2.570
6311.504	26.0	2.830	−3.150
6315.814	26.0	4.070	−1.680
6318.708	12.0	5.110	−2.000
6319.242	12.0	5.110	−2.240
6322.169	28.0	4.150	−1.210
6322.694	26.0	2.590	−2.310
6327.604	28.0	1.680	−3.020
6330.096	24.0	0.940	−2.910
6330.852	26.0	4.730	−1.200
6335.337	26.0	2.200	−2.250
6347.095	14.1	8.120	0.250
6362.350	30.0	5.790	0.050
6369.463	26.1	2.890	−4.190
6371.355	14.1	8.120	−0.040
6378.256	28.0	4.150	−0.850

Table A.1: continued.

Wavelength [Å]	Element	E.P. [eV]	loggf
6380.750	26.0	4.190	−1.290
6383.715	26.1	5.550	−2.070
6384.668	28.0	4.150	−1.020
6392.538	26.0	2.280	−3.960
6393.612	26.0	2.430	−1.610
6411.658	26.0	3.650	−0.720
6416.928	26.1	3.890	−2.610
6432.683	26.1	2.890	−3.570
6436.411	26.0	4.190	−2.420
6439.083	20.0	2.520	0.300
6455.001	27.0	3.630	−0.280
6455.605	20.0	2.520	−1.380
6456.391	26.1	3.900	−2.030
6456.865	20.1	8.440	0.400
6471.668	20.0	2.520	−0.630
6481.878	26.0	2.280	−2.850
6482.809	28.0	1.930	−2.800
6493.788	20.0	2.520	−0.020
6496.908	56.1	0.600	−0.360
6498.945	26.0	0.960	−4.640
6499.654	20.0	2.520	−0.680
6516.083	26.1	2.890	−3.310
6518.373	26.0	2.830	−2.570
6532.881	28.0	1.930	−3.430
6533.940	26.0	4.560	−1.150
6554.238	22.0	1.440	−1.240
6572.795	20.0	0.000	−4.310
6574.254	26.0	0.990	−5.000
6581.218	26.0	1.480	−4.710
6586.319	28.0	1.950	−2.730
6591.314	26.0	4.590	−2.020
6593.884	26.0	2.430	−2.310
6598.611	28.0	4.230	−0.950
6604.600	21.1	1.360	−1.180
6606.979	22.1	2.060	−2.870
6608.044	26.0	2.280	−3.970
6609.118	26.0	2.560	−2.630

Table A.1: continued.

Wavelength [Å]	Element	E.P. [eV]	loggf
6625.039	26.0	1.010	−5.370
6627.560	26.0	4.550	−1.520
6633.758	26.0	4.560	−0.860
6635.137	28.0	4.420	−0.770
6667.426	26.0	2.450	−4.390
6667.723	26.0	4.580	−2.070
6696.032	13.0	3.140	−1.310
6698.669	13.0	3.140	−1.640
6699.142	26.0	4.590	−2.160
6703.576	26.0	2.760	−3.030
6704.485	26.0	4.220	−2.710
6713.745	26.0	4.790	−1.410
6725.364	26.0	4.100	−2.250
6726.673	26.0	4.610	−1.040
6733.153	26.0	4.640	−1.420
6739.524	26.0	1.560	−4.920
6745.965	26.0	4.070	−2.680
6750.164	26.0	2.420	−2.600
6753.465	26.0	4.560	−2.300
6757.195	16.0	7.870	−0.290
6767.784	28.0	1.830	−2.070
6772.321	28.0	3.660	−0.940
6786.860	26.0	4.190	−1.930
6793.260	26.0	4.070	−2.390
6796.120	26.0	4.140	−2.440
6804.297	26.0	4.580	−1.860
6806.856	26.0	2.730	−3.130
6810.267	26.0	4.610	−0.960
6814.961	27.0	1.960	−1.770

Bibliography

Alonso, A., Arribas, S., & Martinez-Roger, C. 1999, A&A, 140, 261

Alonso, A., Martinez-Roger, G., & Arribas, S. 2000, Liege International Astrophysical Colloquia, 35, 281

Anderson, J., Bedin, L. R., Piotto, G., Yadav, R. S., & Bellini, A. 2006, A&A, 454, 1029

Anderson, J., Piotto, G., King, I. R., Bedin, L. R., & Guhathakurta, P. 2009, ApJL, 697, L58

Ballester, P., Modigliani, A., Boitquin, O., et al. 2000, ESO Messenger, 101, 31

Bassino, L. P., & Muzzio, J. C. 1995, The Observatory, 115, 256

Bedin, L. R., Piotto, G., Zoccali, M., Stetson, P. B., Saviane, I., Cassisi, S., & Bono, G. 2000, A&A, 363, 159

Bedin, L. R., Anderson, J., King, I. R., & Piotto, G. 2001, ApJL, 560, L75

Bedin, L. R., Piotto, G., Anderson, J., Cassisi, S., King, I. R., Momany, Y., & Carraro, G. 2004, ApJ, 605, 125

Bekki, K., & Norris, J. E. 2006, ApJL, 637, L109

Bellazzini, M., et al. 2008, , 136, 1147

Bellini, A., et al. 2009, A&A, 493, 959

Blecha, A., Cayatte, V., North, P., Royer, F., & Simond, G. 2000, , 4008, 467

Brown, J. A., & Wallerstein, G. 1992, , 104, 1818

Busso, M., Gallino, R., Lambert, D. L., Travaglio, C., & Smith, V. V. 2001, ApJ, 557, 802

Busso, G., et al. 2007, A&A, 474, 105

Butler, D., Dickens, R. J., & Epps, E. 1978, ApJ, 225, 148

Caloi, V., & D'Antona, F. 2007, A&A, 463, 949

Cannon, R. D., & Stobie, R. S. 1973, MNRAS, 162, 207

Cannon, R. D., Croke, B. F. W., Bell, R. A., Hesser, J. E., & Stathakis, R. A. 1998, MNRAS, 298, 601

Carretta, E., Gratton, R. G., Bragaglia, A., Bonifacio, P., & Pasquini, L. 2004, A&A,

Carretta, E., Gratton, R. G., Lucatello, S., Bragaglia, A., & Bonifacio, P. 2005, A&A, 433, 597

Carretta, E., Bragaglia, A., Gratton, R. G., Leone, F., Recio-Blanco, A., & Lucatello, S. 2006, A&A, 450, 523

Carretta, E. et al., 2007, A&A, 464, 967

Carretta, E., et al. 2009, A&A, 505, 117

Carretta, E., et al., submitted to ApJL

Cassisi, S., Salaris, M., Pietrinferni, A., Piotto, G., Milone, A. P., Bedin, L. R., & Anderson, J. 2008, ApJL, 672, L115

Cohen, J. G. 1978, ApJ, 223, 487

Cohen, J. G. 1981, ApJ, 247, 869

Cohen, J. G., & Meléndez, J. 2005, , 129, 303

Cudworth, K. M., & Rees, R. 1990, , 99, 1491

Da Costa, G. S., & Armandroff, T. E. 1995, , 109, 2533

D'Antona, F., Gratton, R., & Chieffi, A. 1983, Memorie della Societa Astronomica Italiana, 54, 173

D'Antona, F., & Caloi, V. 2004, ApJ, 611, 871

D'Antona, F., Bellazzini, M., Caloi, V., Pecci, F. F., Galleti, S., & Rood, R. T. 2005, ApJ, 631, 868

Decressin, T., Meynet, G., Charbonnel, C., Prantzos, N., & Ekström, S. 2007, A&A, 464, 1029

Dekker, H., D'Odorico, S., Kaufer, A., Delabre, B., & Kotzlowski, H. 2000, , 4008, 534

Dickens, R. J., & Bell, R. A. 1976, ApJ, 207, 506

Dinescu, D. I., Girard, T. M., & van Altena, W.F. 1999, AJ, 117, 1792

Drake, J. J., Smith, V. V., & Suntzeff, N. B. 1992, ApJL, 395, L95

Drake, J. J., Smith, V. V., & Suntzeff, N. B. 1994, ApJ, 430, 610

Ferraro, F. R., Sollima, A., Pancino, E., Bellazzini, M., Straniero, O., Origlia, L., & Cool, A. M. 2004, ApJL, 603, L81

Francois, P., Spite, M., & Spite, F. 1988, A&A, 191, 267

Freeman, K. C., & Rodgers, A. W. 1975, ApJL, 201, L71

Freeman, K. C. 1993, The Globular Cluster-Galaxy Connection, 48, 608

Fusi Pecci, F., Ferraro, F. R., Bellazzini, M., Djorgovski, S., Piotto, G., & Buonanno, R. 1993, , 105, 1145

Gratton, R. G. 1982, A&A, 115, 171

Gratton, R. G., Quarta, M. L., & Ortolani, S. 1986, A&A, 169, 208

Gratton, R. G., Carretta, E., & Castelli, F. 1996, A&A, 314, 191

Gratton, R. G., Carretta, E., Eriksson, K., & Gustafsson, B. 1999, A&A, 350, 955

Gratton, R. G., et al. 2001, A&A, 369, 87

Gratton, R., Sneden, C., & Carretta, E. 2004, , 42, 385

Grundahl, F., Briley, M., Nissen, P. E., & Feltzing, S. 2002, A&A, 385, L14

Hamuy, M. 2003, ApJ, 582, 905

Harris, W. E. 1996, VizieR Online Data Catalog, 7195, 0

Hesser, J. E., Hartwick, F. D. A. & McClure, R. D. 1977, ApJS, 33, 471

Hesser, J. E., Bell, R. A., Harris, G. L. H., & Cannon, R. D. 1982, , 87, 1470

Hilker, M., & Richtler, T. 2000, A&A, 362, 895

Hughes, J., & Wallerstein, G. 2000, , 119, 1225

Ideta, M., & Makino, J. 2004, ApJL, 616, L107

Ivans, I. I., Sneden, C., Kraft, R. P., Suntzeff, N. B., Smith, V. V., Langer, G. E., & Fulbright, J. P. 1999, , 118, 1273

Ivans, I. I., Kraft, R. P., Sneden, C., & Smith, G. H. 2000, Bulletin of the American Astronomical Society, 32, 738

Ivans, I. I., Sneden, C., Wallerstein, G., Kraft, R. P., Norris, J. E., Fulbright, J. P., & Gonzalez, G. 2004, Memorie della Societa Astronomica Italiana, 75, 286

Johnson, C. I., Kraft, R. P., Pilachowski, C. A., Sneden, C., Ivans, I. I., & Benman, G. 2005, , 117, 1308

Johnson, C. I., Pilachowski, C. A., Simmerer, J., & Schwenk, D. 2008, ApJ, 681, 1505

Johnson, C. I., Pilachowski, C. A., Michael Rich, R., & Fulbright, J. P. 2009, ApJ, 698, 2048

Kayser, A., Hilker, M., Grebel, E. K., & Willemsen, P. G. 2008, A&A, 486, 437

Kemp, S. N., Bates, B., & Lyons, M. A. 1993, A&A, 278, 542

King, I. R., Anderson, J., Cool, A. M., & Piotto, G. 1998, ApJL, 492, L37

Kraft, R. P. 1994, , 106, 553

Kurucz, R. L., Furenlid, I., Brault, J., & Testerman, L. Solar Flux Atlas from 296 to 1300 nm, National Solar Observatory Atlas No. 1, June 1984

Kurucz, R. L. 1992, in IAU Symp. 149, The Stellar Populations of Galaxies, ed. B. Barbuy & A. Renzini (Dordrecht: Reidel), 225

Kupka, F., Piskunov, N., Ryabchikova, T. A., Stempels, H. C., & Weiss, W. W. 1999, A&AS, 138, 119

Lawler, J. E., Bonvallet, G., & Sneden, C. 2001, ApJ, 556, 452

Layden, A. C., & Sarajedini, A. 2000, , 119, 1760

Lee, S.-W. 1977, A&AS, 27, 367

Lee, Y.-W., Joo, J.-M., Sohn, Y.-J., Rey, S.-C., Lee, H.-C., & Walker, A. R. 1999, , 402, 55

Lehnert, M. D., Bell, R. A., & Cohen, J. G. 1991, ApJ, 367, 514

Lyons, M. A., Bates, B., Kemp, S. N., & Davies, R. D. 1995, MNRAS, 277, 113

Mandushev, G., Staneva, A., & Spasova, N. 1991, A&A, 252, 94

Marino, A. F., Villanova, S., Piotto, G., Milone, A. P., Momany, Y., Bedin, L. R., & Medling, A. M. 2008, A & A, 490, 625

Marino, A. F., Milone, A. P., Piotto, G., Villanova, S., Bedin, L. R., Bellini, A., & Renzini, A. 2009, A&A, 505, 1099

McCall, M. L. 2004, , 128, 2144

Milone, A. P., et al. 2008, ApJ, 673, 241

Milone, A. P., Bedin, L. R., Piotto, G., & Anderson, J. 2009, A&A, 497, 755

Milone, A. P., et al. 2010, ApJ, 709, 1183

Moehler, S., & Sweigart, A. V. 2006, A&A, 455, 943

Momany, Y., Cassisi, S., Piotto, G., Bedin, L. R., Ortolani, S., Castelli, F., & Recio-Blanco, A. 2003, A&A, 407, 303

Monaco, L., Pancino, E., Ferraro, F. R., & Bellazzini, M. 2004, MNRAS, 349, 1278

Moretti, A. et al. 2008, A&A, 493, 539

Norris, J., & Bessell, M. S. 1975, ApJL, 201, L75

Norris, J., & Freeman, K. C. 1979, ApJL, 230, L179

Norris, J. 1980, Globular Clusters, 113

Norris, J. 1981, ApJ, 248, 177

Norris, J. E. & Freeman, K. C. 1983, ApJ, 266, 130

Norris, J. E., & Da Costa, G. S. 1995, ApJ, 447, 680

Norris, J. E., Freeman, K. C., & Mighell, K. J. 1996, ApJ, 462, 241

Norris, J. E. 2004, ApJL, 612, L25

Pancino, E., Ferraro, F. R., Bellazzini, M., Piotto, G., & Zoccali, M. 2000, ApJL, 534, L83

Pasquini, L., et al. 2002, The Messenger, 110, 1

Persson, S. E., Cohen, J. G., Matthews, K., Frogel, J. A., & Aaronson, M. 1980, ApJ, 235, 452

Peterson, R. C., & Cudworth, K. M. 1994, ApJ, 420, 612

Peterson, R. C., Rees, R. F., & Cudworth, K. M. 1995, ApJ, 443, 124

Pietrinferni, A., Cassisi, S., Salaris, M., & Castelli, F. 2004, ApJ, 612, 168

Pilachowski, C., Wallerstein, G., Leep, E. M. & Peterson, R. C. 1984, ApJ, 263, 187

Piotto, G., Villanova, S., Bedin, L. R., Gratton, R., Cassisi, S., Momany, Y., Recio-Blanco, A., Lucatello, S., Anderson, J., King, I. R., Pietrinferni, A., & Carraro, G. 2005, ApJ, 621, 777 (P05)

Piotto, G., et al. 2007, ApJL, 661, L53

Piotto, G. 2008, in XXI Century Challenges for Stellar Evolution, Memorie della Societa Astronomica Italiana, vol. 79/2, eds: S. Cassisi, M. Salaris (arXiv:0801.3175)

Piotto, G. 2009, arXiv:0902.1422

Piotto, G., et al. 2009, in preparation

Prantzos, N., Charbonnel, C., & Iliadis, C. 2007, A&A, 470, 179

Preston, G. W., Sneden, C., Thompson, I. B., Shectman, S. A., & Burley, G. S. 2006, , 132, 85

Pryor, C., & Meylan, G. 1993, Structure and Dynamics of Globular Clusters, 50, 357

Ramírez, S. V., & Cohen, J. G. 2002, , 123, 3277

Recio-Blanco, A., Aparicio, A., Piotto, G., de Angeli, F., & Djorgovski, S. G. 2006, A&A, 452, 875

Recio-Blanco, A., & de Laverny, P. 2007, A&A, 461, L13

Renzini, A. 2008, MNRAS, 391, 354

Rey, S.-C., Lee, Y.-W., Ree, C. H., Joo, J.-M., Sohn, Y.-J., & Walker, A. R. 2004, , 127, 958

Rich, R. M., Sosin, C., Djorgovski, S. G., Piotto, G., King, I. R., Renzini, A., Phinney, E. S., Dorman, B., Liebert, J., Meylan, G. 1997, ApJ, 484, 25

Richer, H. B., et al. 2008, , 135, 2141

Richter, P., Hilker, M., & Richtler, T. 1999, A&A, 350, 476

Sandage, A., & Wildey, R. 1967, ApJ, 150, 469

Sarajedini, A., & Layden, A. C. 1995, , 109, 1086

Sarajedini, A., et al. 2007, , 133, 1658

Shetrone, M. D. 2003, ApJL, 585, L45

Siegel, M. H., et al. 2007, ApJL, 667, L57

Skrutskie, M. F., Cutri, R. M., Stiening, R., Weinberg, M. D., Schneider, S. et al. 2006, AJ, 131, 1163

Smith, V. V., Cunha, K., & Lambert, D. L. 1995, , 110, 2827

Smith, V. V., Suntzeff, N. B., Cunha, K., Gallino, R., Busso, M., Lambert, D. L., & Straniero, O. 2000, , 119, 1239

Smith, V. V., Cunha, K., Ivans, I. I., Lattanzio, J. C., Campbell, S., & Hinkle, K. H. 2005, ApJ, 633, 392

Smith, G. H., & Briley, M. M. 2005, , 117, 895

Smith, G. H., & Briley, M. M. 2006, , 118, 740

Sollima, A., Ferraro, F. R., Pancino, E., & Bellazzini, M. 2005, MNRAS, 357, 265

Sollima, A., Pancino, E., Ferraro, F. R., Bellazzini, M., Straniero, O., & Pasquini, L. 2005, ApJ, 634, 332

Sollima, A., Ferraro, F. R., Bellazzini, M., Origlia, L., Straniero, O., & Pancino, E. 2007, ApJ, 654, 915

Sosin, C., et al. 1997, ApJL, 480, L35

Sneden, C. A. 1973, Ph.D. Thesis

Sneden, C., Kraft, R. P., Guhathakurta, P., Peterson, R. C., & Fulbright, J. P. 2004, , 127, 2162

Stanford, L. M., Da Costa, G. S., Norris, J. E., & Cannon, R. D. 2006, ApJ, 647, 1075

Straizys, V., & Kuriliene, G. 1981, Ap&SS, 80, 353

Suntzeff, N. B., & Smith, V. V. 1991, ApJ, 381, 160

Suntzeff, N. B., & Kraft, R. P. 1996, , 111, 1913

Sweigart, A. V., & Mengel, J. G. 1979, ApJ, 229, 624

Sweigart, A. V. 1997, ApJL, 474, L23

Sweigart, A. V., & Catelan, M. 1998, ApJL, 501, L63

Tsuchiya, T., Korchagin, V. I., & Dinescu, D. I. 2004, MNRAS, 350, 1141

van den Bergh, S. 1967, , 72, 70

van de Ven, G., van den Bosch, R. C. E., Verolme, E. K., & de Zeeuw, P. T. 2006, A&A, 445, 513

van Leeuwen, F., Le Poole, R. S., Reijns, R. A., Freeman, K. C., & de Zeeuw, P. T. 2000, A&A, 360, 472

Ventura, P., D'Antona, F., Mazzitelli, I., & Gratton, R. 2001, ApJL, 550, L65

Ventura, P., D'Antona, F., & Mazzitelli, I. 2002, A&A, 393, 215

Ventura, P., Caloi, V., D'Antona, F., Ferguson, J., Milone, A., & Piotto, G. P. 2009, MNRAS, 399, 934

Villanova, S., Piotto, G., King, I. R.; Anderson, J., Bedin, L. R., Gratton, R. G., Cassisi, S., Momany, Y., Bellini, A., Cool, A. M., et al. 2007, ApJ, 663, 296

Yong, D., & Grundahl, F. 2008, ApJL, 672, L29

Yong, D., Grundahl, F., D'Antona, F., Karakas, A. I., Lattanzio, J. C., & Norris, J. E. 2009, ApJL, 695, L62

Zinnecker, H., Keable, C. J., Dunlop, J. S., Cannon, R. D., & Griffiths, W. K. 1988, The Harlow-Shapley Symposium on Globular Cluster Systems in Galaxies, 126, 603